University of Miami
Scholarly Repository

2009-07-24

A Laboratory Study of the Transfer of Momentum Across the Air-Sea Interface in Strong Winds

Ivan B. Savelyev
University of Miami, ivansav@gmail.com

Follow this and additional works at: https://scholarlyrepository.miami.edu/oa_dissertations

UNIVERSITY OF MIAMI

A LABORATORY STUDY OF THE TRANSFER OF MOMENTUM ACROSS THE
AIR-SEA INTERFACE IN STRONG WINDS

By

Ivan B. Savelyev

A DISSERTATION

Submitted to the Faculty
of the University of Miami
in partial fulfillment of the requirements for
the degree of Doctor of Philosophy

Coral Gables, Florida

August 2009

UNIVERSITY OF MIAMI

A dissertation submitted in partial fulfillment of
the requirements for the degree of
Doctor of Philosophy

A LABORATORY STUDY OF THE TRANSFER OF MOMENTUM ACROSS THE
AIR-SEA INTERFACE IN STRONG WINDS

Ivan B. Savelyev

Approved:

_____
Mark A. Donelan, Ph.D.
Professor of Applied
Marine Physics

_____
Terri A. Scandura, Ph.D.
Dean of the Graduate School

_____
Brian K. Haus, Ph.D.
Associate Professor of Applied
Marine Physics

_____
William M. Drennan, Ph.D.
Professor of Applied
Marine Physics

_____
Lynn K. Shay, Ph.D.
Professor of Meteorology
and Physical Oceanography

_____
John C. Van Leer, Sc.D.
Associate Professor of
Meteorology and Physical
Oceanography

SAVELYEV, IVAN   (Ph.D., Applied Marine Physics)
A Laboratory Study of the Transfer of Momentum   (August 2009)
Across the Air-Sea Interface in Strong Winds

Abstract of a dissertation at the University of Miami.

Dissertation supervised by Professor Mark Donelan.
No. of pages in text. (101)

A quantitative description of wind-wave and wind-current momentum transfer in high wind conditions is currently unresolved, mainly due to the severe character of the problem. It is, however, necessary for accurate wave models, storm and hurricane forecasting, and atmosphere-ocean model coupling.

In this research, strongly forced wind-wave conditions were simulated in a laboratory tank. On the air side, a static pressure probe mounted on a vertical wave follower measured wave-induced airflow pressure fluctuations in close proximity to the surface. Vertical profiles of wave-induced pressure fluctuations were resolved and wave phase dependent features, such as airflow separation, identified. Based on the pressure measurements, wind-wave momentum fluxes were obtained. The dependence of the spectral wave growth function on wind forcing, wave steepness, and wave crest sharpness was also investigated.

The bulk air-sea momentum fluxes were estimated using the "total budget" experimental technique. It provided information on the contribution of a wind-wave flux induced by a single wave to the total air-sea momentum flux. The percentile contribution

of wind-wave momentum flux into one wave was found to be dependent on the wave's steepness. An arbitrary change in steepness, however, was found to modify the wave field in such a way that it had little effect on the total wind stress.

To complement wind stress measurements velocity profiles in the water were measured using Particle Image Velocimetry technique. Mean current, turbulent stress, turbulent kinetic energy and turbulent dissipation rate vertical profiles were studied as a function of wind speed. Together with wave spectrum evolution measurements they form a complete empirical description of momentum fluxes in the laboratory tank.

The results provide a detailed empirical view on airflow pressure fluctuations over a wavy surface, on total wind stress, and on the velocity response in the water. A new wave growth parameterization with wind forcing range extended into storm conditions is the most significant stand alone result of this work. Combined with the near surface vertical profiles, these empirical data also serve as a test bed for coupled air-sea numerical models.

Acknowledgments

TABLE OF CONTENTS

LIST OF FIGURES

Figure

LIST OF TABLES

Chapter 1: Introduction.

The understanding of air-sea interaction is critical for the accurate prediction of atmosphere and ocean dynamics. In particular, the vertical flux of horizontal momentum is a major parameter needed to estimate near-surface mixing, to predict hurricane strength, to forecast global surface waves, and to simulate global atmosphere-ocean circulation. Modern numerical studies dedicate a large effort to solve equations of motion and to simulate atmosphere and ocean dynamics. Yet the present formulation of air-sea momentum flux is often oversimplified and its dependence on sea state is largely neglected in practical applications. The entire physical process at the air-sea interface is often expressed in terms of a parameter such as the drag coefficient. This approach is not due to an insignificance of the processes at the air-sea interface; rather it is due to the complexity of the problem and a lack of related physical understanding. Therefore, additional research is needed to be able to incorporate the dynamics of the air-sea interface into parameterization of air-sea fluxes.

The physics of shear flow near a flat boundary are fairly well understood (Prandtl 1905), but the air-sea interface is a free surface boundary, which adds another level of complexity to the problem. Therefore, a large amount of work was dedicated to the problem of "momentum transfer from a shear flow to a wavy boundary" over the last century (Lamb 1945, Miles 1957, Benjamin 1959, Mellor 1966, among many others).

In the process of air-sea momentum transfer, wind forcing initiates and amplifies instabilities on the water surface which results in the formation of initially capillary-gravity and later gravity surface waves. These waves, in turn, increase surface roughness and further enhance the momentum transfer to form a feedback mechanism. Hence, to

fully understand the air-sea momentum flux it is necessary to understand the dynamics of surface waves and to predict their response to winds and currents.

While the basic linear surface wave theory is available, it no longer applies once waves reach a finite steepness. Some non-linear approaches to surface wave dynamics exist (e.g. Chalikov and Sheinin 1998); however, none of them are able to describe the process after a wave of a critical steepness collapses because of surface instability.

Due to the difficulties described above, a combination of basic wave theory and empirical functions, based on observations, is being used for ocean wave modeling (e.g. WAM and WAVEWATCH models). Such models represent the ocean waves as a superposition of linear sine wave, which makes it possible to represent surface wave field as a function of frequency using Fourier analysis. Specifically for wave representation in frequency domain, a number of theoretical and empirical methods were designed to account for wave breaking (Melville and Rapp 1985, Banner et al. 2002), wave-wave interaction (Benjamin and Feir 1967, Zakharov 1968, Hasselmann et al. 1976), and wind-wave energy input (Snyder et al. 1981, Donelan et al. 2006).

The total momentum flux is composed of wind-wave and wind-current fluxes, and in general it depends on the state of the surface waves. The state of surface waves in turn depends on wind-wave momentum flux. Therefore, it is necessary to resolve both wind-wave and wind-current components of the flux separately. In an attempt to avoid such complication, a simplified approach exists, typically used for global atmosphere-ocean model coupling. In this approach the momentum flux is simply expressed as a function of wind speed ($\tau = \rho_a C_D U^2$, where ρ_a – air density, U – wind speed at 10 m height and C_D – drag coefficient). The approach simply assumes that for a given wind speed any wavy

surface would always result in the same momentum flux. While this provides some rough estimate on the total momentum flux, the partitioning of momentum between currents and waves remains largely unknown.

The purpose of this work is to measure the momentum flux in laboratory conditions as it crosses the air-sea boundary. Wind forcing impact on near-surface current, turbulence and surface waves is measured, analyzed and parameterized throughout the thesis. Special emphasis is given to high wind conditions and to wind-wave momentum flux resulting in parameterization of wave growth in hurricane-like conditions

The structure of the thesis is the following: Chapter 2 provides theoretical background, an overview of the literature, and results in the formulation of specific research goals. Chapter 3 describes experimental setups used to acquire the necessary data. Chapter 4 focuses on specific data analysis techniques. Chapter 5 outlines major results and provides a discussion and interpretation. Chapter 6 summarizes the research results with concluding remarks on the broader implications of the research.

Chapter 2: Background.

a. The fundamental theory overview.

Below is a brief overview of basic physical principles and equations widely used to describe fluid motion and momentum and energy fluxes. This includes momentum flux through the air-sea interface, surface wave energy growth and dissipation, and the response of near-surface currents to wind stress. The goal is to identify places in the theory, where empirical guidance is needed. In the following sections a detailed discussion on each of such issues is given and the experimental goals of this work are formulated.

The basic equations, describing a closed control volume of fluid can be written as following:

$$\oiint \vec{u} \cdot \vec{n} dA = 0 \qquad \text{- the continuity equation,} \qquad (2.1)$$

$$\frac{\partial}{\partial t} \iiint \vec{u} dV + \oiint \vec{u}\vec{u} \cdot \vec{n} dA = -\oiint p\vec{n} dA + \oiint \vec{\tau} dA + \iiint \frac{\rho}{\rho_0} \vec{g} dV \qquad (2.2)$$

- the momentum conservation equation,

where $\vec{u}$ – velocity, p – pressure, $\vec{n}$ – normal unit vector, ρ/ρ_0 – the ratio of a local water density to the non-disturbed density, $\vec{\tau}$ – stress, $\vec{g}$ - acceleration due to gravity. Equation 2.2 for the x component (i.e., $\vec{u} = u\vec{i} + v\vec{j} + w\vec{k}$, Fig. 2.1) takes the form (Mellor 2008a):

$$\frac{\partial}{\partial t} \iiint u dV + \oiint u\vec{u} \cdot \vec{n} dA = -\oiint p n_x dA + \oiint \tau_{vx} dA + \iiint \frac{\rho}{\rho_0} g_x dV \qquad . (2.3)$$

Suppose the upper boundary of such volume is at the wave surface and the lower boundary is horizontal at some depth z (Fig. 2.1). The vertical transport of horizontal

4

momentum in and out of the volume is described by the following terms: The horizontal

viscous stress term at the lower boundary is dominated by turbulent momentum transport:

$$\tau_x\big|_z = -\rho \overline{u'w'}. \qquad\qquad (2.4)$$

The horizontal viscous stress at the wavy boundary $\tau_x\big|_0$ (later denoted simply as τ)

is determined experimentally, depending on wave conditions. Particularly, to do so the

velocity profile in the viscous sublayer must be measured. Since the layer thickness is of

the order of 1 mm, such an experiment is very delicate. To measure the shape of the

velocity profile, Okuda et al. (1977) traced micro bubbles simultaneously released along

a vertical line, and Banner and Pierson (1998) used Particle Image Velocimetry, which is

discussed in detail in Chapter 3.c.

The first term on the right hand side of eq.2.3 is essentially the momentum flux

due to surface roughness:

$$pn_x dA = p\frac{\partial \eta}{\partial x} dxdy, \qquad\qquad (2.5)$$

where η represents wave surface elevation. At the wave surface, this term describes the

momentum flux going from wind to waves, and at the lower boundary it is equal to zero.

The value $p\dfrac{\partial \eta}{\partial x}$ is important and will be discussed
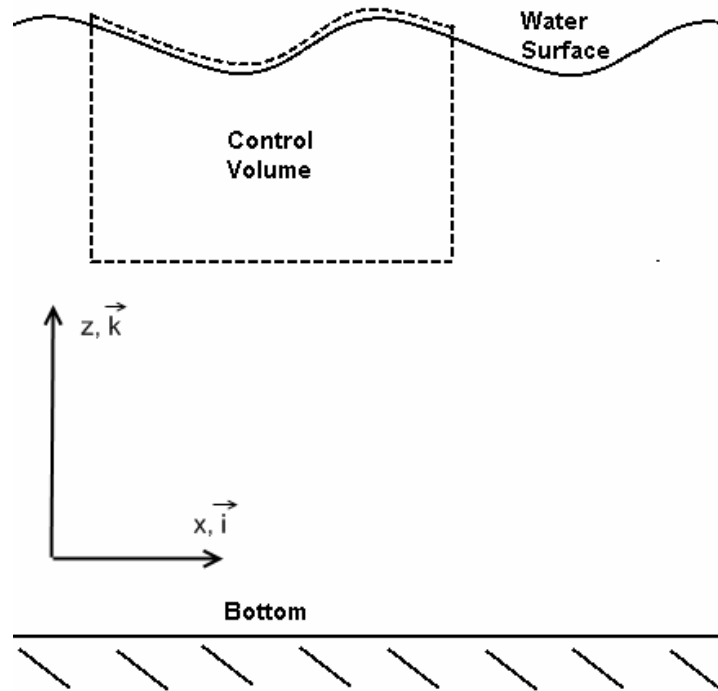
Figure 2.1. The dashed line shows the borders of a control volume within the water column.

throughout the paper because it is also used in the energy input term $S_{in} = c_p p \dfrac{\partial \eta}{\partial x}$ in the

deep water wave energy equation (Hasselmann 1960):

$$\frac{\partial E(\omega)}{\partial t} + \frac{\partial}{\partial x} c_g E(\omega) = S_{in} + S_{nl} + S_d , \qquad (2.6)$$

where c_g and c_p are group and phase wave velocities, E is wave energy, ω − wave

frequency, S_d is the dissipation function, mostly due to wave breaking, and

S_{nl} is the non-linear transfer function, responsible for the wave energy re-distribution

among wave spectrum frequencies. Equation 2.6 is widely used in numerical wave

models (e.g. Hasselmann et al. 1988). While an estimate for the non-linear term is mostly

a challenging theoretical problem (Valenzuela and Laing 1972, Hasselmann et al. 1976,

Gastel 1987), wave energy input and dissipation terms, discussed in the following subchapters, are mostly determined empirically.

Empirical estimates of a sum of all terms on the right hand side (eq.2.6) are available through measurements of wave spectra evolution for short fetched waves (e.g. Hasselmann et al. 1973, Dobson et al. 1989, Zhang 1995), nearly fully developed seas (e.g. Moskowitz 1964, Snyder and Cox 1966, Ewing and Laing 1987), and combined seas (Donelan et al. 1992b). Such bulk parameterizations are useful for cross-reference and evaluation of the sum of three terms, but are too idealized for practical wave modeling purposes.

The kinetic energy budget equation for the mean flow is given by:

$$\frac{D}{Dt}(\frac{1}{2}U_i^2) = \frac{\partial}{\partial x_j}(-\frac{PU_j}{\rho_0} + U_i\overline{u_iu_j} + 2\nu U_iE_{ij})$$
$$- \overline{u_iu_j}\frac{\partial U_i}{\partial x_j} - \frac{g}{\rho_0}\overline{\rho U_3} - 2\nu\overline{E_{ij}E_{ij}}$$

(2.7)

where $E_{ij} = \frac{1}{2}(\frac{\partial U_i}{\partial x_j} + \frac{\partial U_j}{\partial x_i})$, ν – viscosity, i and j equal to 1,2 and 3 correspond to x,y

and z coordinates. On the right hand side the first term is the energy transport, the second term is the energy loss to turbulence, the third term is the loss to potential energy and the last term is the energy dissipation rate

$$\varepsilon = 2\nu\overline{E_{ij}E_{ij}} .$$

(2.8)

In numerical models, the resolution is such that small features like fluctuating components of velocities can not be fully resolved. Therefore, the Reynolds stress $\overline{uw}$ and dissipation rate ε are parameterized empirically as functions of depth.

The brief overview, provided above, allows to summarize the empirical data, required by the theory to close the fundamental equations and to prepare them for solution. The required empirical functions are the following: viscous and form drag at the wavy surface, Reynolds stress and dissipation rate vertical profiles, total wind stress, wave energy input, dissipation and non-linear transfer. A detailed discussion on the specific methods related to obtaining these functions is provided below.

b. Roughness induced momentum flux through the surface.

One of the empirically determined terms, required to close the definition of the problem is the 'pressure – surface slope' product averaged over the water surface $\overline{p\dfrac{\partial \eta}{\partial x}}$.

This section discusses in detail the underlying physical processes, reviews literature and defines experimental goals on this matter.

As wind speed increases, the physical processes at the air-sea interface change dramatically, moving from smooth, laminar cases to fully turbulent regime dominated by rough airflow over waves. One particular goal is to fill in the gap in understanding and parameterization of wind-wave momentum transfer in strongly forced wind-wave conditions.

Present theories are able to describe a regime corresponding to light wind blowing over sine waves of small steepness. A wave acts as a surface roughness element, causing airflow streamlines to curve along the wave surface with a slight phase lag. This causes airflow acceleration and deceleration along the surface, and thus pressure differences appear between windward and leeward sides of the wave. The part of the wave-induced surface pressure pattern, which is in phase with the slope of the surface, acts to deposit

wind momentum into the flow field of the wave. This process was described in analytical solutions by Miles (1957, 1959, 1960), supported by the following work of Benjamin (1959), Davis (1969) and more recently further developed by Janssen (1991), Belcher and Hunt (1993, 1998), and Miles (1993). Miles introduced a non-dimensional wave growth function and suggested its dependence on wind forcing. Moreover, as long as waves of various frequencies are superposed and can be represented as wave spectra, it is possible to parameterize wind-wave momentum transfer using a spectral wave growth function (i.e. Snyder et al., 1981), defined as:

$$\gamma(\omega) = \frac{\rho_w}{\rho_a} \frac{1}{\omega E(\omega)} \frac{\partial E(\omega)}{\partial t}, \quad (2.9)$$

where ρ_a, ρ_w - air and water densities, $E(\omega)$ – wave energy spectrum, ω – wave radian frequency.

Wave growth parameterization through one function that depends on wave age only is alluring, because it can be easily used by numerical spectral wave models to describe wave motion throughout the oceans. The theory, however, provided solutions only for a small range of light wind forcing. Also, according to Miles (1957), the controlling parameter for wind-wave forcing is the curvature of the wind profile at the "matched layer" height. The "matched layer" is defined by the height at which the horizontal wind speed is equal to the wave phase speed. Such a parameter, however, was not found to be useful in practice (i.e. Shemdin and Hsu 1967). First, a matched layer does not exist in wind opposing wave cases; second, even in moderate wind forcing situations, the matched layer height is near or within the viscous sublayer, which has a linear wind speed profile. For these reasons, experimental efforts were expended to reinforce the theoretical solution. Resulting empirical parameterizations (e.g., Snyder et

al. 1981; Donelan et al. 2006) use the dimensionless ratio U_{10}/C_p as a more appropriate

wind-wave forcing parameter, where U_{10} is the wind speed at 10m height (Fig.2.2).
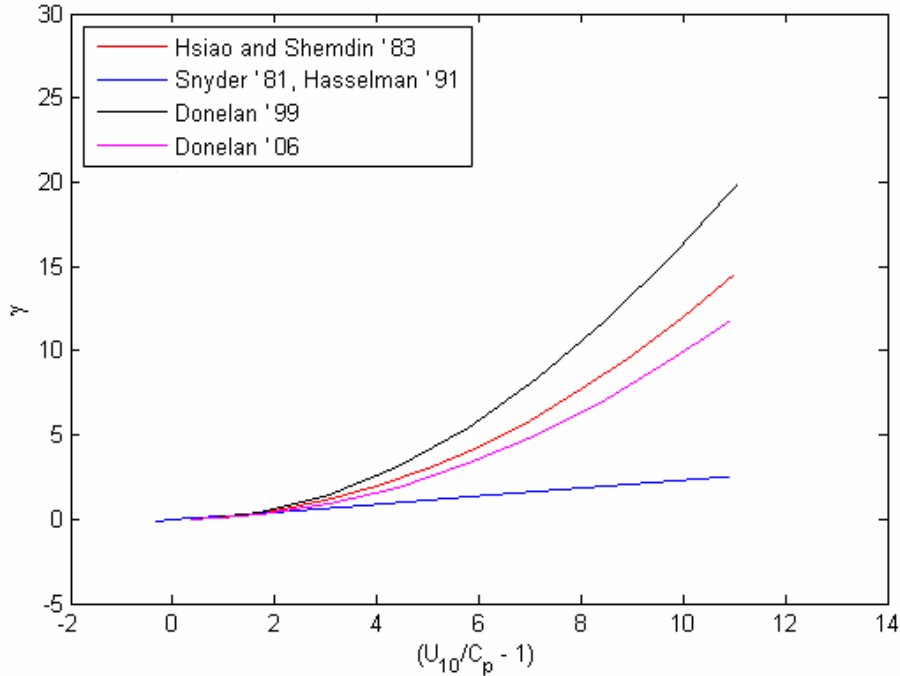
Figure 2.2. Empirical parameterizations of the wave growth (eq.2.9) as a function of wind forcing, obtained in several studies.

Momentum transfer from wind to waves is given by the pressure – slope

correlation:

$$M = \overline{p_o \frac{\partial \eta}{\partial x}}, \quad (2.10)$$

where $\partial \eta / \partial x$ is wave surface slope , p_0 represents static air pressure at the surface. The

most obvious approach to estimate momentum transfer experimentally was to use a static

air pressure probe (i.e., Elliott 1972b or Nishiyama, et al. 1991), while simultaneously

measuring surface elevation (Elliott, 1972a; Hsu, et al., 1982). However, it was predicted

(Miles 1957) and observed (Snyder 1974) that wave induced static pressure fluctuations

exponentially decay with height. Since the lowest position of the static pressure probe

must be higher than the highest wave crest, such measurements do not represent static pressure at the water surface, especially above wave troughs.

As a solution to this problem, vertical arrays of probes were used to extrapolate the magnitude of wave-induced fluctuations to the surface (Kondo et al. 1972, Snyder et al. 1981, Donelan et al. 1999a, Hristov et al. 2003, Donelan et al. 2005b, among others). This gave us the understanding that wave induced pressure fluctuations decay proportionally to $e^{-\alpha kz}$, where k – wave number, z – height, $\alpha \approx 1$. However, the exact form of pressure fluctuation decay near the surface, especially in strongly forced conditions, is still unknown. Therefore, one of the goals of the present study is to provide guidance for pressure extrapolation to the surface for future stationary probe measurements.

Another more direct experimental solution is to mount a static pressure probe on a frame that moves with surface elevation. Therefore, the probe is held at a small constant height from the surface. This method can potentially provide the most accurate measurements, however, it is technically challenging. In one of the first attempts (Dobson 1971), a surface buoyant platform was used to carry the pressure probe. In other attempts, coupled surface elevation sensors and vertical motor systems were used. Shemdin et al. (1967) reported successful following of a predetermined monochromatic wave in laboratory conditions. However, until recently, most of the attempts to use a wave-follower for a random wave field faced technical difficulties, especially in the field. Among the most successful were Snyder et al. (1981) in the Bight of Abaco, Bahamas experiment, Harris and DeCicco (1993), at the Chesapeake Bay Light Tower, Donelan (1999b) laboratory experiments, Jacobs et al. (2002), Meetpost Noordwijk research and

monitoring platform, Donelan et al. (2006), Lake George experiment (Fig 2.2). The resulting empirical estimates of $\gamma(U_{10}/C_p)$ generally agree in mature seas, however they scatter dramatically in strong wind forcing cases. In many aspects, the present work follows the experimental methodologies of these authors and the results are compared and discussed in the following chapters.

Strong wind over young waves with intense wave breaking and spray generation (Andreas 1998) are typical in the North Sea, the Southern Ocean, and during storms and hurricanes. The shape of the ocean surface is such that it can no longer be described by a linear wave theory. Moreover, wave breakers and spray add completely new physical elements to the problem. However, it is important to parameterize air-sea momentum transfer in these conditions to predict storm surge and wave height. At this moment no exact theory exists that describes wind-wave momentum transfer in such conditions. However, a "sheltering hypothesis", originally proposed by Jeffreys (1924, 1925), can be used as an assumption within the high-wind forcing theory (i.e. Kukulka et al. 2007) and, therefore, to extend existing wind-wave momentum transfer parameterization into high winds.

The rationale of the "sheltering hypothesis" is in a slow wind and smooth wave condition airflow streamlines take on the shape of the surface, except for some phase shift, which results in pressure difference between windward and leeward sides of the wave (Fig. 2.3). This airflow structure is also predicted by Miles (1957) theory. As wave steepness and wind forcing increase, at some point the airflow can no longer follow the surface shape and separates from it at the leeward side of the wave. Later on, airflow streamlines reattach to the surface at the windward side of the next wave (Fig.2.4.). In a

sense, the wave crest "shelters" the wave trough region from strong winds. This creates an isolated eddy with a much slower wind speed. As a result, pressure fluctuations along the wave surface are not as big as extrapolation of the linear case to strong winds would yield. This phenomenon was both predicted by numerical models (e.g. Celenligil and Mellor 1985, Shen et al. 2003, Ryn et al. 2007) and observed in laboratory conditions (Buckles et al. 1984, Reul 2008). However, its effect on wind-wave momentum transfer remains poorly understood.

The Jeffrey's sheltering effect can be quantified through a sheltering coefficient G (e.g. Donelan et al. 2006 suggested $G = 0.93$ for moderate wind forcing), so that

$$\gamma = \gamma(\frac{U_{10}}{C_p}, G) \quad . \qquad (2.11)$$

However, his sheltering hypothesis provides little guidance on what G should depend, and no experimental study was comprehensive enough to give a definite answer. Wave steepness should obviously be one of the key parameters, however other wind and wave parameters like wind speed and gustiness, wave asymmetries, breaking, and non-linear interactions may also affect it (Babanin and Makin 2008, Babanin et al. 2008).

The lack of information to construct the empirical function (eq. 2.11) in high wind conditions is mainly due to the incompatibility of harsh environmental conditions with the sensitive instrumentation needed for wave-following or vertical array experiments. To address this scientific question, the present study conducts wave-follower based measurements in laboratory conditions.
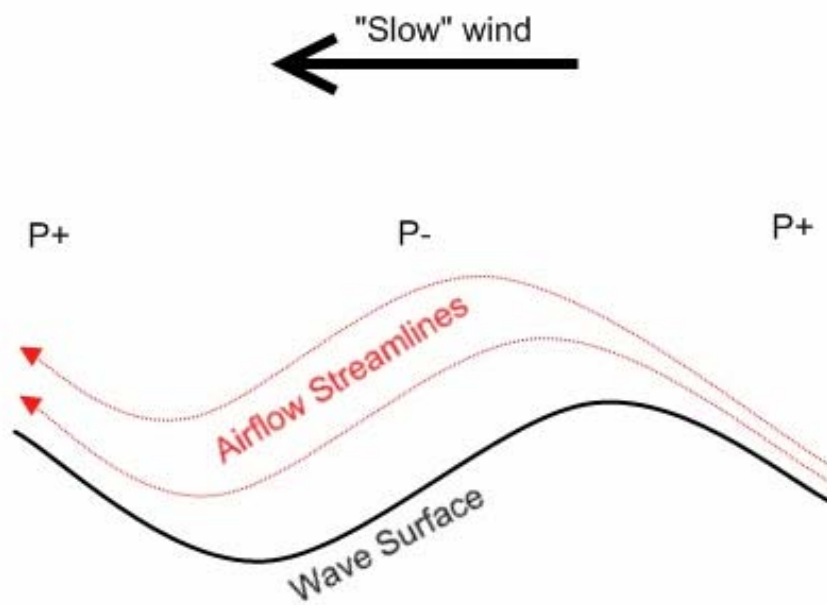
Figure 2.3. Airflow streamlines and static pressure distribution above smooth waves.
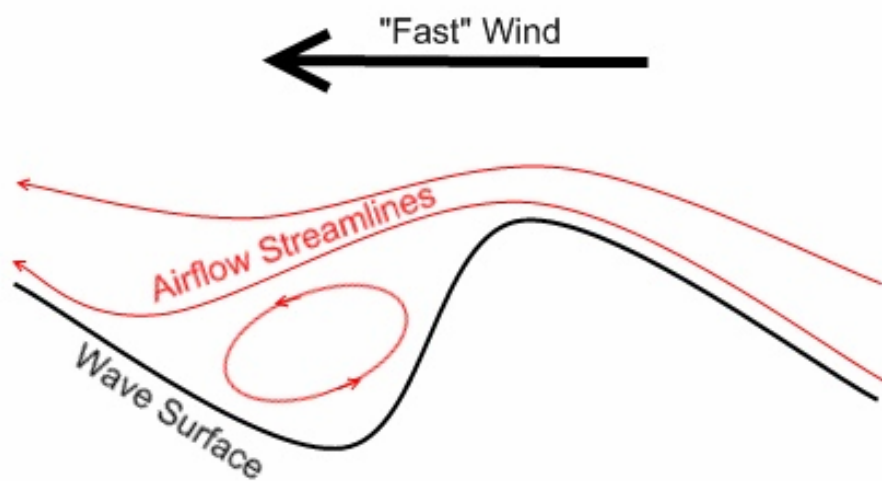
Figure 2.4. Airflow streamlines above steep waves.

c. Viscous stress.

In the simplest case, the wind blows over a flat water surface. This is not a common situation at the ocean surface, but it can happen under light wind and fetch limited conditions. The vertical wind profile is described the same way as in a classical "flow near a flat solid boundary" problem (e.g. Kundu and Cohen 2002, p.528). An approximate solution for this problem is called "The Law of the Wall":

$$U(z) = \frac{U_*}{\kappa} \ln \frac{z}{z_0},$$ (2.12)

where $U(z)$ is the vertical profile of the horizontal wind velocity, U_* is the friction velocity, z_0 is the surface roughness length. In this scenario, the momentum transfer from air to water is realized only through the tangential stress due to friction between air and water: $\tau_0 = \mu \frac{dU}{dz}$, where τ_0 is the shear stress at the surface, μ is the dynamic viscosity of the air.

Laboratory experiments on tangential stress in the case of light wind over waves of small steepness, were performed by Okuda et al. (1977) and Banner and Peirson (1998). The stress was estimated by measuring water velocity profiles in the surface sublayer within several millimeters from the surface. All authors achieved remarkable precision, but noticed that this technique could only work for smooth waves free of wave breakers.

In strong wind conditions no successful direct measurements of viscous stress were reported. Delicate velocity profile measurements near the surface are constantly interrupted by surface instability, leading to foam and bubble generation, interfering with measurements. The viscous stress, however, can potentially be estimated indirectly as the

difference between total and form drag, if such data is available. Here the form drag is a horizontal force applied to surface roughness elements by means of air pressure fluctuations.

d. The total air-sea momentum flux.

In large scale applications, such as atmosphere-ocean coupled numerical models, the state of a local wave field is often unknown. However, it is necessary to approximately estimate the rate of momentum exchange at the air-sea interface. To empirically obtain such bulk parameterizations, the momentum flux is measured above the wave boundary layer, where the Reynolds stress is the dominant transport mechanism.

Away from the wavy boundary the momentum transfer from wind to water is given by

$$\tau = -\rho_a \overline{u'w'} = \rho_a U_*^2 = \rho_a C_D U(z)^2, \qquad (2.13)$$

where C_D is the drag coefficient at a height z, ρ is the air density. In this case, similar to the flow along the flat boundary, the vertical wind speed profile is described by the Law of the Wall (eq.2.12). Here the influence of waves on the wind profile is embedded in the surface roughness parameter z_0, related to drag coefficient as (e.g. Donelan 1990):

$$C_D = \kappa^2 (\ln \frac{z}{z_0})^{-2}. \qquad (2.14)$$

Classical dimensional considerations by Charnock (1955) suggest the expression for the roughness length

$$z_0 = m_0 U_*^2 / g, \qquad (2.15)$$

where m_0 is a constant, required to be determined empirically, Garratt (1977) found $m_0 =$ 0.0144. This allows the expression of the total air-sea momentum flux as a function of friction velocity.

Following Charnock's hypothesis, several experimental studies were aimed to confirm his formula (i.e., Deacon and Webb 1962, Smith 1980, Large and Pond 1981). This approximate approach to the momentum flux estimate is still widely used, since the direct measurements are typically unavailable. It is especially useful in strong wind conditions, where the information about surface waves can not be obtained. Therefore, the interest in such parameterization is strong, in part fueled by the demand of hurricane models. The drag coefficient C_D is traditionally given at 10m height reference level as a function of wind speed. Among recent parameterizations are Powell et. al (2003) and Donelan et. al (2004), that extend the range of the wind speed to over 50 ms^{-1}.

Further detailed analysis of the surface roughness dependence on wind and wave conditions revealed a more complex relationship (Donelan et al. 1993):

$$\frac{z_0}{\sigma} = 6.7 \cdot 10^{-4} (\frac{U_{10}}{C_p})^{2.6}, \qquad\qquad (2.16)$$

where σ is rms wave amplitude. Uz et al. (2002) confirmed the existence of a relationship between wind stress and wave field. These results revealed the importance of wave information to the parameterization of the total air-sea momentum flux.

e. The response of the near-surface currents to wind forcing.

To estimate the vertical Reynolds stress and dissipation rate profiles, a vertical profile of current velocity vectors must be measured. Such measurements were performed by Yefimov and Khristoforov (1971) to find a relationship between near-surface velocity

and wave spectra, and by Terray et al. (1999) to study wave effects on near-surface dissipation. In the laboratory, Howe et al. (1982) measured velocity profiles below and above the water surface to study the air-sea momentum flux, and Cheung and Street (1988a) used a Doppler velocimeter to measure orbital velocities of wind waves and their effect on the mean flow.

A wide array of instrumentation is available for such measurements, but once these data are acquired, the separation of turbulent and wave orbital velocities is not trivial, as their timescales often overlap. To separate these components, for example, Cheung and Street (1988a,b) used a Doppler anemometer mounted on a wave follower in laboratory conditions, so that the vertical orbital velocity is not included in the measured velocity. Such experimental techniques are usually impossible to implement in the field.

Particle Image Velocimetry (PIV) based measurements of the velocity profiles are especially effective as discussed in Chapter 3.c. PIV provides snapshots of velocity vectors with high spatial resolution both horizontally and vertically. Such data contains mean and fluctuating component of velocity vectors. For the purpose of more detailed velocity components separation (i.e. turbulent and orbital components), orbital velocities can be estimated using surface elevation time series (Donelan et al. 1992a). In general, the contamination of turbulent fluctuations with orbital velocities is a complex problem (Kitaigorodskii et al. 1983a,b). Its relation to the present experiment is further discussed in Chapters 4.b and 5.b.

While the calculation of vertical profiles of the mean current, Reynolds stress and turbulent kinetic energy is fairly straightforward, methods to estimate the turbulence

dissipation into heat deserve a separate discussion. By definition (eq.2.8), the dissipation rate is

$$\varepsilon = \nu \frac{\partial u_i}{\partial x_j}(\frac{\partial u_i}{\partial x_j} + \frac{\partial u_j}{\partial x_i}) ; \qquad (2.17)$$

however, PIV measurements can only provide velocities along a vertical plane. And the cross-plane component of velocity vectors is also typically unavailable. Normally, this difficulty can be overcome by assuming 3D isotropy, then the dissipation rate is simply

$$\varepsilon = 15\nu(\frac{\partial u}{\partial x})^2 , \qquad (2.18)$$

but since we are looking for the vertical variability of the dissipation rate, such an assumption is counterproductive. Instead, just two-dimensional horizontal isotropy assumption can be sufficient. An expression was derived specifically for PIV data by Doron et al. (2001):

$$\varepsilon = 3\nu\left[\left\langle\left(\frac{\partial u}{\partial x}\right)^2\right\rangle + \left\langle\left(\frac{\partial w}{\partial z}\right)^2\right\rangle + \left\langle\left(\frac{\partial u}{\partial z}\right)^2\right\rangle + \left\langle\left(\frac{\partial w}{\partial x}\right)^2\right\rangle + 2\left\langle\left(\frac{\partial u}{\partial z}\frac{\partial w}{\partial x}\right)\right\rangle + \frac{2}{3}\left\langle\left(\frac{\partial u}{\partial x}\frac{\partial w}{\partial z}\right)\right\rangle\right]$$

$$(2.19)$$

Equation 2.19, or another similar method described by Fincham et al. (1996), are effective direct ways of estimating dissipation rate if the spatial resolution of the measurements captures the scales at which turbulent kinetic energy dissipates into heat. But since sometimes a significant portion of the dissipation occurs over sub-millimeter scales, it is useful to have a method capable of utilizing coarsely resolved data. Such method exists and it is based on hypothesis, proposed by Kolmogorov (1941), where the velocity structure function is defined as

$$D_{ij}(\vec{x},\vec{r},t) \equiv \left\langle \left[U_i(\vec{x}+\vec{r},t)-U_i(\vec{x},t)\right] \cdot \left[U_j(\vec{x}+\vec{r},t)-U_j(\vec{x},t)\right] \right\rangle, \qquad (2.20)$$

which by definition is a covariance of the difference in velocity between two points defined by $\vec{x}+\vec{r}$ and $\vec{x}$. The hypothesis is based on the assumptions of turbulence isotropy and homogeneity, and also large Reynolds numbers. These assumptions simplify eq. 2.20 to

$$D_{ij}(\vec{r},t) = D_{NN}(r,t)\delta_{ij} + [D_{LL}(r,t)-D_{NN}(r,t)]\frac{r_i r_j}{r^2}, \qquad (2.21)$$

where D_{LL} and D_{NN} are longitudinal and transverse structure functions respectively, which are given by

$D_{11} = D_{LL,}$

$D_{22} = D_{33} = D_{NN,}$ $\qquad\qquad\qquad\qquad\qquad (2.22)$

$D_{ij} = 0$, for $i \neq j$.

Further, based on dimensional considerations, Kolmogorov's hypothesis suggests a unique relationship between the structure function, the distance r and the dissipation rate ε:

$$D_{LL}(r,t) = C_2(\varepsilon \cdot r)^{2/3}, \qquad\qquad\qquad (2.23)$$

where C_2 is a universal constant, determined empirically. Assuming stationarity, function D_{LL} is easily measurable; therefore, equation 2.23 gives an expression for ε.

Kolmogorov's hypothesis, as shown in later experimental studies, confirmed that the structure function decays at $r^{2/3}$ rate within the turbulence inertial dissipation range (e.g., Dickey and Mellor 1979). Structure function measurements within this range provide means for dissipation rate ε estimate. Moreover, it is not required to resolve the

flow up to the smallest scale, as any value of the structure function within the dissipation range is sufficient.

f. Wave dissipation.

The dissipation function (S_d) is the least known among all terms on the right hand side of eq. 2.6. Most of the wave dissipation is caused by wave breaking which is essentially a collapse of instability on the air-sea interface. Such a phenomenon is highly sensitive to initial conditions, which complicates the prediction of its dynamics in the open ocean. Bulk parameterization of wave dissipation also poses a challenge, as it may be caused by wind-forcing (Banner and Phillips 1974), wave-wave interactions, and wave instabilities (Melville 1982). Most of the wave breaking in the open ocean, however, happens due to wave-wave interaction. The phenomenon was isolated and carefully studied in laboratory conditions by Rapp and Melville (1990), where its relationship with the dissipation rate vertical profile was revealed. For spectral modeling purposes the wave dissipation is parameterized in terms of the wave spectra (e.g. Komen et al. 1984, Banner and Young 1994, Hara and Belcher 2002, Young and Babanin 2006).

g. Background summary.

In conclusion of the theoretical and experimental overview of the problem, it is appropriate to say that substantial progress has been made in the area over the past century. While, clearly the problem is still not completely solved, all obvious theoretical and experimental directions were thoroughly investigated by several authors. The results of these studies are widely applied in operational numerical models, as well as in new

approaches to atmosphere-wave-ocean numerical model coupling (i.e. Shchepetkin and McWilliams 2005, Mellor et al. 2008b).

One significant direction, however, remains largely unresolved: strong wind conditions. That is intensive wave breaking and spray generation due to surface instability add new physical processes that are influencing air-sea fluxes and particularly momentum flux. Powell et al. (2003) and Donelan et al. (2004) have shown that simple extrapolation of the air-sea parameterization (i.e. drag coefficient parameterization based on measurements in moderate winds) into hurricane conditions may not be done (Fig 2.5, taken from Donelan et al. 2004).
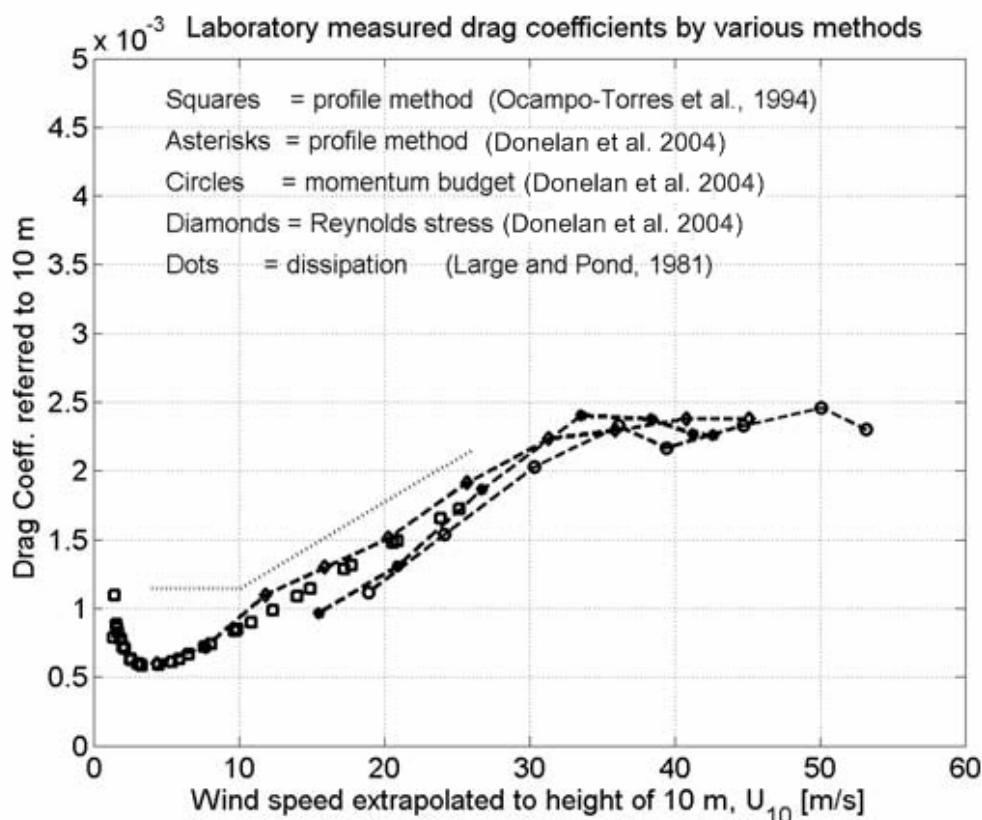
Figure 2.5. Empirically obtained parameterization for the drag coefficient. Linearly growing function within moderate wind range was found to saturate above 33ms^{-1}. The figure is taken from Donelan et al. (2004).

A typical assumption to make during analytical derivations related to the air-sea interface is the surface waves linearity. Since this assumption does not hold in strong winds, the existing theory must be used carefully, and often supplemented by corrections, related to the hurricane conditions.

The empirical functions, obtained for air-sea parameterization are especially vulnerable to extrapolation into high winds, as the vast majority of both field and laboratory experiments were conducted in moderate winds. The general idea behind this research is to provide experimental guidance on the necessary empirical functions, described above. Specifically, to show how these empirical functions react to wind conditions changing from moderate to severe.

Here, the experimental goal is to obtain near-surface vertical profiles of mean horizontal velocity, Reynolds stress, turbulent kinetic energy and dissipation rate. On the air-side total momentum flux was investigated, and an especially large effort was dedicated to wind-wave momentum flux.

Chapter 3: Experimental Methodology

a. Experimental facility overview

All experimental data presented in this work were acquired in the Air-Sea

Interaction Saltwater Tank (ASIST) at the Rosenstiel School of Marine and Atmospheric

Science, University of Miami (Fig.3.1.).

Figure 3.1. Air-Sea Interaction Saltwater Tank (ASIST)

ASIST is a state-of-the-art wind-wave tank, constructed in 2000. Its primary

purpose is to study various physical processes at the air-sea interface, including high

wind conditions, using modern techniques. The working section of ASIST is 15m long,

1m wide and 1m high. In a typical setup water occupies 0.42 m of the tank. For

simulations of realistic ocean conditions, it is equipped with a digitally controlled

mechanical wave generator (wave frequencies 0.25Hz – 3Hz, amplitudes 0-0.1 m), a

wind generator (wind speed in the tank's centerline 0-30 ms^{-1}), a current generator

(current speed 0-0.5 ms^{-1}), and a water temperature control (5-40ºC). The air circulation

has closed and open loop options. In the open loop option fresh airs comes from the

atmosphere and is exhausted back after passing the working section (Fig.3.2). The open

loop mode is used for gas, humidity and heat transfer to avoid quick saturation. On the

other hand, the closed loop mode yields a ~50% faster maximum wind speed. Mechanical

wave and current generation can be reversed, allowing simulation of opposing wind-

wave-current scenarios.
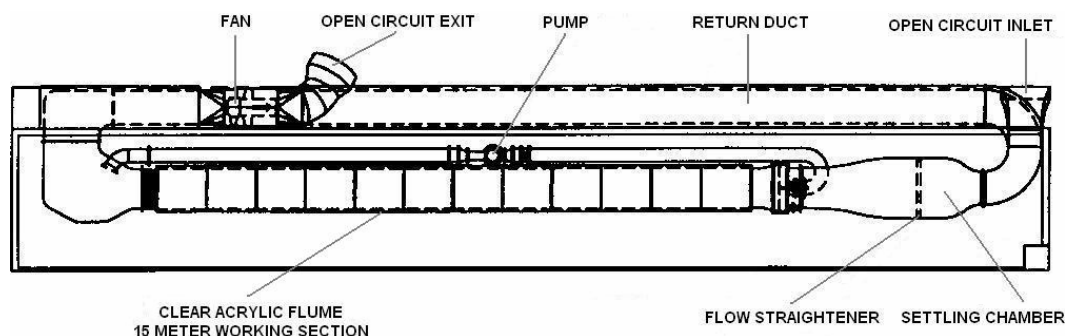
Figure 3.2 Air-Sea Interaction Saltwater Tank schematics.

Fully transparent acrylic walls, bottom and top of the tank allow using non-

intrusive optical methods for flow measurement and visualization. Such currently used

methods are the following:

Laser Elevation and Slope Gauges: Two Argon-Ion (manufactured by Melles

Griot, model 543R-BS-AO3, beam power 150 mW, wavelength 488 nm) air-cooled

lasers are equipped with beam splitters and mirrors to provide up to 6 vertical beams at

any points in the tank. The intersection of these beams with the surface is detected by

line-scan cameras at a rate of up to 1000 Hz. The cameras have a dynamic range of 2048

(pixels) and the range of heights is determined by the choice of lenses. At two locations a

slope sensor (manufactured by NWRI INRE, model 201) has been installed above the

laser elevation gauge. This sensor captures the deflection of the laser beam after it passes through the air-water interface.

Particle Image Velocimeter (PIV): This flow visualization and measurement system, manufactured by Dantec Dynamics, yields velocity vector maps in a 198 x 146 grid covering an area of size limited only by the optics. These maps are produced at a maximum rate of 15 Hz and multiple realizations of the flow at steady state can be used to make the statistical error arbitrarily small. A detailed description of the PIV system is provided in section 3.c.

Some physical properties, however, can not be measured without intrusion; also more direct measurements are useful for calibration of non-intrusive methods:

The "Pitot tube" measures the dynamic air pressure, *i.e.*, the difference between the static and the total head air pressure. It is used for a robust estimate of the wind speed, as well as for calibration of more sensitive wind speed measuring technique, such as hot films. Hot film system (manufactured by TSA) provides turbulence measurements in the air, and also aid PIV measurements in the water. Particularly, hot films allow high frequency (>100Hz) sampling rate, versus only 15 Hz for PIV.

The "Elliott tube", described in detail later in this text, is used for static pressure measurements. Its advantage over the "Pitot tube" is its ability to perform such measurements in an environment of dynamically changing wind direction. This probe is particularly useful for wind-wave drag measurements.

Resistance thermometers (wires) are used for turbulent temperature fluctuations measurement. Combined with the hot films, they provide an effective method for direct measurement of vertical turbulent heat flux.

b. "Wave-follower" based wind-wave momentum transfer measurements.

To study wind-wave momentum transfer an "Elliott" type of static air pressure probe (Elliott, 1972b) was used. Because wave induced wind pressure fluctuations quickly decay with height it was important to measure pressure as close to the wave surface as possible. Therefore, the probe was moved vertically and kept at a small constant distance (1-3 cm) from the surface. The sketch of the experiment design is shown on Fig. 3.3., and wave follower design is shown on Fig.3.4.
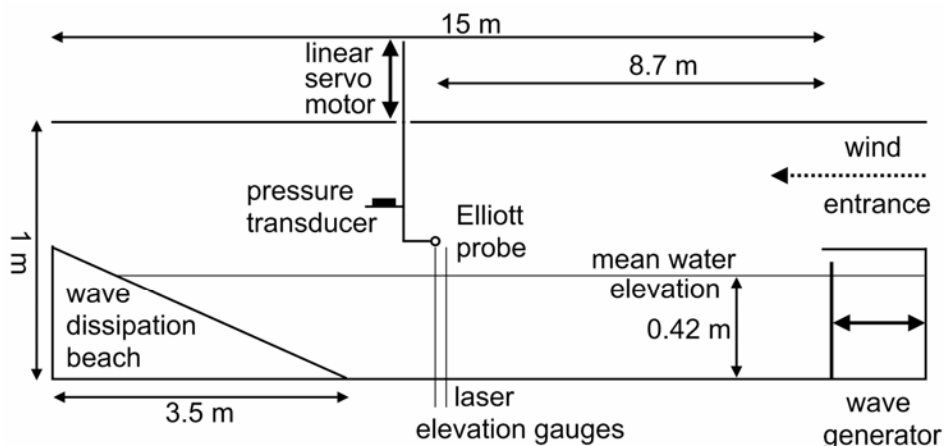
Figure 3.3. Sketch of the wind-wave momentum transfer experiment in the Air-Sea Interaction Saltwater Tank

To generate arbitrary wind-wave conditions a combination of wind fan and mechanical wave generator were used. During these experiments water temperature was equal to room temperature (20-22ºC) and no current was imposed. It was possible to generate wind forcing in the wide range of inverse wave age, as the wind speed was controlled by the fan and the wave phase speed was controlled through the wave frequency by the wave generator.
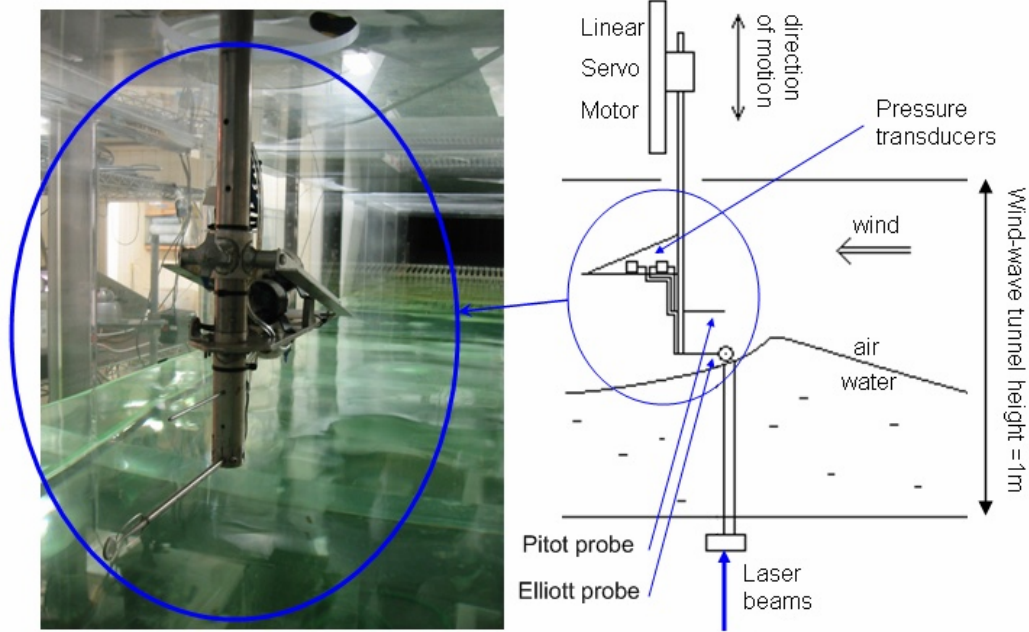
Figure 3.4. The wave follower system design.

The wave generator in ASIST is a flat vertical panel, moved horizontally by a hydraulic motor according to a pre-programmed trajectory. During these experiments the shape of the motor trajectory was exclusively a sine wave with various frequencies and amplitudes. The form of the resulting surface waves was carefully examined in a separate experiment. While for a high initial wave steepness generated waves expose some non-linearity, for the studied range (ak<0.2, where a is wave amplitude), first harmonics in the wave spectra was found to contain less than 1% of the wave energy and, therefore, generated waves were assumed to have pure sine shape. However, strong wind speed, studied in this work, deforms the wave shape by the time it reaches the fetch of pressure measurement. The effect of non-linear wave shape is investigated and discussed in detail in Chapters 5.d and 5.e.

To make the wave following possible in strong wind conditions, with spray and wave breaking present, a robust and fast response elevation gauge was developed. The new Digital Laser Elevation Gauge (DLEG) essentially is a vertical laser beam crossing

the water surface. Fluorescein added to the water makes the laser beam highly visible; this creates a brightness contrast as the beam crosses the air-water interface. A digital line scan camera looks at the beam through the tank's side wall. The brightness threshold location on a line image signifies the water elevation. While this technique provides the most accurate surface elevation measurement (maximum resolution <0.2 mm, maximum sampling rate 1000 Hz), it is vulnerable to the presence of whitecaps and spray (e.g. Fig. 3.5).
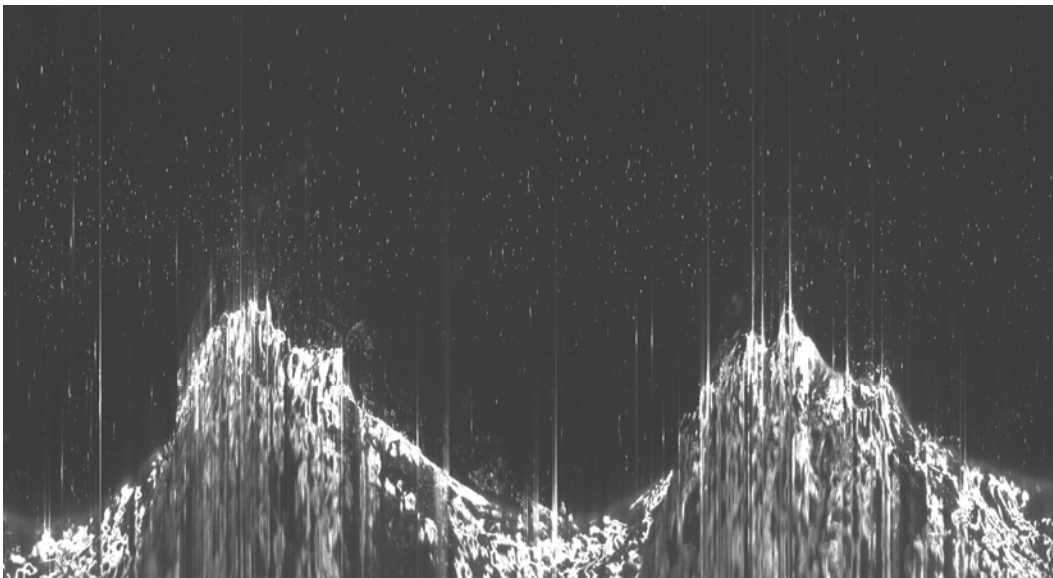
Figure 3.5. Unfiltered DLEG image of the air-sea interface at $U_{10} = 40$ ms^{-1}. Horizontal scale – time, vertical – height. Pixel size on this image is 0.2 mm vertical and 0.5 ms horizontal.

After the laser beam scatters over foam or a spray particle, a large part of its intensity is likely to be redirected into the camera. This can cause the entire vertical array of photoelectric light sensors to oversaturate resulting in vertical bright lines (Fig 3.5). While such an effect is harmful for the camera and makes the task of finding the water surface complicated, it has a potential of being an effective tool for spray concentration measurements. For the purpose of the current work, a light filter specific to the laser

beam wavelength was installed on each camera. It blocked the scattered light, but allowed the light intensity of a differing wavelength produced by the flourescein particles, excited by the laser beam.
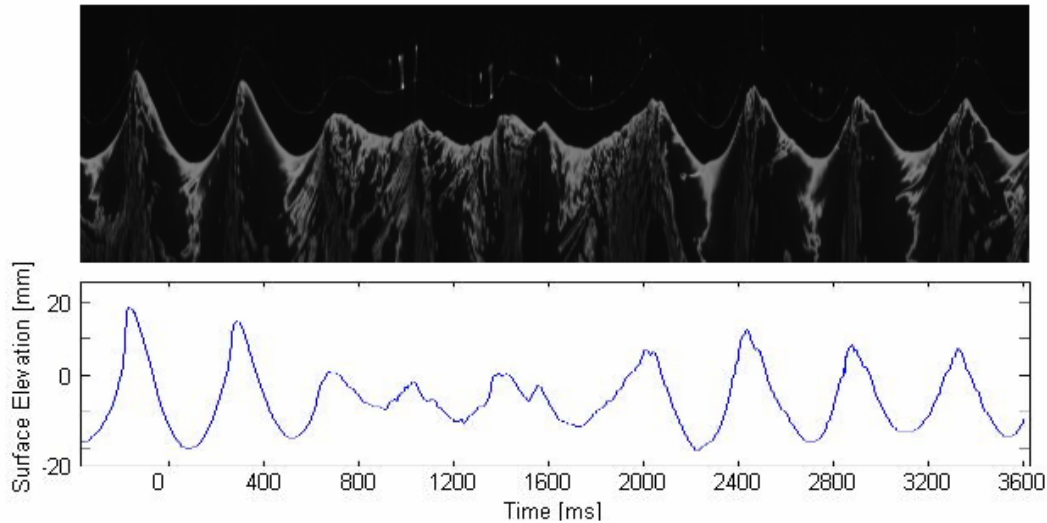
Figure 3.6. Example of a surface elevation signal acquired by a line scan camera. Top image represents multiple vertical scans stacked together. Bottom plot is the resulting water elevation time series.

While the scattered light filtering makes the water surface easier to detect, wave breaking inevitably distorts the surface elevation signal. A spike removal algorithm must be implemented after such measurements are taken. Recent advancements in digital imaging technology made it possible to implement such an algorithm "on the fly" during the experiment. Line images were acquired through a firewire board and processed by a code, written in National Instruments Labview, in real-time mode. The code had an edge detection algorithm (described in detail in Chapter 3.c), and thus provided a clean surface elevation signal without wave breaking related spikes (Fig.3.6). It was critical to have the surface elevation signal processed, cleaned and calibrated at the same instant it was

measured, because it had to be used immediately as a reference coordinate for the vertical motor.

The heart of the wave follower was a linear servo motor (manufactured by Northern Magnetics) with its programmable controller. To provide the optimal following trajectory, every time step, in addition to a new water elevation coordinate, the current motor position was considered to make a new motion decision. This allowed smooth reattachment of water elevation and wave follower trajectories and limited unnecessary vibrations. The key principle behind the smooth motion was that instead of position, only velocity of the motor was controlled. Every time step it was chosen as

$$U = \frac{X_w - X_m}{\Delta t},$$ (3.1)

where X_w is the current surface elevation, X_m is the current motor elevation and Δt is sampling time step. This allowed the motor to be in constant motion and thus eliminated stop and go vibration, or "jerking" problem, which is harmful for the motor and pressure sensors and introduces noise in the pressure signal.

Multiple digital and mechanical actions, necessary between an instant of an actual surface elevation and an instant of the wave-follower reproduction of that elevation, produced a 30 ms following lag. This lag could not be neglected, because given the low following trajectory, at a steep slope of a wave the location of the probe will intersect the water surface , causing the flooding of the pressure probe. To remove the lag, another elevation gauge was installed 4 cm upwind of the location of the pressure probe and was used to drive the motor. A typical wave phase speed during this experiment was about 1.5 ms^{-1}, therefore ~27 ms in advance notification was sufficient to compensate for the lag and to keep the probe above the water.

The follower motion repeated the water surface elevation with good precision: depending on wave conditions, particularly maximum vertical acceleration, the wave follower position was within 1-3 cm above the surface. An example of water surface elevation and motor position spectra are shown on Fig.3.7. Although, motor elevation information is available within the motor controller, it was also measured by means of another line scan camera, focused on an LED light source on the moving part of the motor. Since all cameras were centrally triggered this was essential to obtain both water surface and motor elevation at the same time.
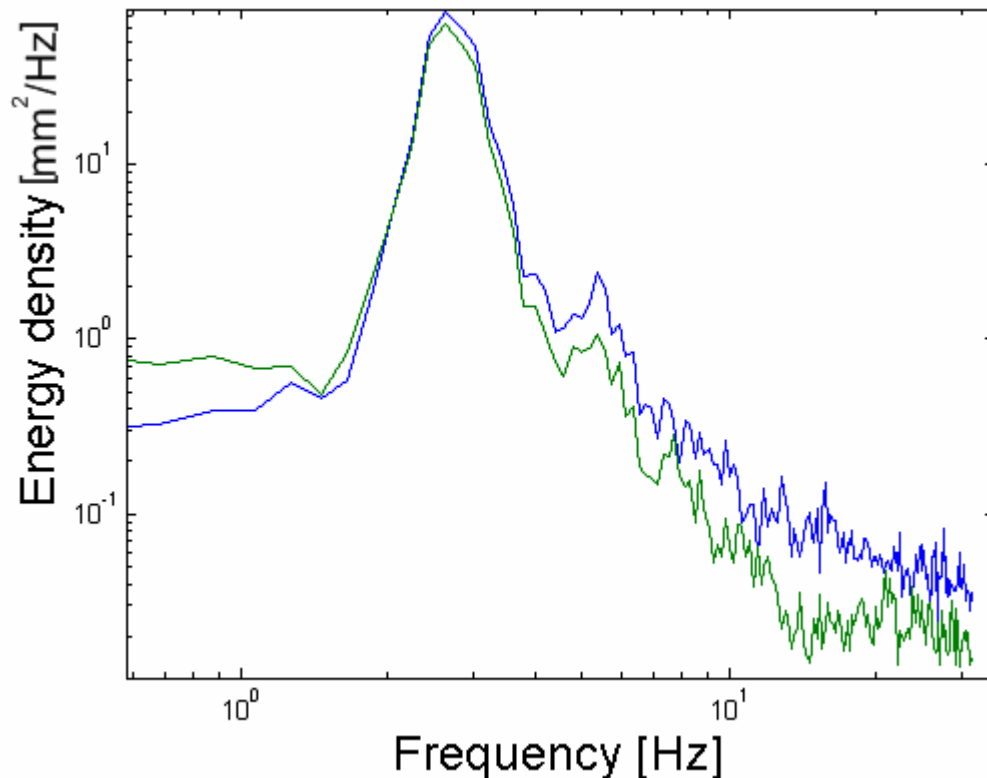
Figure 3.7. Water surface elevation spectrum (blue), wave-follower motor position spectrum (green).

In addition to the surface elevation gauge used to drive the motor, another elevation gauge was installed directly underneath the Elliott pressure probe. Its signal together with the motor positioning signal provided the most vital elevation information,

as they are the ones used further in the data analysis. The challenge of measuring surface elevation directly underneath the pressure probe is that a part of the laser beam is reflected by the probe (Fig. 3.8). To avoid such bright reflection, the light filter was first installed on the camera; and the laser beam was then displaced about 2mm away from the probe in the cross-tank direction. In the final configuration, occasional reflections were still visible (i.e. Fig. 3.6.), but were filtered out by an edge-detection algorithm (described below) during the post processing. Although, Figure 3.8 does not represent the final configuration, it is shown, because it is the most accurate way to illustrate the performance of the wave follower, as both the surface and the motor elevations are shown on one image. Note how well the motor trajectory reproduces the surface waveheight, which is about 2cm in this case. The offset of the motor trajectory is arbitrary and it is only the deviation between the probe and the motor positions that limits the proximity at which the surface can be followed. In this case the following can be performed at as low as about 5-10 mm height from the surface. In comparison, previous wave-follower based studies (e,g., Snyder et al. 1981) report ~5 to 10 cm following height.
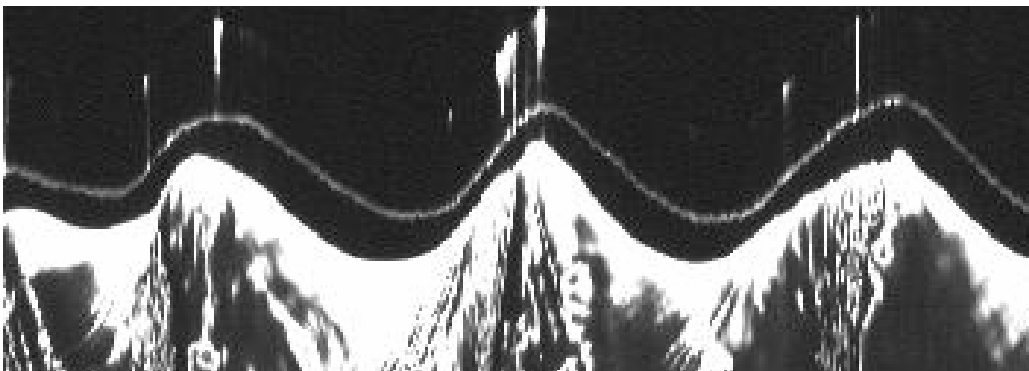
Figure 3.8. Digital laser elevation gauge underneath the Elliott pressure probe. White solid line above waves – laser light reflected from the bottom of the pressure probe.

Given the information about the motor and the water elevation allows collecting all measured points on one plot, resolved in terms of phase of a dominant surface wave. Details of this procedure are described in chapter 4. On Figure 3.9 a summary of a 30min sample is shown to evaluate the following performance. Nearly all data points fluctuate within 10±5 mm from the surface with the follower set to be 10mm above the surface. The mean wave surface slope was obtained by wave phase averaging over the random wind wave field, in which the shape of the wave surface is not constant.
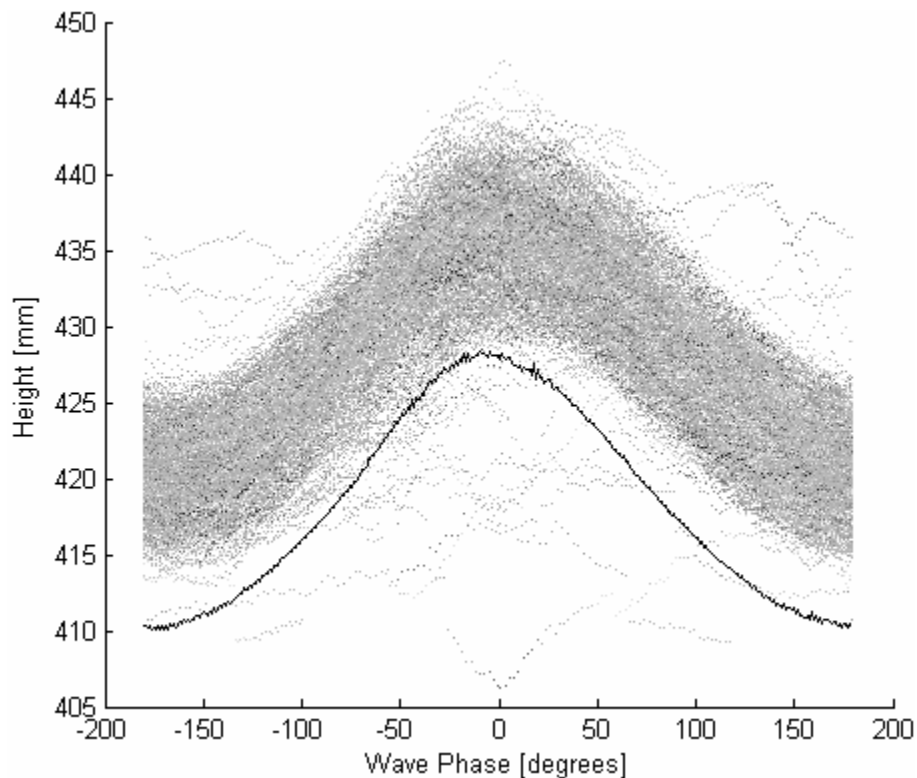
Figure 3.9. Wave-follower positions (points) above mean surface of a dominant wave (solid line), both summarized over 30 minutes long run. Some points appear to be underwater due to imperfections in phase calculation of random wind wave field or due to the wave-follower motion error.

The static pressure "Elliott" probe is essentially a metal disk 2 cm in diameter with an inlet in the middle of each side. Both inlets are connected to a single pressure

transducer (Fig. 3.10). The shape of the probe is such that airflow, disturbed by the disk edge, restores by the time it reaches the center of the disk. This ensures that the measured pressure is static pressure, as long as the wind direction is within $\pm 12^\circ$ of the disk plane. Detailed information on the probe design and specifications can be found in Elliott (1972b) and Donelan et al. (2005a). A discussion on various static pressure probes and corrections associated with them is given in Wyngaard et al. (1994). In ASIST for the given experimental setup, the dominant wind speed components are in the vertical and along-tank directions. Thus, the disk was mounted vertically in the along-tank direction on the bottom of the wave following vertical shaft. In addition, due to the smaller scale of the experiment, the size of the manufactured probe was reduced by a factor of 2, compared to that of the original design.

Occasionally a wave breaker or spray resulted in flooding of the pressure probe. Such events were detected by means of monitoring the raw pressure signal during the experiment. The presence of water in the probe reduced the magnitude of pressure fluctuations (Fig.3.11) and, therefore, was easily detectable. In such cases remotely operated control valve was switched to a source of high pressure, which cleaned the probe with a backflow. Within 2-3 seconds after the cleaning the pressure probe was reconnected to the pressure transducer. This allowed continuation of the experiment without long interruptions even in conditions with severe wave breaking and spray generation. In the post processing stage, pressure data around such events, including segments two seconds before and after the event were taken out. Such spike removal was not found to introduce any wave-coherent errors to the final results.
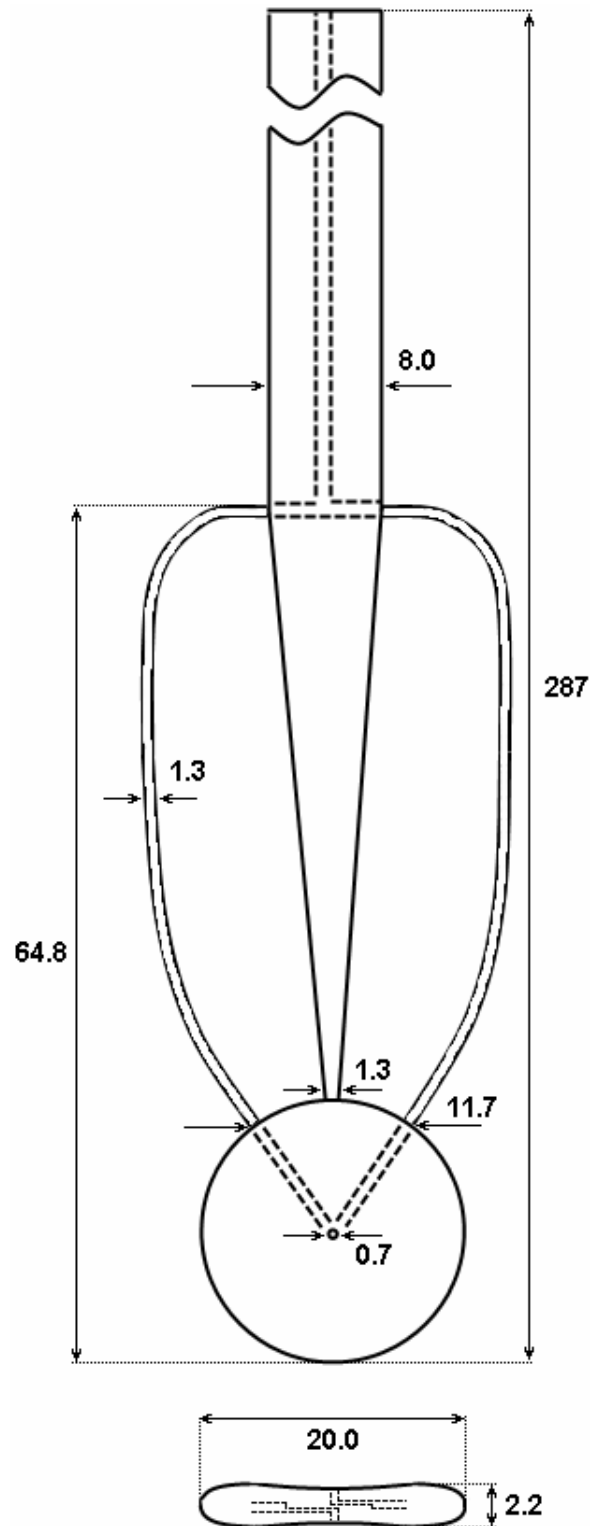
Figure 3.10. Static pressure probe used in this study. It is based on the design by Elliott (1972a) with the disc diameter reduced by a factor of 2. All dimensions of the probe used in this work are shown in the figure in [mm].

The static pressure difference between windward and leeward sides of a wind wave was found to be in the 1 to 30 Pa range. At such small fluctuation magnitudes, several factors can influence the pressure measurements and need to be accounted for in experimental approach.
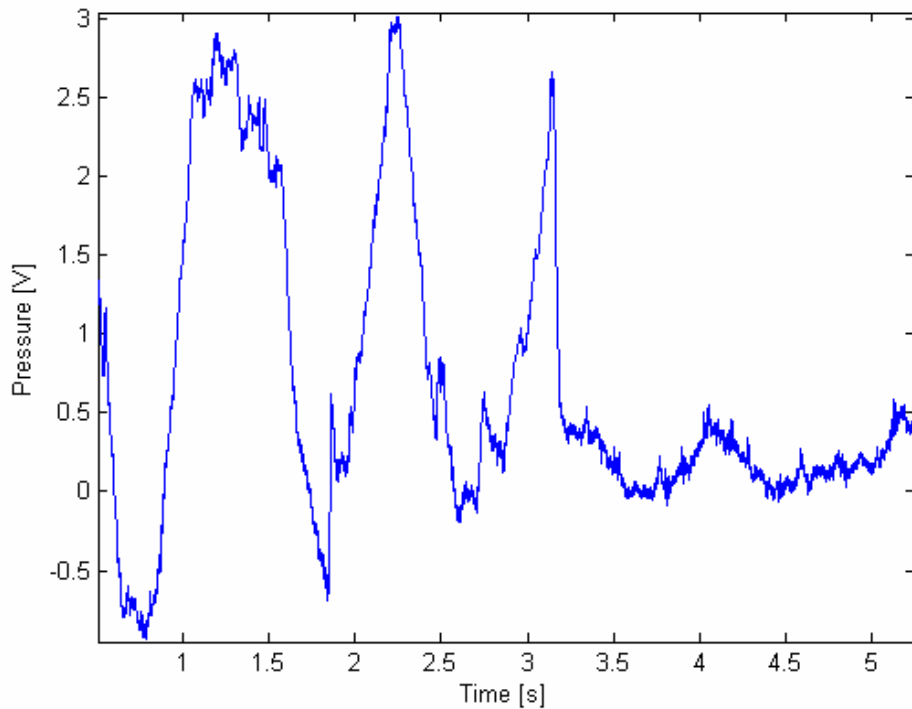
Figure 3.11. An example of the raw analog signal output from the pressure transducer during a probe flooding event (~3.2 s).

First, due to the wave-follower acceleration, additional pressure is generated in the vertical air column that connects the "Elliott" probe and pressure transducer. The additional pressure is approximately given by (Snyder et al. 1981):

$$\Delta p_f = \rho_a a_f \Delta h / 2 , \qquad\qquad (3.2)$$

where ρ_a – air density, a_f – wave-follower acceleration, Δh – vertical length of the air column. In previous works (e.g. Donelan et al. 2005a) the pressure transducer was

mounted at a safe distance (1.28m) from the probe to protect the electronics. This resulted

in a large Δh values, hence the fluctuations of the Δp_f correction (eq. 3.2) were

comparable to the amplitude of the static pressure fluctuations. To minimize the errors

due to acceleration, an advanced dynamic calibration had to be performed. However, a

different approach was taken here. That is, the pressure transducer and other supporting

electronics were installed directly on the moving part of the wave-follower as close to the

pressure probe as possible (Fig.3.4). This reduced the value of Δh to 0.1m, and therefore

the pressure correction value (eq. 3.2) was typically within 1% of the pressure signal.

Second, the hydrostatic atmospheric pressure correction is given by:

$$\Delta p_a = -\rho_a gh, \hspace{4cm} (3.3)$$

where h represents the vertical position of the pressure probe. Fluctuations in hydrostatic

atmospheric pressure along the surface of a wave do not result in momentum flux, as the

correlation of such pressure with surface slope results in zero. Nonetheless, the correction

was applied for the purpose of studying the vertical decay of pressure fluctuations.

Third, a correction was made due to finite membrane inertia and noise cancelling

electronics within the pressure transducer, and also due to the finite time of pressure

wave propagation between the Elliott probe and its pressure transducer. These amplitude

and phase lags dependence on frequency were studied using a controlled pressure

chamber (Fig.3.12). Pressure in the chamber was generated by a saw-tooth signal, shown

on figure 3.13 as a green line and the response of the pressure transducer is shown as a

blue line. The response was decomposed in Fourier space and is shown on Figures 3.14

and 3.15 in the form of amplitude-frequency and phase-frequency response functions.

Corresponding least mean square fits, forced to pass a non-disturbed point at $f = 0$ Hz are
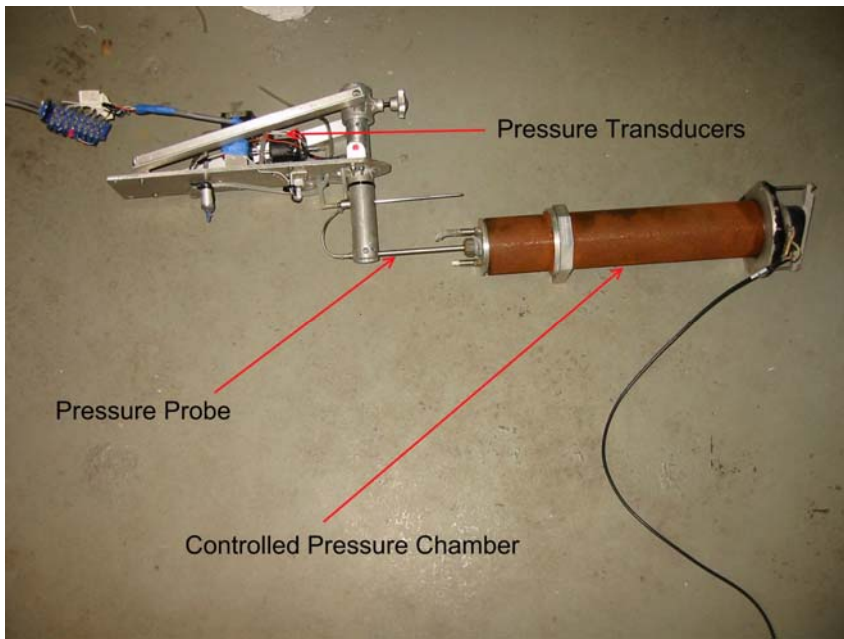
Figure 3.12. Pressure sensor dynamic calibration. The "Elliott" probe is placed within the controlled pressure chamber.
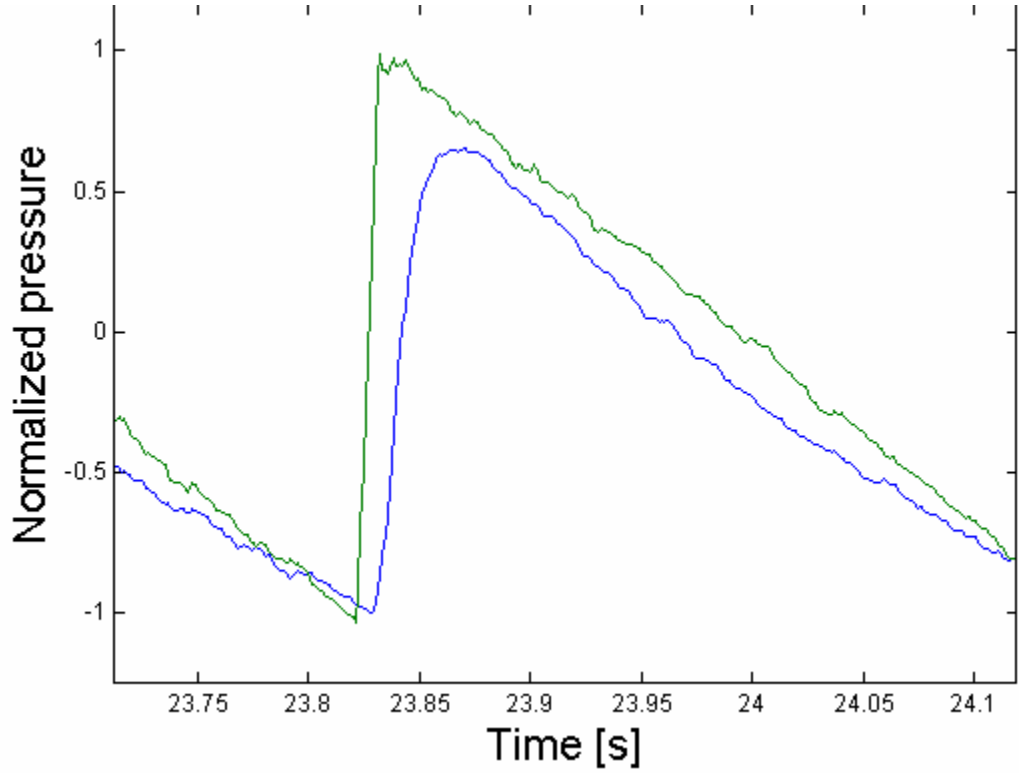
Figure 3.13. Saw tooth signal used for dynamic calibration in the controlled pressure chamber. Green line – pressure signal fed to the chamber, blue line – pressure transducer response.

shown as solid lines (i.e. phase lag approached 0 and amplitude correction approached 1 as frequency approached 0 Hz). The form of these functions is similar to the original calibration, performed by Elliott (1972b, Figure 5). These response functions were applied in Fourier space to all pressure data collected during experiments.
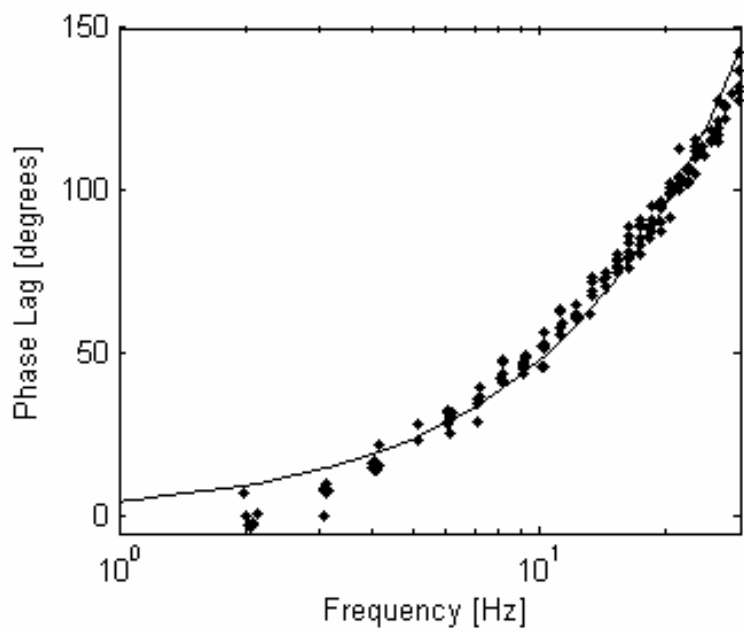
Figure 3.14. Pressure measurement's phase-frequency response function.
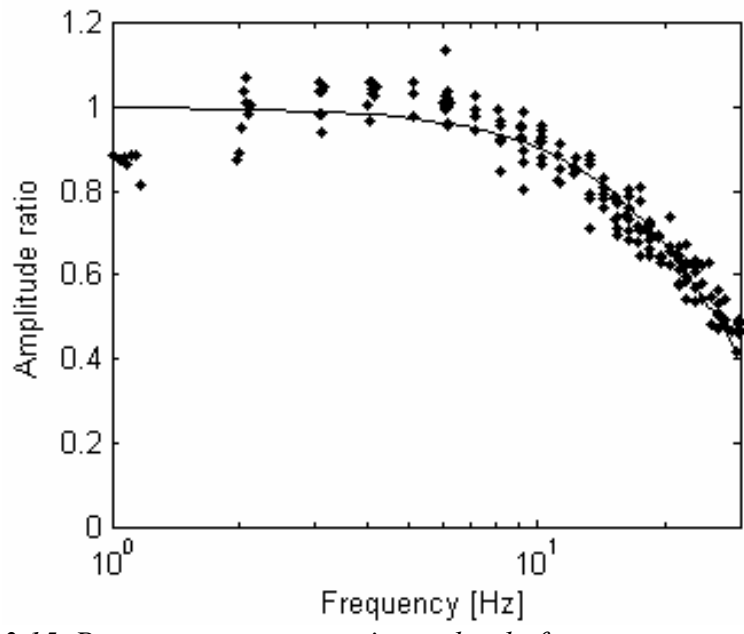
Figure 3.15. Pressure measurement's amplitude-frequency response function.

Table 1. Summary of wave-follower experiment runs. U_{10} is wind speed at 10m height, $U_{\lambda/2}$ is wind speed at half the wave length height, C_p is wave phase speed, a, k is wave amplitude and number, $<p\,\partial\eta/\partial x>$ is momentum flux, γ is spectral wave growth function.

Run #	U_{10} ms^{-1}	$U_{\lambda/2}$ ms^{-1}	C_p ms^{-1}	ak	k $[m^{-1}]$	$<p\dfrac{\partial\eta}{\partial x}>$ $[Pa]$	γ
1	11.0	8.6	1.48	0.097	4.26	0.261	14.5
2	15.0	11.4	1.48	0.116	4.26	0.564	26.2
3	19.1	14.0	1.48	0.147	4.26	1.307	45.4
4	23.1	16.5	1.48	0.152	4.26	2.314	61.9
6	23.1	16.5	1.48	0.120	4.26	1.098	46.7
7	19.1	14.0	1.48	0.108	4.26	0.816	52.1
8	15.0	11.4	1.48	0.094	4.26	0.338	26.4
9	11.0	8.6	1.48	0.079	4.26	0.137	13.5
11	11.0	8.6	1.48	0.052	4.26	0.062	14.5
12	15.0	11.4	1.48	0.052	4.26	0.104	22.2
13	19.1	14.0	1.48	0.066	4.26	0.396	64.0
14	23.1	16.6	1.48	0.095	4.26	1.067	82.0
16	8.2	6.8	1.71	0.032	2.76	0.018	8.6
17	12.9	10.4	1.71	0.033	2.76	0.046	22.1
18	17.6	13.8	1.71	0.032	2.76	0.070	34.8
19	22.2	17.0	1.71	0.037	2.76	0.131	62.6
20	26.9	20.1	1.71	0.038	2.76	0.113	41.1
22	8.2	6.8	1.71	0.061	2.76	0.059	7.7
23	12.9	10.4	1.71	0.060	2.76	0.159	20.1
24	17.6	13.8	1.71	0.065	2.76	0.218	27.5
25	22.2	17.0	1.71	0.074	2.76	0.432	50.4
26	26.9	20.1	1.71	0.072	2.76	0.454	41.3
29	12.9	10.4	1.71	0.094	2.76	0.259	15.6
30	17.6	13.8	1.71	0.097	2.76	0.498	27.7
31	22.2	17.0	1.71	0.091	2.76	0.803	47.3
35	12.4	9.2	1.24	0.084	6.35	0.259	24.2
36	9.7	7.3	1.24	0.072	6.35	0.112	14.0
39	12.4	9.2	1.24	0.040	6.35	0.058	24.8
42	20.5	14.1	1.24	0.066	6.35	0.295	43.1
43	20.5	14.1	1.24	0.141	6.35	0.949	32.5
44	17.8	12.5	1.24	0.103	6.35	0.317	19.9
45	7.0	5.4	1.24	0.058	6.35	0.034	6.7
46	20.5	14.1	1.24	0.115	6.35	0.825	42.1
47	17.8	12.5	1.24	0.083	6.35	0.317	29.4
48	15.1	10.9	1.24	0.093	6.35	0.285	24.0
49	9.7	7.3	1.24	0.061	6.35	0.069	12.4
50	12.4	9.2	1.24	0.071	6.35	0.142	18.8
51	19.1	14.0	1.48	0.162	4.26	2.178	52.0
52	19.1	14.0	1.48	0.190	4.26	2.345	36.1
53	19.1	14.0	1.48	0.028	4.26	0.079	56.1

The experiment summary is listed in Table 1. Each experiment was approximately 30 minutes in duration. Various wind speed and mechanically generated wave conditions were held constant during each run. The wave steepness *ak* is given for the wave of the generated frequency, where *a* is wave amplitude at the fetch of the pressure measurement. Wind speeds at 10 meters height and at *λ/2* (half of the wave length) height references were calculated using the logarithmic wind profile assumption.

c. *"Particle Image Velocimetry" based current profiles measurements.*

The Particle Image Velocimetry (PIV) technique was used to obtain the vertical and along-tank components of water velocity vector maps. For this purpose, water was seeded with polyamide spheres (50 μm diameter) and illuminated by two consecutive laser sheet pulses 10 to 15 ms apart. The laser sheet was positioned vertically along the centerline of the wave tank, at ~6.6m wind fetch. A digital "Hisense" camera synchronized with laser pulses recorded pairs of consecutive images.

The basic technique used for PIV image processing is based on a cross-correlation algorithm, where the image is split into multiple target areas typically 16x16 or 32x32 pixels each and a cross-correlation function is computed for each pair of corresponding target areas from two frames. The location of the peak of the cross-correlation function yields the fluid displacement within the target area during the time between two laser pulses. The limitation of the "cross-correlation" approach is that if a significant amount of particles has left a target area between the pulses, its cross-correlation peak is likely to produce an incorrect velocity estimate. Therefore, target areas must be kept large, but spatial resolution is reduced.

In this work, the "adaptive correlation" technique, developed by Dantec Dynamics Inc., was used to determine average particle displacement during the time lag between pulses. The adaptive correlation algorithm is more complex, but it is based on the same principle. If the desired resolution is NxN pixels, it starts by computing rough estimates of fluid velocity, i.e., 4Nx4N target area sizes. Once raw velocities are known, the resolution is increased to 2Nx2N. This time target areas are chosen with a spatial shift between two frames, according to the known larger scale fluid velocity in the area. Once the second iteration step is complete, a third iteration step refines the resolution further to NxN pixels. The number of iteration steps and final resolution are flexible. The resolution NxN can be as fine as 8x8 or 4x4 pixels, and this method is less likely to produce an error in the velocity vector estimate. An example of an output of the adaptive correlation and cross-correlation algorithms is shown for comparison in Fig 3.16.

While adaptive correlation produces clearer results, occasional spikes are unavoidable, especially near a rough air-sea interface. For the purpose of spike removal a simple moving average window validation was applied to all vector maps to filter out outliers.

In addition to PIV image acquisition, multiple surface elevation measurements were performed. Digital laser elevation gauges (DLEG) were installed upwind and downwind from the PIV location (5.77m and 8.67m wind fetch) to monitor wind wave spectra evolution. And another surface elevation measurement technique was developed and implemented to resolve the surface location above each PIV frame.

A video camera, identical to the "Hisense" camera used for PIV, looked at the intersection line between laser sheet and water surface (Fig 3.17). Synchronized with

laser pulses, similar to laser elevation gauges, it provided water elevation information along the laser sheet above each PIV image.
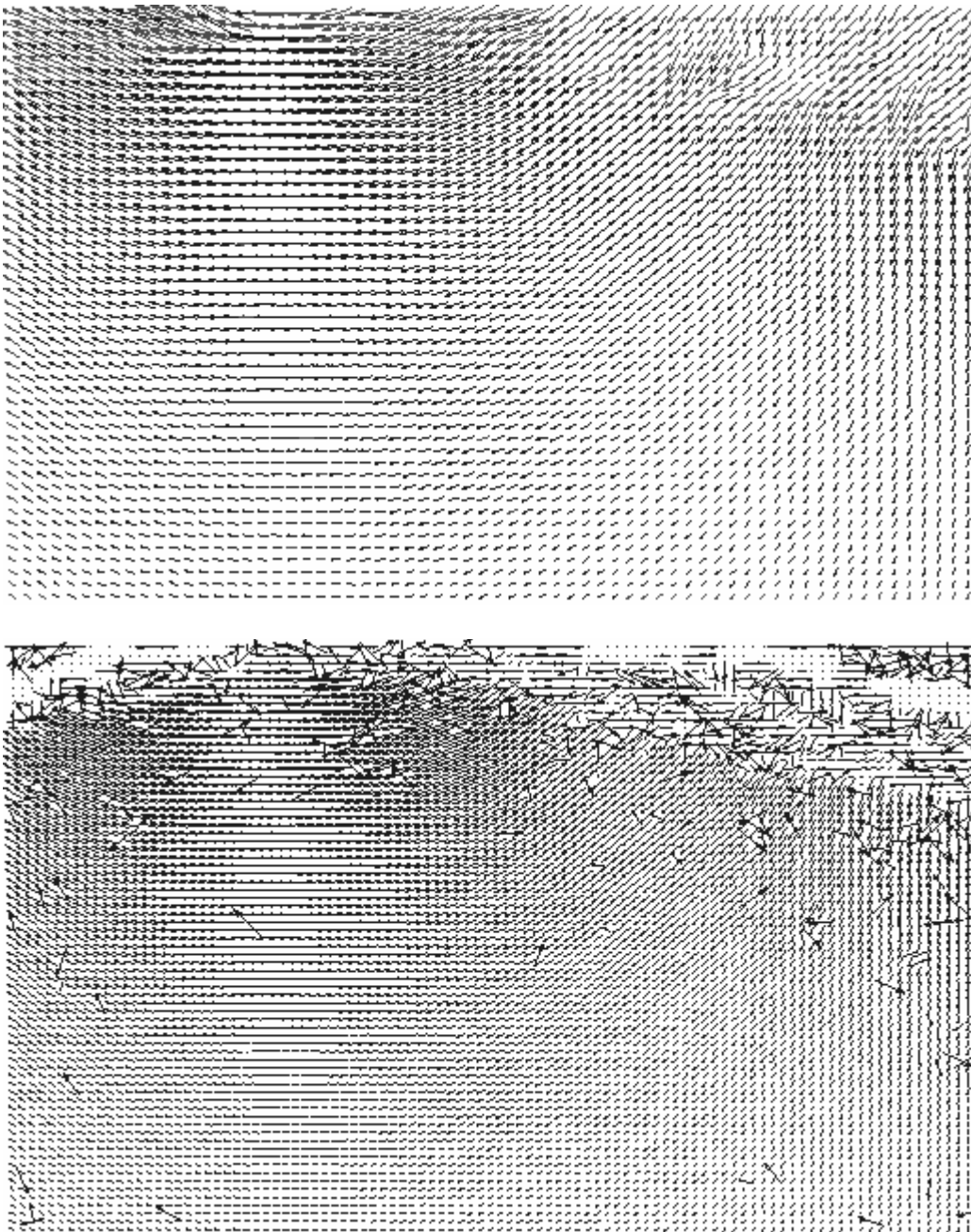
Figure 3.16. Velocity vector map, deduced from PIV images using a simple cross-correlation algorithm (bottom) and adaptive correlation algorithm (top) provided by Dantec Dynamics in its Flowmanager software. The adaptive correlation algorithm gives a much clearer result. The frame size is 10x7 cm.
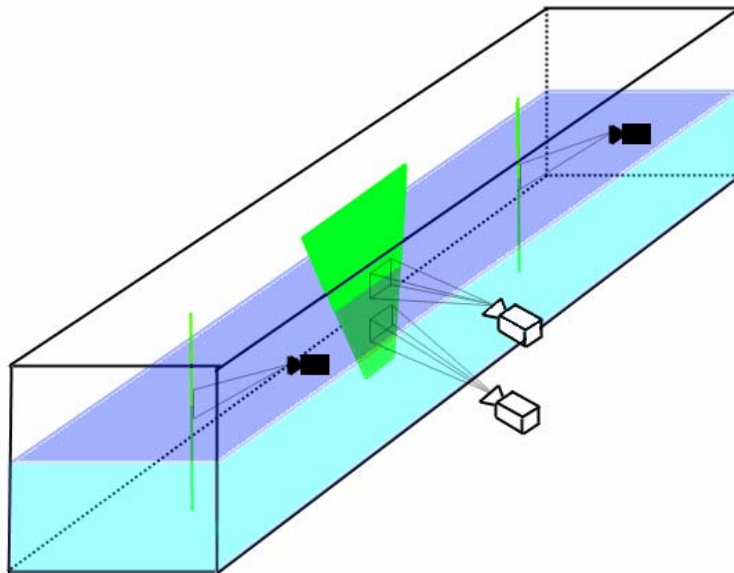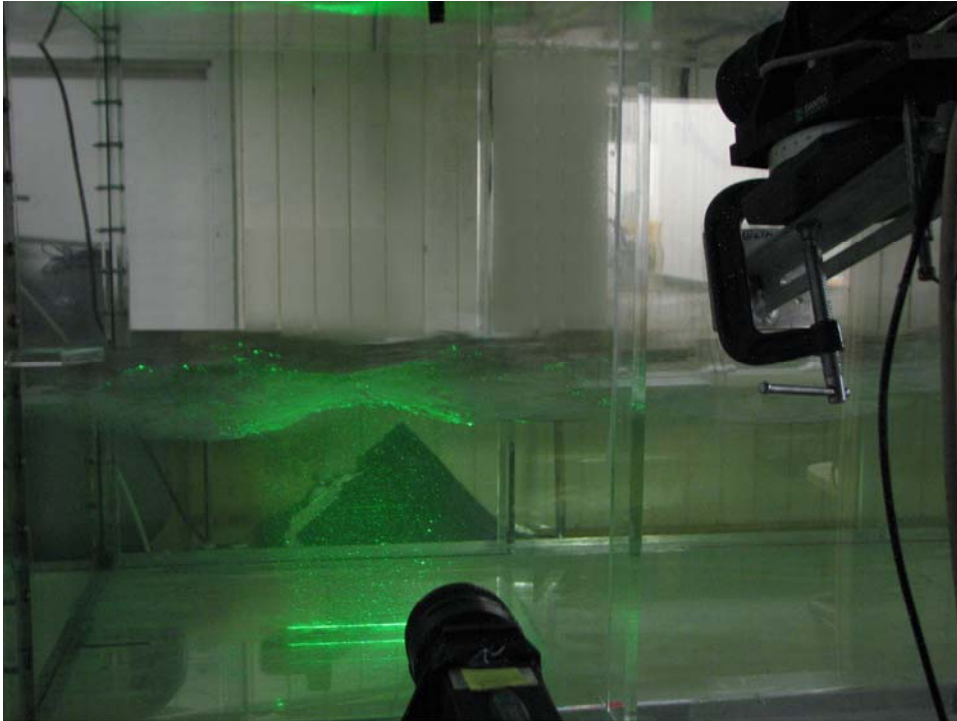
Figure 3.17. PIV and Elevation gauges setup. Top: two "Hisense" cameras looking at the laser sheet: one used for PIV, another resolves surface elevation. Bottom: sketch of the experimental setup. "Hisense" cameras are shown in white. Line scan cameras, used for DLEG are shown in black.

Examples of the resulting images of the water surface are shown in Figure 3.18 (left) and Figure 3.19 (top left). Horizontal brightness edge in such images, shown in by the red line in Figure 3.18 (right) provided information on water surface elevation above each column of PIV resolved velocity vector maps. While the edge is clear in smooth surface conditions (i.e., Fig. 2.10), in the presence of the wave breaking related foam and spray, surface edge detection poses a significant challenge. And since thousands of images were acquired during the experiment, manual quality control of edge detection was out of the question.

An advanced edge detection algorithm was developed specifically for the purpose of water surface measurements in rough wind-wave conditions. The development of this algorithm was also justified by the necessity of line scan image processing within the DLEG technique. Therefore, the same algorithm was used within two techniques for two different experiments.
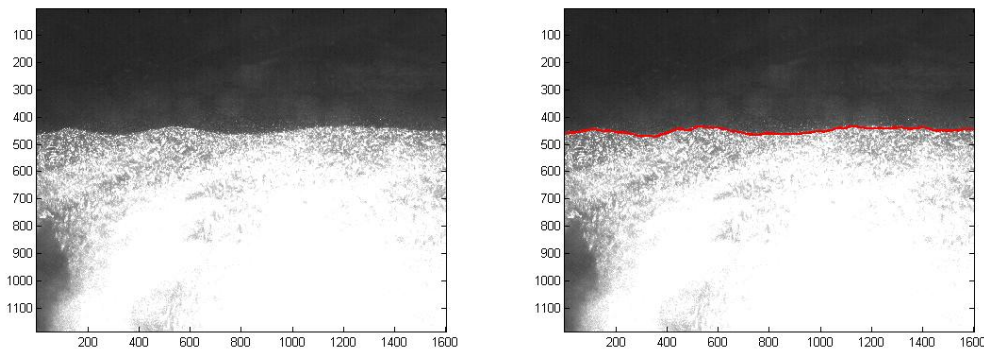
Figure 3.18. Edge detection in smooth surface case. Original image on the left, original image with the overlaid processed elevation (red line) on the right. Scale is shown in pixels.

The idea behind the edge detection algorithm was to attempt to reconstruct the logic a human would use to find an edge on such images. There are two main challenges

that a rough surface poses for edge detection: first, spray particles are as bright as the surface and have a risk of being recognized as such; second, wave breaking foam, attached to the surface, misrepresents the actual water elevation. Both of these features, however, are easily identified by a human eye (i.e. Fig.3.19 top left). To deal with the first problem, an image is defocused, where its resolution is decreased by a factor of 64x64. Because spray particles are small, their high brightness has little impact on mean brightness of 64x64 pixel areas. On such a defocused image, a rough estimate of the brightness edge can be easily found without the risk of spray contamination.

While the rough surface edge estimate effectively deals with spray, it would still have an error due to the foam. To filter that effect out, a critical surface wave curvature criterion was used. If the curvature of a rough surface elevation signal $\frac{\partial^2 \eta}{\partial x^2}$ exceeded a critical value, such points were considered contaminated by the foam and were replaced by a function, smoothly filling the gap. Such function was found using small smoothing iterations, starting with unchanged function until the curvature criterion was satisfied. The curvature threshold was optimized individually for each run, depending on wave conditions (i.e., expected maximum crest sharpness). In the image dimensions the typical critical curvature value was one vertical pixel per one horizontal pixel per one horizontal pixel. Whether the replacement in form of a smooth function actually represents the true surface is an open question, as the air-water interface line does not exist within the foam. The described method, however, gives a good estimate on where the surface would have been in the absence of foam.

Once the first rough step of the edge detection is complete (i.e. Fig 3.19 top right), the image resolution is increased by an arbitrary factor and the same edge detection

principle is applied for the part of the image within close proximity to the rough elevation estimate (Fig.3.19 bottom left). The second step has the highest computation cost, therefore such reduction in edge search area improves algorithm efficiency, and it also reduces a chance of picking up an edge somewhere within air or water away from the surface. The third step increases the image resolution to the maximum and simply interpolates the surface elevation curve to provide elevation data for each pixel column of the original image (Fig.3.19 bottom right).
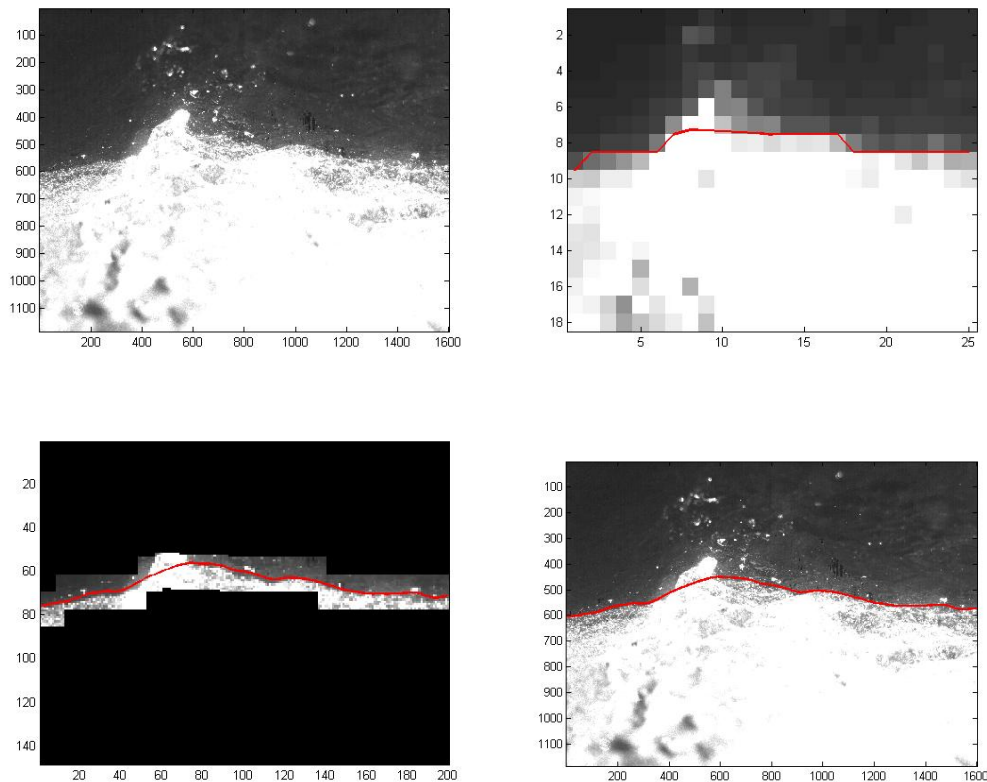
Figure 3.19. Edge detection in rough surface case. Top left – original image, top right – defocused image with rough edge estimate, bottom left – fine resolution edge detected within vicinity of rough estimate, bottom right – final surface elevation (red line), the final elevation line cuts off a piece of foam. Scale is shown in pixels.

d. Bulk measurements of the total air-sea momentum transfer in a wind tank.

The most common way of measuring total air-sea momentum flux is by

measuring turbulent velocity fluctuations above the wave boundary layer. In a wave tank,

however, the layer often extends all the way to the ceiling. But other methods, impossible

to perform in the field, are easily accessible in a laboratory setup.

A number of effective methods exist: in this work we use one called "momentum

budget" (Fig.3.20, taken from Donelan et al. 2004, figure 1).
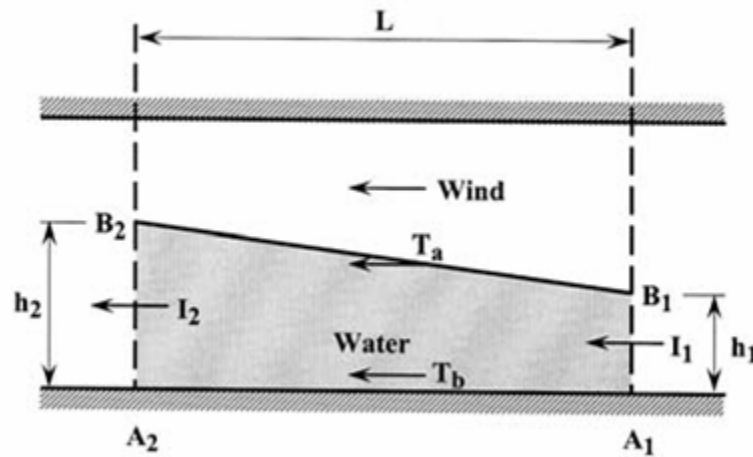
Figure 3.20. The flux of horizontal momentum in and out of a control volume (shaded area) of a wind-wave tank. The variables are defined in the text.

The idea of the method is to select a volume of water in a tank and to measure

total horizontal momentum flux in and out of the volume. The law of momentum

conservation yields

$$I_2 - I_1 = T_a + T_b. \qquad (3.4)$$

Here T_b is the stress induced by the bottom friction, T_a is the air-sea momentum flux,

related to flux per unit length by $T_a = \tau L$; I_1 and I_2 are incoming and outgoing fluxes on

the sides of the control volume. The difference, I_2-I_1, is composed of the water level surge,

surface pressure difference, and wave radiation stress difference terms:

$$I_2 - I_1 = \frac{1}{2}\rho_w g((h_2{}^2 + \sigma_2^2) - (h_1{}^2 + \sigma_1^2)) + h(p_2 - p_1), \qquad (3.5)$$

where σ is the standard deviation of the surface displacement due to waves, p is the air pressure, h is the mean water level in the tank. Previous measurements by Donelan et al. (2004), performed in the same tank with maximum wind speed up to twice higher than in the present work, reported that the bottom stress (due to friction of the return current) never exceeded 2% of I_2 - I_1; therefore in present calculations it will be disregarded for the sake of simplicity. This gives the final equation for the total air-sea momentum flux per unit length:

$$\tau \approx \frac{1}{L}(I_2 - I_1) = \frac{1}{L}(\frac{1}{2}\rho_w g((h_2{}^2 + \sigma_2^2) - (h_1{}^2 + \sigma_1^2)) + h(p_2 - p_1))$$
$$= h(\rho_w g s + \Delta p / L) + \rho_w g \Delta(\sigma^2)/2L \qquad (3.6)$$

where s is the mean water surface slope, Δp is the pressure difference, $\Delta(\sigma^2)$ is the wave spectrum's total energy change. Thus, such measurements of the total wind stress only require pressure and surface elevation sensors in two ends of the control volume.

Chapter 4: Data Processing

a. Wind – wave momentum transfer.

The wind-wave momentum flux is calculated as the correlation between the static pressure at the surface and the surface slope (eq.2.2). Such an approach yields in momentum flux from wind to the entire wave field. But for the purpose of spectral wave modeling, it is more desirable to resolve momentum flux from wind to each wave frequency separately, so that

$$\int_\omega M(\omega)d\omega = \tau^w , \qquad (4.1)$$

where τ^w is the total wind-wave momentum transfer. To study each frequency separately, pressure fluctuations coherent with a particular wave frequency must be isolated. For this purpose a band-pass filter is used in Fourier space to isolate the surface elevation of a particular frequency and then the Hilbert transform

$$H(u)(t) = -\frac{1}{\pi} \lim_{\varepsilon \downarrow 0} \int_\varepsilon^\infty \frac{u(t+\tau) - u(t-\tau)}{\tau} d\tau. \qquad (4.2)$$

is applied to it. The Hilbert transform produces a function orthogonal to the original signal, i.e., inner product of the original signal and its transform is zero. An angle, given by the complex number, where the real part is the signal and imaginary part is its Hilbert transform, is interpreted as the wave phase of the original signal (Bendat and Piersol 1986).

Once the phase of the wave in question is determined for each data point of each 30 minute run, the reconstruction of average, phase resolved wave periods begins. The wave phase (over 360°) is split into 5° bins and all available pressure and elevation data

points are separated according to these bin widths. Averaging data points within each bin is important to isolate wave coherent processes. Any process, unrelated to this particular wave frequency, including turbulent fluctuations of pressure and surface elevation fluctuations due to waves of other frequencies on average results in a zero contribution.

While mean surface elevation is calculated by averaging within each bin, an additional step is required to determine the value of the static pressure at the surface. Since the pressure is measured at a small, but finite and slightly fluctuating height, it must be extrapolated to the surface. However, the exact form of the extrapolation function is unknown

$$p_0 = f(p, z, k) \text{,} \qquad (4.3)$$

where z represents the pressure probe's instantaneous elevation, p is measured pressure and k is wave number. Potential theory, as well as previous vertical array measurements (i.e., Snyder 1974), suggest a vertical dependence of

$$p = p_0 e^{-\alpha k z} \text{,} \qquad (4.4)$$

where α is a constant, which is to be determined empirically. Since this study emphasizes strong wind forcing, there is no certainty that equation 4.4 still holds. Therefore, the vertical decay function must be fully investigated. For this purpose, for each run an averaged function $p(\Theta, kz)$ was measured, where Θ represents the phase of the investigated wave. To obtain $p(\Theta, kz)$, each run was conducted for up to 30 minutes, while wind and wave conditions were held constant. During each run, the pressure was sampled at a range of heights starting from the closest non-wetting height
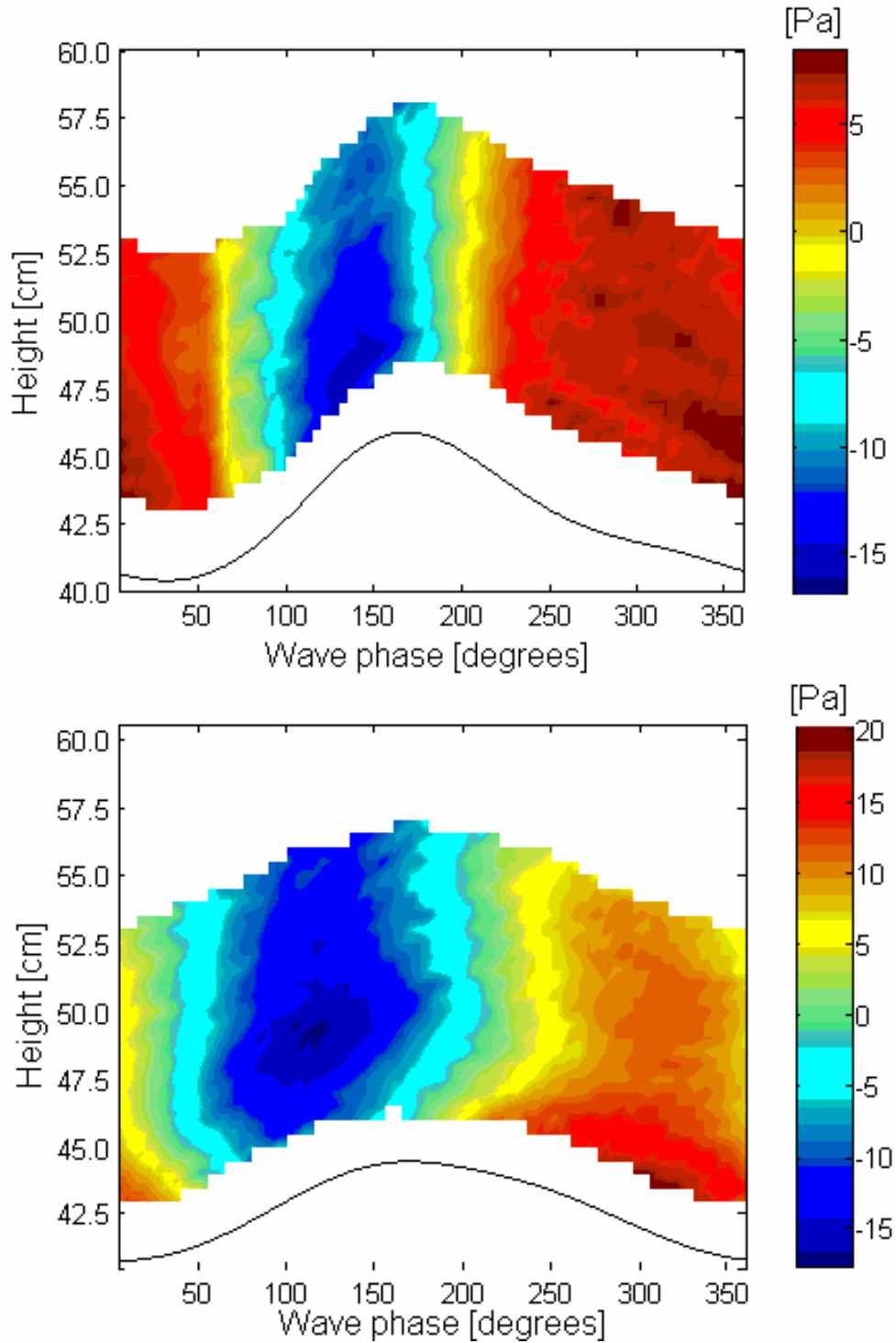
Figure. 4.1. Two examples of a phase resolved airflow pressure fluctuations $p(\Theta, z)$ above the mean wave surface (solid line), the wind and waves propagate from right to left. On the top is a typical case with $U_{10}/C_p = 10.1$ ($k=4.26m^{-1}$, $ak = 0.116$), on the bottom is an extreme wind forcing case $U_{10}/C_p = 16.6$ ($k=6.35m^{-1}$, $ak = 0.115$) exposing strong airflow separation.

(~1 to 3 cm) and up to about 1/10 of the wave length. Thus, pressure measurements collected and averaged within each 5° wave phase and 5mm height area provided points for pressure extrapolation to the surface.

Two typical examples of $p(\Theta, z)$ are shown in Fig. 4.1. The vertical pressure profile was observed to vary with wave phase. Sometimes, it has a local minimum above the leeward side of the wave crest. This effect is consistent with the expected behavior due to airflow separation.

To obtain pressure value exactly at the surface, available data points above each wave phase were linearly extrapolated to the surface. Linear extrapolation was chosen due to close proximity to the surface, where vertical pressure decay can be approximated as linear. Surface pressure values p_0 were further used to reconstruct vertical pressure profiles using exponential approximation $p = p_0 e^{-\alpha k z}$ profile ($\alpha = 1$), the profiles are shown in Figure 4.2. The figure qualitatively resembles the original pressure field to some extent, however, it can not account for airflow separation and small-scale features. Such a comparison also allows one to calculate the extrapolation error that happens due to the exponential decay assumption with constant α of ≈ 1. The source of the error here is not only the unknown α, but also the distortion of the exponential profile itself. If such an exponential assumption, however, would be used for pressure measurements above a 1 Hz wave with the probe positioned at 10 cm height, the resulting momentum flux would be underestimated by about 9%. If the same measurement were done at 50 cm height, the underestimate would be about 15%.
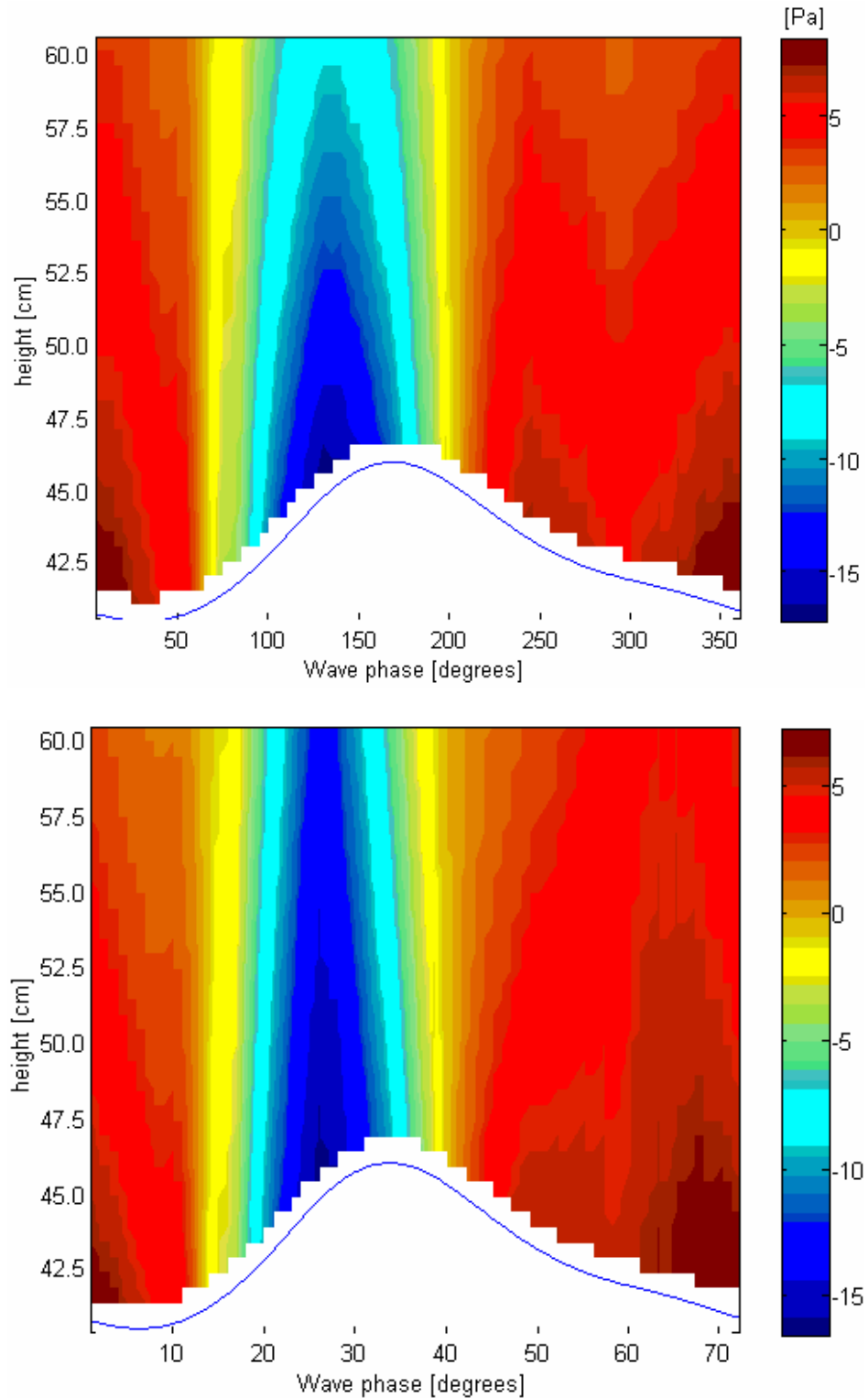
Figure 4.2. Static air pressure map, reconstructed using measured surface elevation and surface pressure with assumption of exponential decay e^{-kz} (top panel), $e^{-\alpha kz}$ (bottom panel), where $U_{10}/C_p = 10.1$, α is defined in eq. 4.7. Both profiles are based on surface pressure corresponding to Fig. 4.1 (top).

Comparison was made with the Direct Numerical Simulations of the wave-induced static air pressure fluctuations (Fig. 4.3) (provided by Jennifer L. Regis, University of Florida). The primary purpose of this comparison was to evaluate the model performance. Although, in general the model was found to require further improvement, especially in the part of surface wave simulations, modeled air pressure fields were found to be qualitatively correct. Furthermore, the pressure map was simulated in two scenarios:
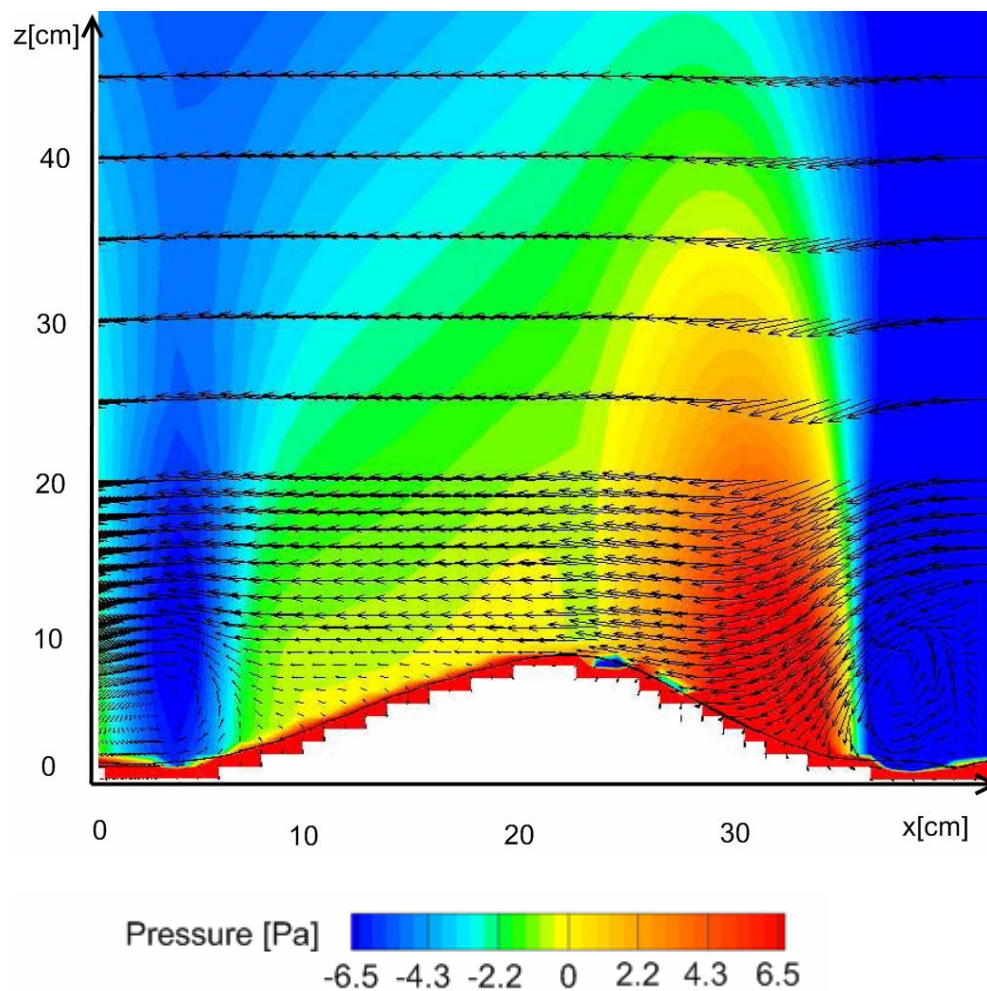
Figure 4.3. Direct Numerical Simulation of the airflow above a surface wave. Model resolution is 1cm near the surface followed by 5cm in the upper region. The wind speed is 10 ms^{-1} at the upper boundary.

with and without the upper rigid lid boundary condition. Such simulations have shown no influence of the upper boundary on the near-surface pressure. In terms of the wave tank experiment this means that pressure fluctuations decay before they reach the tank's ceiling and, therefore, it imposes no limitation on ocean-laboratory similarity.

A more comprehensive study describing similar pressure fields numerically was done by Sullivan et al. (2000). Comparison between the numerical study and the present experimental results can be found in the Results chapter.

Further analysis of the ASIST experiment revealed that for each wave phase in the given height range the observed pressure profile is optimally described by a linear fit. Since measurement heights were within 1/10 of the wave length, this linear profile may approximate a short section of the $e^{-\alpha kz}$ profile. This assumption and measured pressure decay slope give

$$\left. \frac{\partial p_0 e^{-\alpha kz}}{\partial z} \right|_{z=0} \approx \frac{\partial p}{\partial z} \text{, or} \qquad (4.5)$$

$$\alpha \approx -\frac{\partial p / \partial z}{k p_0} , \qquad (4.6)$$

where $\partial p / \partial z$ is the measured pressure slope and p_0 is the linear extrapolation to the surface of the measured pressure profile (~10cm above surface). This procedure provides an α estimate for each wave phase from each experiment. The resulting scatter of α among various experiments allows only the most basic generalization, which is averaging $\alpha(\Theta)$ over all available experiments. This results in the mean phase-dependent exponential pressure vertical decay (Fig. 4.4).
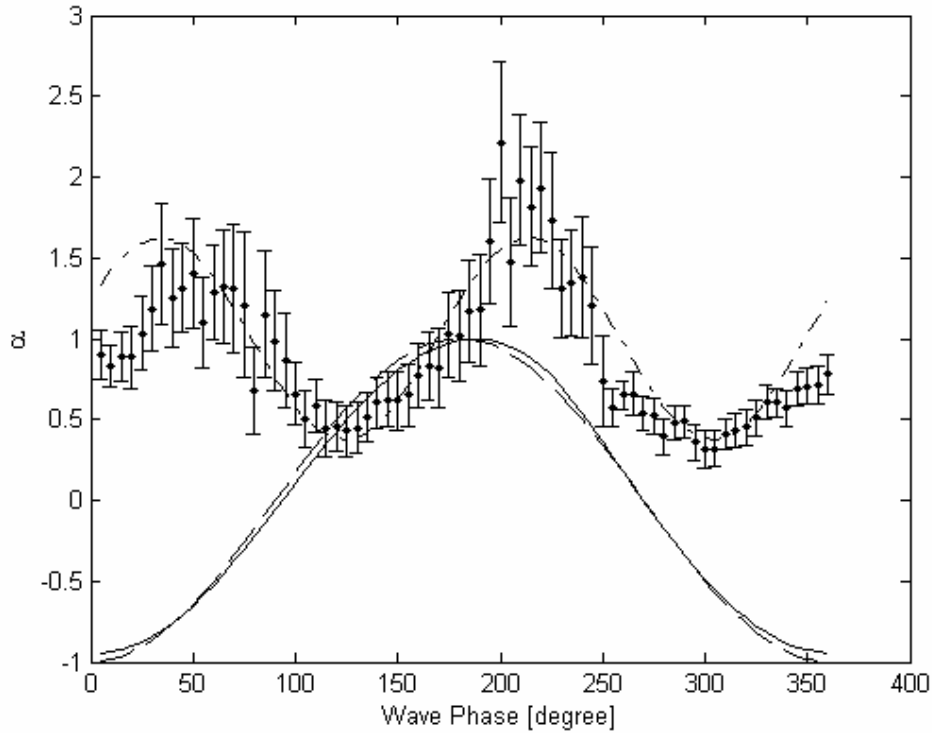
Figure 4.4. The intensity of exponential pressure vertical decay rate (eq. 4.4) as a function of wave phase. Error bars show 95% confidence intervals for the value of α, dash-dotted line represents the closest analytical function fit for α (eq.4.7). Solid and dashed lines are correspondingly measured and fitted mean surface elevation.

The spread of the 95% confidence interval as a function of phase shows that for various wind-wave conditions the exponential decay model is not necessarily consistent in close proximity to the surface. In addition, these results clearly suggest that there is a phase dependence in the intensity of exponential decay. The minimum mean square fit yields

$$\alpha = 1 - \frac{5}{8}\cos(2\Theta + \frac{5\pi}{8}), \qquad (4.7)$$

with corresponding mean surface elevation (shown by the solid line on Fig. 4.4), where the fitted cosine wave ($\eta = -\cos(\Theta)$) is depicted by the dashed line. The averaging was done for each 5° wave phase bin among all runs shown in Table 1. The limitation of such

averaging is that it incorporates experiments with various wind speeds and wave forms, which potentially can influence the $\alpha(\Theta)$ function. An example of pressure profiles incorporating the parameterization (4.7) is shown in Figure 4.2 (bottom panel).

In accord with *a priori* expectations, the observed value of α fluctuates near unity. However, this is the first time its dependence on the wave phase has been observed. In this context, more in-depth experimental research on this topic is needed to confirm this dependence and to investigate the effect of wind forcing severity.

Note, in this work, equation 4.7 was not used for pressure profile extrapolation to the surface. Instead, existing data points were used in each experiment for each 5 degrees wave phase bin to acquire local pressure at the surface. Therefore, the uncertainty in equation 4.7 does not undermine the following results.

b. The reconstruction of current and turbulence profiles using PIV data.

To cover the entire vertical profile from the tank's bottom to the water surface, measurements of velocity vectors were made with PIV windows located at the three depth levels: first, from 42cm to 25cm, second, from 27cm to 10cm, and third, from 12cm to -5cm. Overlap areas served for evaluation purposes, as measurements at various depths were not done at the same time, relying on ASIST's reproducibility. Such an evaluation technique proved to be useful to ensure that there was no significant background flow variability, (i.e., due to long period waves). Before each experiment, a constant wind forcing of ~15 minutes duration was applied to reach "stable" conditions. In some cases, however, profiles still showed slight discontinuity, therefore, overlapping areas were used for smooth reattachment between PIV window areas.

Each PIV image aspect ratio is 4:3 with dimension of 99 columns and 73 rows. This resulted in spatial resolution of 2.3mm. At each depth for each wind-wave case, nine hundred image pairs were taken, and in total this provided 89,100 data points (99 vectors for each pair, with image pairs acquired at sampling frequency of 1 Hz) to estimate turbulent and mean velocity components of the flow for each point of the vertical profile.

Using Reynolds decomposition, measured velocities were separated into mean and fluctuating components:

$$U = u' + <U>$$

$$W = w' + <W>, \quad (4.8)$$

based on which mean horizontal velocity $<U>$ and Reynolds stress $<u'w'>$ profiles were easily reconstructed (averaged over the entire data set). To estimate the mean turbulent kinetic energy all three components of velocity vectors are required:

$$<q^2> = <u'^2 + v'^2 + w'^2>, \quad (4.9)$$

however, the value of the cross tank velocity component is unknown. Instead, the assumption of isotropic turbulence was used:

$$<q^2> = 1.5<u'^2 + w'^2>. \quad (4.10)$$

To arrive at equation 4.10 we assumed that all components of turbulent velocities contain equal amount of kinetic energy.

There is one significant limitation in the estimation procedure of the turbulent kinetic energy based on such PIV data. The values u' and w', estimated in eq. 4.8 are in fact $u'+u^w$ and $w'+w^w$, where u^w and w^w are wave orbital velocities. Due to small wavelengths (2-15cm), orbital velocities decay within few centimeters from the surface (i.e., ~0-15% at 5cm depth), therefore the remainder of the profile is not contaminated by

this limitation. But near the surface, based on the available data, it is practically impossible to separate turbulent and wave components of velocity vectors. Moreover, the assumption made in transition from eq.4.9 to eq.4.10 is only valid for the turbulent components, as wave orbital velocities are not isotropic.

For the reasons described above, the estimates of turbulent kinetic energy in close proximity to the surface can not be trusted. This is one of the reasons why some profiles, shown in the "Results" chapter, do not extend all the way to the surface. As for the Reynolds stress estimate, the presence of the wave orbital velocity should not interfere with it (according to the linear wave theory), as wave motion is considered irrotational and, therefore, does not result in momentum flux $<u^w w^w> = 0$ (averaging was done over more than 1000 wave periods). This assumption has been called into question for steep non-breaking waves by Babanin and Haus (2009) based on experiments in ASIST. However a full analysis of that problem is beyond the scope of the present study.

The turbulent dissipation rate profiles were calculated based on the dissipation range constant slope assumption. Structure functions

$$D_{11}(r) = < (u(x+r) - u(x))^2 > \qquad (4.11)$$

were calculated at each depth. To construct the function $D_{11}(r)$ the range r was varying only horizontally at each depth. A separate function was calculated for each row of each image and later averaged over all 900 images. For each resulting function a region where $D_{11}(r) \sim r^{2/3}$ was chosen, and dissipation rate was calculated as

$$D_{11}(r) = C_2 (\varepsilon \cdot r)^{2/3}, \qquad (4.12)$$

where $C_2 = 2.2$ (Pope 2000). The internal dissipation range, depending on depth was found to start on the scale of millimeters, well clear of the peak associated with longer

scale wave motion. More detailed discussion on dissipation rate estimation methods is

provided in chapter 2.e.

Chapter 5: Results

a. The total air-sea momentum flux

The results of the total air-sea momentum flux measurements, described in section 3.d, are shown in Fig. 5.1. The data collected in this experiment partly overlapped with the wind-wave flux experiment in terms of wind-wave conditions. Therefore, the wind-wave conditions of these data points represent a reproduced subset of experiments conducted within the wind-wave momentum flux experiment (specifically experiments # 1,2,3,4,7,11,12,13,14,16,17,18,19,20,39,42,51,52,53 shown in Table 1).
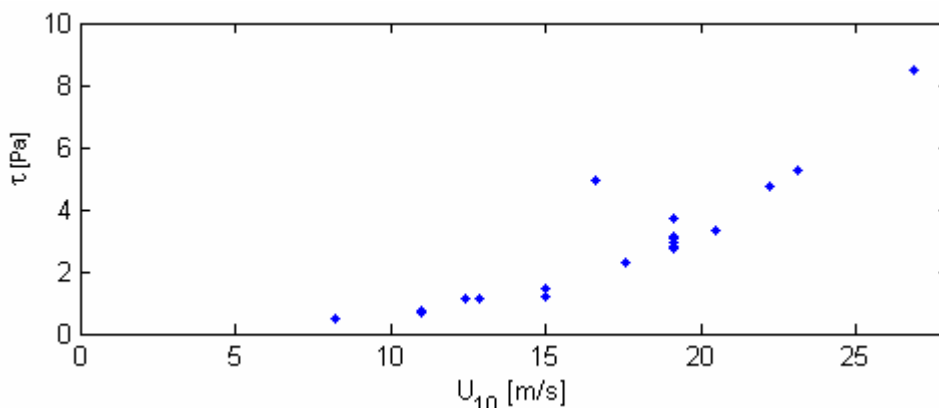
Figure 5.1.The total air-sea momentum flux as a function of wind speed.

The entire curve (Fig. 5.1), is about 3 times as high as that was observed by Large and Pond (1981). This might partly be explained by the significantly higher wave steepnesses in the laboratory compared to the ocean. Such large disagreement requires more validation in future, particularly several experiments must be conducted with no mechanical waves and compared to Donelan et al. (2004). His data was collected in the same laboratory, for the same wind speeds but without additional mechanically generated long waves and showed good agreement with Large and Pond (1981). Also, other

experimental methods of total stress measurements must be used to confirm present data. Therefore, in this work the momentum flux shown in Fig. 5.1 will be considered as preliminary data. It is suggested that steep mechanically generated waves are the primary reason for these high values of momentum flux. In the ocean the presence of swell is known to sometimes boost the drag coefficient in a similar way (e.g. Drennan et al.1999, figure 10).

In the following sections further investigation of the effect of the momentum flux is conducted, first, in the water column (Chapter 5.b). Then, a thorough study on wind-wave momentum transfer is provided, looking particularly at the role of an individual wave frequency (Chapter 5.c), based on which wave-growth parameterization is formulated (Chapter 5.d). Shortcomings and non-linearities associated with spectral wave growth formulation are discussed in Chapter 5.e.

b. Currents and turbulence response to the wind stress.

PIV based measurements of current velocity vectors were made at five wind speeds: 2.5, 5.0, 7.5, 10.0 and 12.5 ms^{-1} at 30 cm above the mean water surface reference level, which corresponds to $U_{10} \sim$ 3.8, 7.5, 11.0, 15.0, and 19.1 ms^{-1}. The air-sea viscous stress generated a near-surface current. Due to mass conservation and the finite length of the tank this generated a backflow along the bottom of the tank in the direction opposite to the wind. To cancel out the backflow, a background current of 0.075 ms^{-1} was generated in along-wind direction.

The resulting mean horizontal current profiles are shown in the top panel of Fig.5.2. PIV measurements were done at three depth levels and the gray boxes on the

figure show the overlap areas between the datasets. At the junction areas, the profiles were forced to connect using a linear weighted window. A tangential wind stress forces the surface current to accelerate as the wind speed increases, causing the current profile to deviate from the original background current value. All profiles converge to zero as they approach the bottom at -420 mm. At some overlap levels, the profiles show a sharp change (i.e. green line at -260 mm) due to long term variations that occurred between experiments. Note that on the bottom panel of Fig. 5.2, the vertical profiles of mean horizontal velocity are shown in non-dimensional coordinates. It is given for the purpose of comparison to similar profiles on a different length scale, if needed.

Using mean current profiles results, fluctuation velocities can be obtained as: $u' = U - <U>$, $w' = w - <W>$. For the most of the profile length these quantities represent turbulent velocities. However, near the free surface they also carry wave orbital velocities information. The resulting profiles of the quantity $<q^2>$, calculated based on eq.4.10, are shown on Fig 5.3. The solid lines show profiles corrected for wave orbital velocities, calculated under the linear wave assumption. Higher winds enhance vertical momentum flux and force deeper layers through turbulent motions. Both wave orbital and turbulent velocities decay with depth as expected.

Experiments with wind speeds $U_{0.3} = 7.5$ ms^{-1} and below produced relatively smooth waves. The run with $U_{0.3} = 12.5$ ms^{-1} demonstrated significant wave breaking and the run with $U_{0.3} = 10$ ms^{-1} is a transitional case between smooth and breaking waves conditions. For the $U_{0.3} = 2.5$ ms^{-1} run, wave motion was practically undetectable.
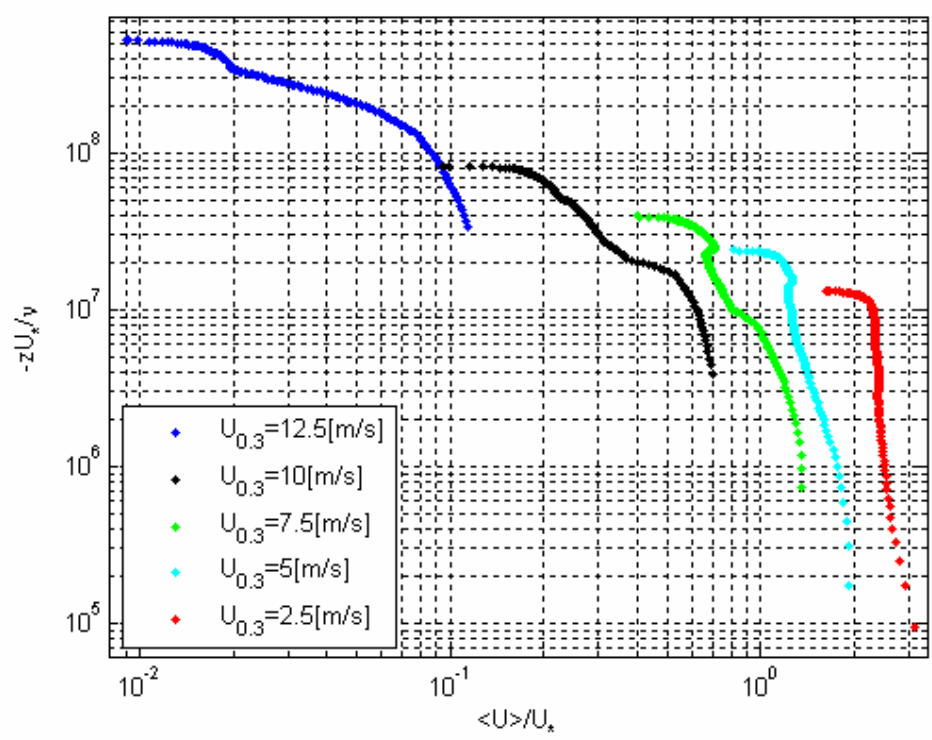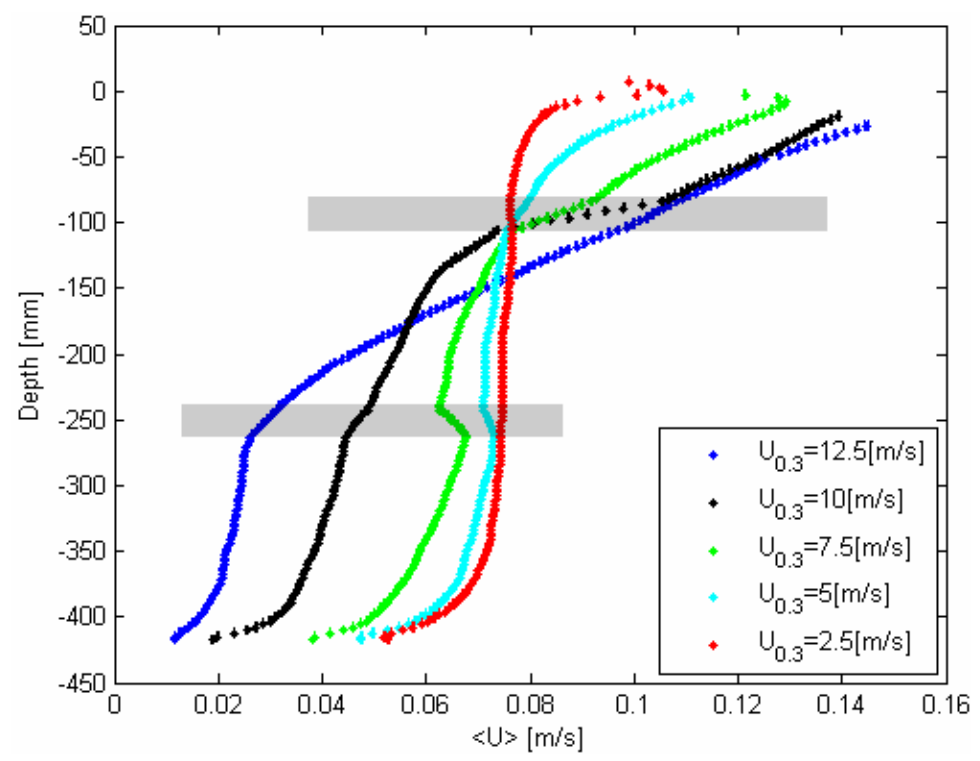
Figure 5.2. Top: mean horizontal velocity profiles. Bottom: same profiles in non-dimensional coordinates. Gray boxes correspond to regions of profile junctions. Velocity profiles are shifted by ~7.5[cm/s] due to the superimposed current.
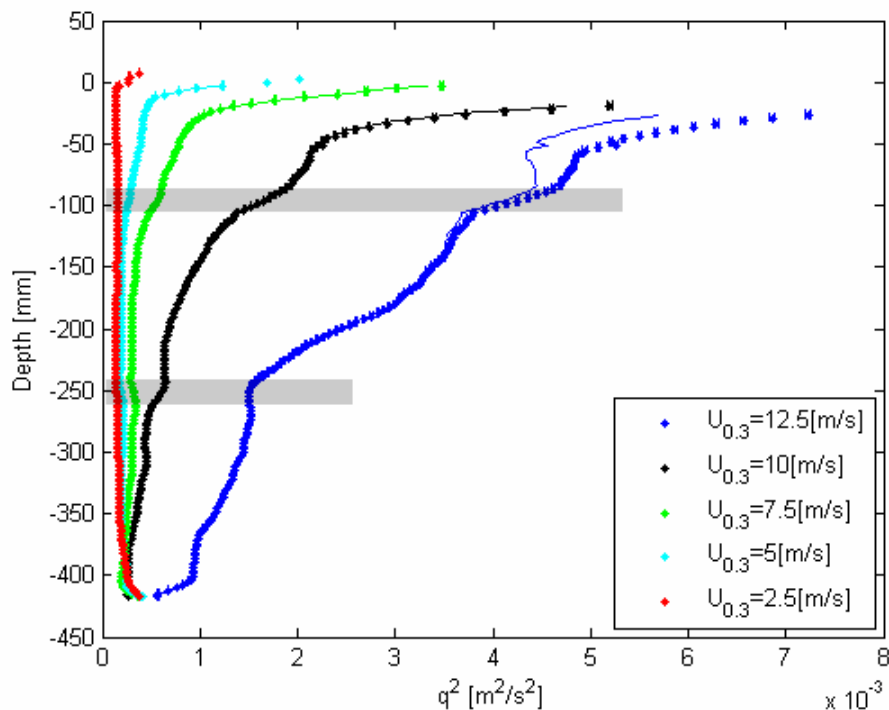
Figure 5.3. Turbulent kinetic energy profiles with their 95% confidence intervals. Dots represent direct estimate based on measured velocities. Solid lines are the same data corrected for wave orbital velocities. Gray boxes correspond to regions of profile junctions.

Note, how the short waves of (2-10Hz) and strong wind forcing can engage the entire vertical profile in turbulent motion at depths greater than a wavelength. Two examples of wave spectra before and after (5.77m and 8.67m) the PIV measurements fetch (6.6m) are shown on Fig.5.4.
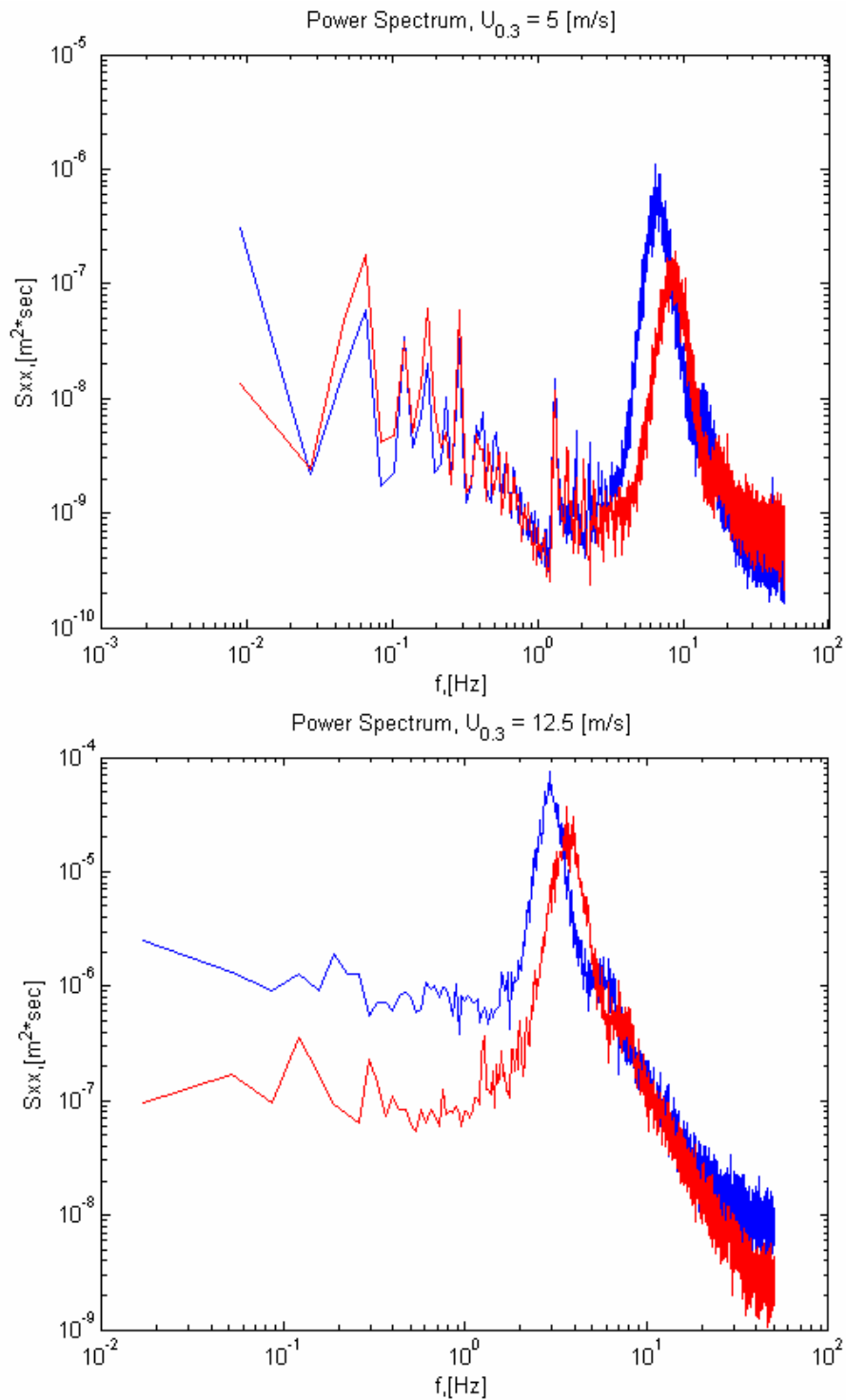
Figure 5.4. Two examples of the wind wave power spectrum before (5.77m fetch, red line) and after (8.67m fetch, blue line) the PIV window location (6.6m fetch). Top $U_{0.3} = 5$ ms^{-1}, bottom $U_{0.3} = 12.5$ ms^{-1}.

Since linear wave motion does not carry turbulent stress, $\langle u^w w^w \rangle = 0$, apart from non-linear wave effects, the quantity $\langle u'w' \rangle$ represents Reynolds stress throughout the profiles (Fig.5.5). The reduction of the stress at depths <50mm can be attributed to wave-current momentum transport (Cheung and Street 1988a). More specifically, the stress peak can be caused by additional momentum influx from the waves. Such effect is poorly understood and is not accounted for in coupled wind-wave-current models.
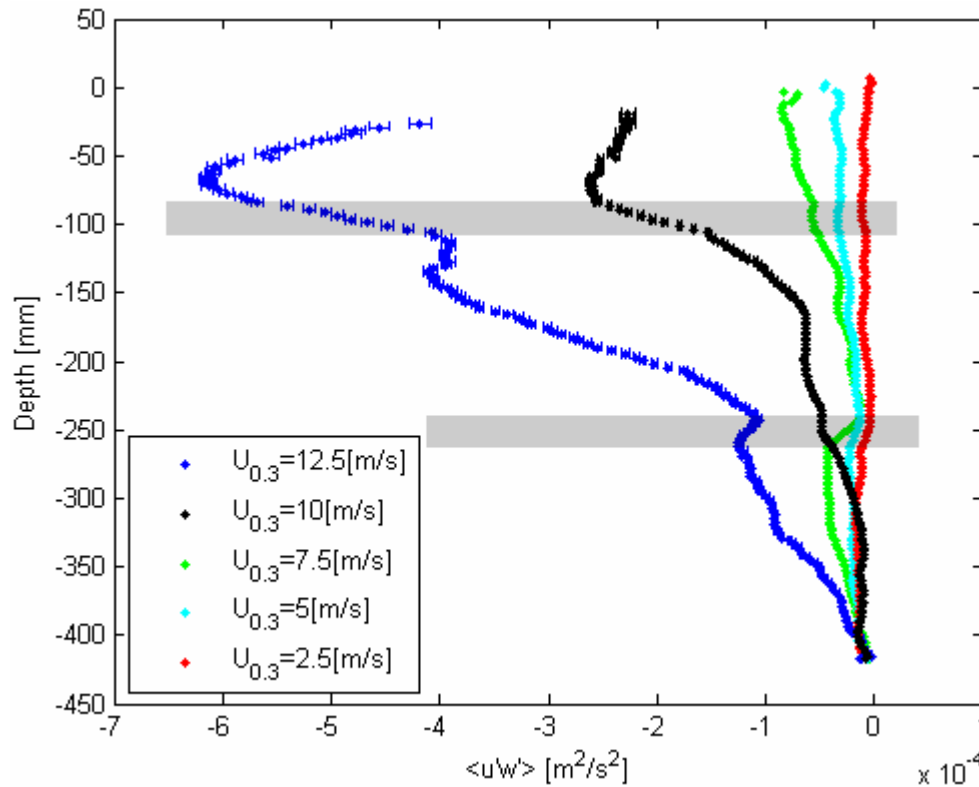
Figure 5.5. Reynolds stress profiles with 95% confidence intervals. Gray boxes correspond to regions of profile junctions.

To calculate turbulent dissipation rate profiles, equations 4.11 and 4.12 were used. For more detail on dissipation rate calculation methods see sections 2.f and 4.b. The resulting profiles $\varepsilon(z)$ are shown in Figure 5.6. The definition based profiles with 2D and 3D isotropy (eq.2.18, 2.19) closely match each other, suggesting the validity of the isotropy assumption at each depth level. But both of these estimates are much lower than

the values obtained through Kolmogorov's structure functions (eq. 4.12). This is because much of the dissipation happens on a scale within 1 mm, which is not captured by direct measurements, but is accounted for within the Kolmogorov's dissipation range theory. Solid lines in Fig. 5.6 represent typical values of dissipation in the ocean for the given friction velocity. In most cases the dissipation in the laboratory was found to be much bigger, because of the bottom effect typically not present in the field. Due to the back flow along the bottom the horizontal shear in the flow is much greater, which intensifies turbulence production and thus turbulent dissipation. For two cases with the strongest
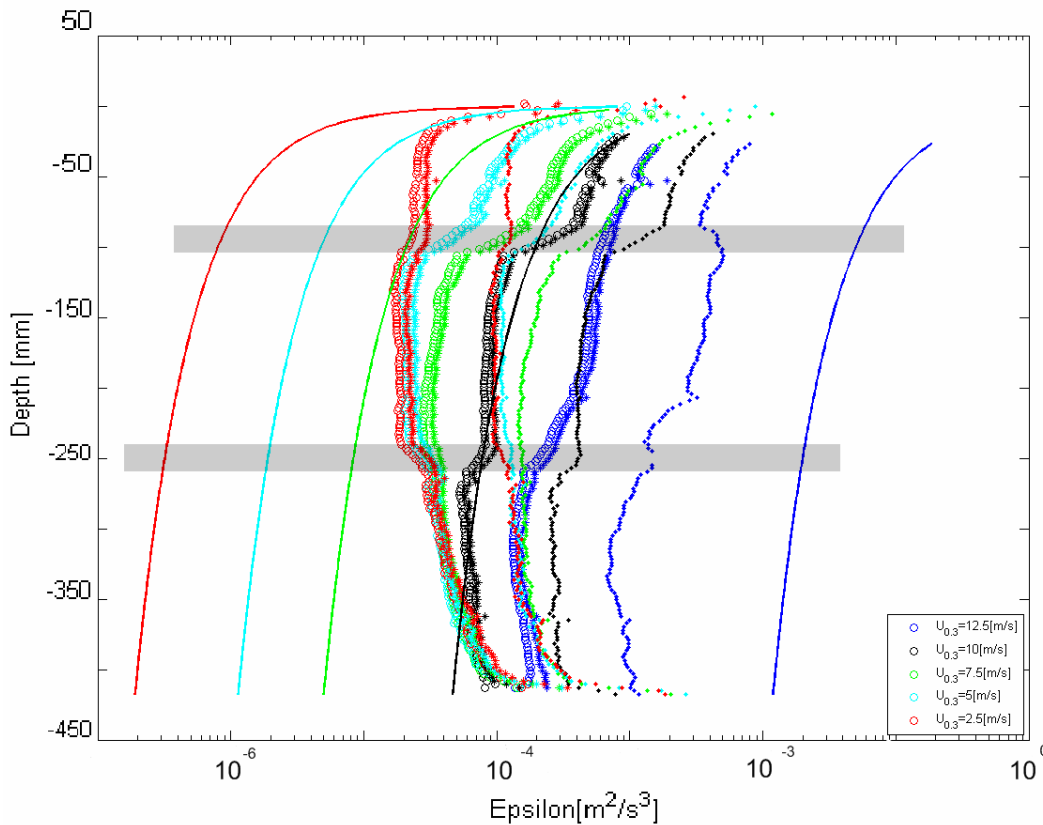
Figure 5.6. Turbulent dissipation rate profiles. Dots represent the method based on structure functions (eq.4.12), circles and asterisks are values calculated by definition assuming of 2D and 3D isotropy respectively (eq.2.19,2.18), solid lines are obtained through the similarity theory $\varepsilon z \kappa / u_*^3 = 1$ *(Lumley and Panofsky 1964). Gray boxes correspond to regions of profile junctions.*

wind speed, on the contrary, similarity theory over predicts the value of the dissipation. This is most likely due to enhanced wave-current momentum flux which causes higher than expected values of friction velocity used to calculate the dissipation rate $\varepsilon \kappa / u_*^3 = 1$.

In smooth surface cases (Fig. 5.6), the most intensive dissipation occurs close to the upper and lower boundaries. As the wind speed increases, near-surface dissipation starts to dominate the flow, and in the most severe case with the wave breaking present, the entire upper half of the profile is involved in intense turbulent dissipation.

For experimental data evaluation purposes, a balance between turbulence production and dissipation can be determined from these high resolution data. The production is given by (Mellor and Yamada 1982)

$$-\overline{u'w'}\frac{\partial U}{\partial z} = \frac{q^3}{\Lambda_1}, \qquad (5.1)$$

where $\Lambda_1 = 16.6\ell$ is their dissipation length scale. Eddy viscosity approximation gives

$$-\overline{u'w'} = S_M q l \frac{\partial U}{\partial z}, \qquad (5.2)$$

where $S_M q \ell$ is the eddy viscosity and $S_M = 0.39$ for neutral stratification. Combining equations 5.1 and 5.2 results in

$$q^2 = (\frac{\Lambda_1}{S_M \ell})^{1/2}\left|\overline{u'w'}\right| = 6.5 \left|\overline{u'w'}\right|. \qquad (5.3)$$
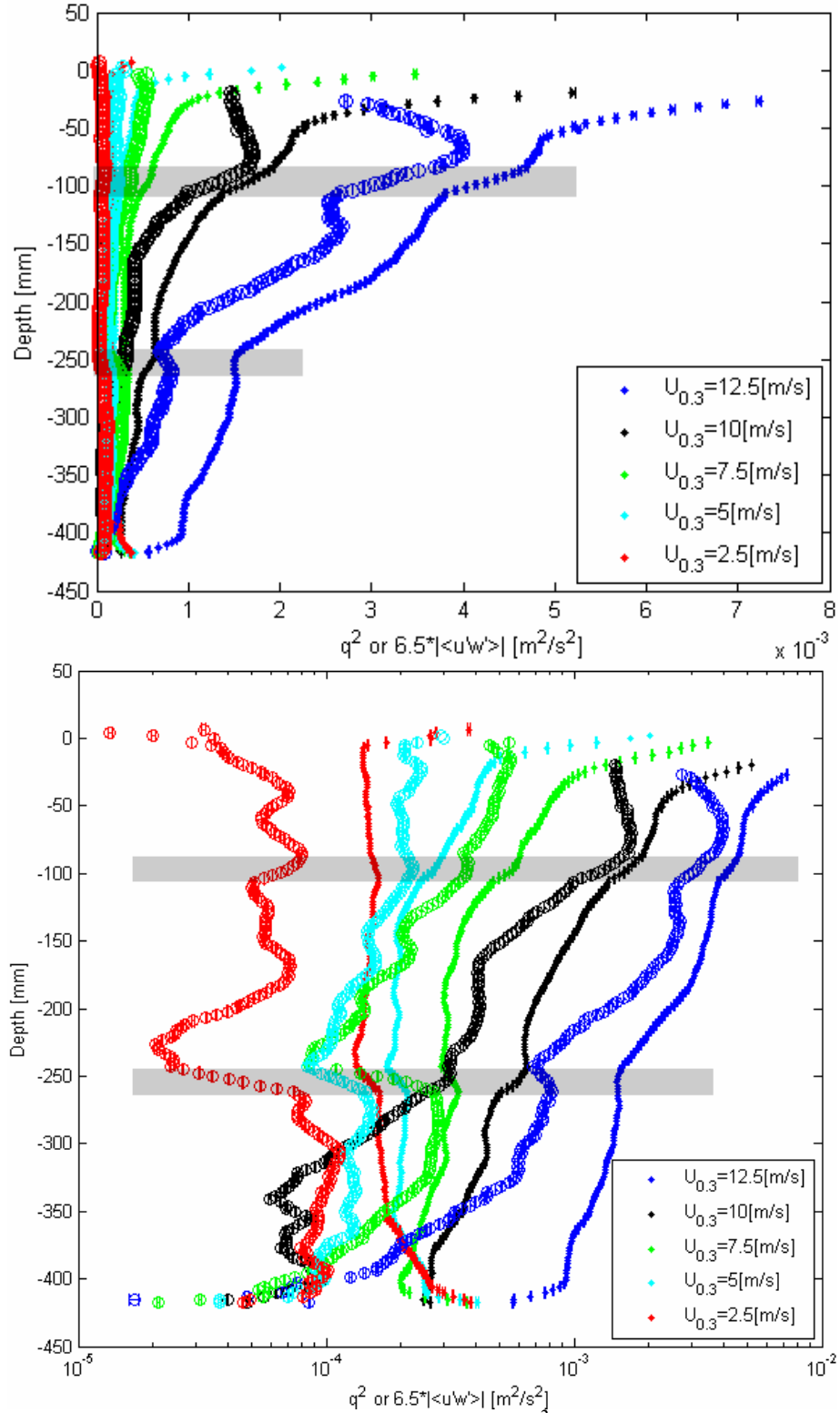
Figure 5.7. Comparison of turbulent kinetic energy q² (dots) and Reynolds stress 6.5|<u'w'>| (circles) vertical profiles. Top panel shows linear scale, bottom logarithmic. Gray boxes correspond to regions of profile junctions.

Note that figure 5.7 compares leftmost (dots) and rightmost (circles) sides of equation 5.3 using experimental data. Within the turbulence closure scheme (Mellor and Yamada 1982) these two curves are expected to match. We see that experimental curves follow each other with some offset throughout the lower depth range. They diverge near the surface as the kinetic energy estimates start to be contaminated with wave orbital velocities and as the turbulent momentum flux gives way to viscous flux.

c. Wind-wave momentum flux.

Once the phase resolved static air pressure at the surface and surface slope are obtained (see chapter 4.a for details), momentum flux is given by (eq.2.10). It was calculated for each run (Table 1) and is shown on Fig. 5.8.
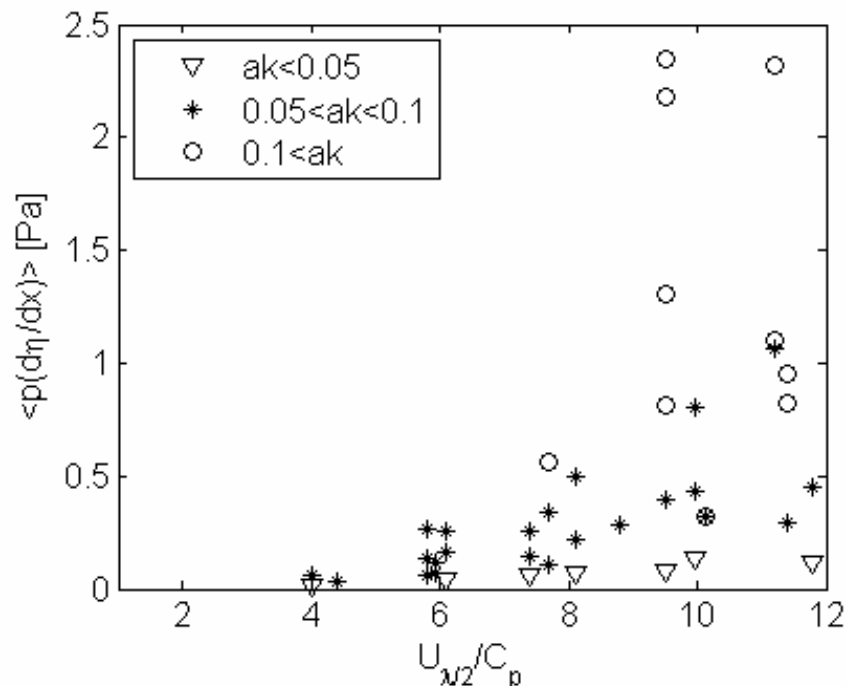
Figure 5.8. Wind-wave momentum transfer as a function of wind forcing, where $U_{\lambda/2}$ - wind speed at half the wave length height, C_p - wave phase speed, ak - wave steepness. Several points with significantly higher momentum flux are due to mechanically generated wave with steepness (ak = 0.15, 0.16, 0.19) far exceeding typical values for such wind forcing in the ocean.

The momentum transfer intensifies with the wind forcing as anticipated. In addition, the steepness of the imposed mechanical wave is reflected in the pressure-slope correlation (momentum input), due to enhanced surface roughness. Some of the values of the momentum flux are dramatically exceeding what was observed in the ocean in high winds. The following analysis will show that this happens due to unnaturally high wave steepness created in the laboratory.
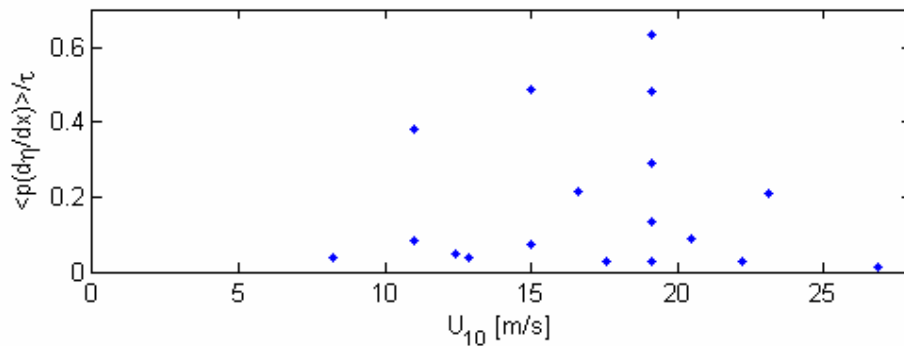
Figure 5.9. Ratio of momentum flux from wind into mechanically generated wave to total momentum flux as a function of wind speed.

After combining total momentum flux and wind-wave momentum flux, the contribution of the momentum flux into a mechanically generated wave to the total wind stress is shown in Fig. 5.9. A remarkable feature is exposed by 5 data points at $U_{10} = 19.1$ ms^{-1}. These points have constant wind speed and mechanical wave frequency, but differing mechanical wave steepness. These waves can be responsible for a wide range of contribution to the total wind stress, however, Figure 5.1 shows all 5 points nearly collapsing near one value. This means that as long the mechanical wave steepness, and
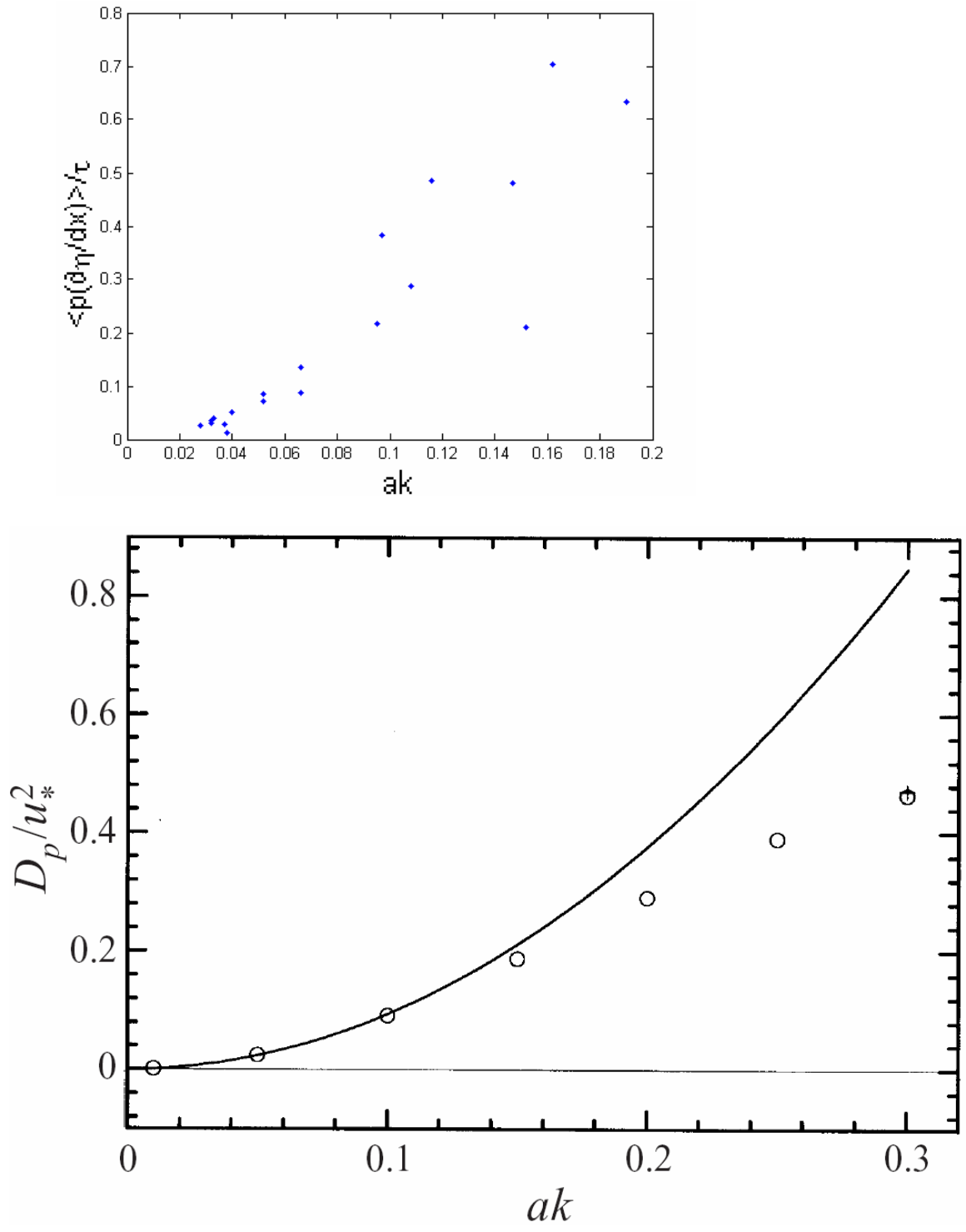
Figure 5.10. Top: The ratio of the momentum flux into a wave to the total momentum flux as a function of wave's steepness, bottom: similar ratio of the form drag D_p to total drag (i.e. friction velocity squared), taken from Sullivan et al. (2000). Solid line is asymptotic theory prediction, circles are the results of the numerical model simulation.

the amount of momentum transferred into the wave increase, the long wave dampens the wind-wave field in such a manner that its share of stress is symmetrically reduced.

The ratio shown on Fig.5.9 varies between 0.02 and 0.71. Since there is no clear dependence on wind speed it is important to investigate what the ratio $< p \frac{\partial \eta}{\partial x} > / \tau$ depend on. On Figure 5.10 its dependence on the mechanical wave steepness is given. It suggests that the role of a monochromatic wave the total air-sea momentum flux is a function of its steepness.

Such dependence was also shown by Sullivan et al. (2000) based on direct numerical simulation of wind over solid waves (Fig. 5.10 bottom). While there is qualitative agreement, the present results predict a faster growth of such function with wave steepness. This is most likely caused by the much smaller wind velocity and wind forcing used in numerical simulations. The viscous drag played a larger role in the total momentum flux, therefore a smaller portion of the total drag was represented by the form drag.

If aided by the total wind stress and wave steepness, the results shown on the top panel of figure 5.10 can help understand the separation between form and viscous drag in high wind conditions. The ratio, however, is given for one isolated wave frequency and can only be applied in an idealized scenario or have to be integrated through a realistic wave spectra. Note that in typical hurricane conditions the steepness of a wind-driven wave $H_s k/2$ usually does not exceed 0.03 (e.g. Wright et al. 2001), therefore according to present results the form drag due to such a wave can be responsible only for a few percent of the total drag. Note, that this value does not represent the entire form drag, but only one part of it that corresponds to a wave of a particular frequency.

d. Wave Growth Parameterization

The non-dimensional wave growth function (eq.2.9) is the ratio of kinetic energy influx to the total energy of the wave times the ratio of water density to air density. In other words, it is a relative kinetic energy growth rate. It may be calculated as

$$\gamma(\omega) = \frac{<p(\omega)\eta(\omega)^* >}{\rho_a g E(\omega)} \quad , \quad (5.4)$$

where $<p(\omega)\eta(\omega)^*>$ is the quadrature spectrum (Snyder et al. 1981). However, it is impossible to obtain the entire function based on one 30min experiment due to the rapidly increasing error in the tail of the wave spectrum. Therefore, each experiment was used to calculate only one value, corresponding to the frequency of the mechanically generated
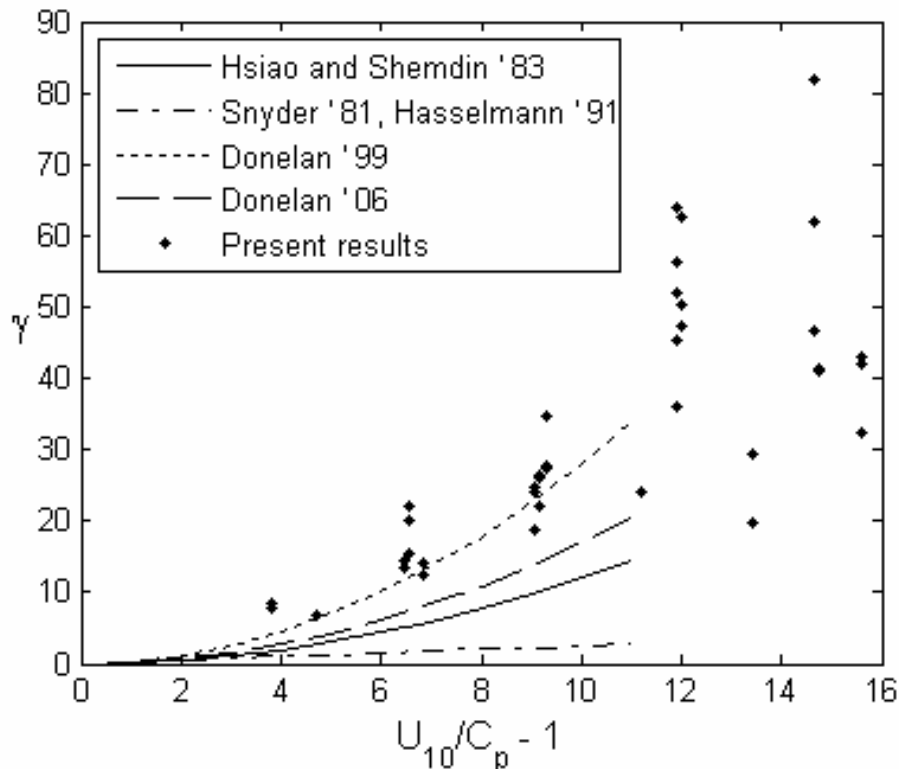
Figure 5.11 .Spectral wave growth function dependence on wind forcing. Present study data points are compared to parameterizations obtained by other authors.

wave. This simplifies equation 5.4 further

$$\gamma\big|_{\omega=const} = \frac{C_p < p\dfrac{\partial \eta}{\partial x} >}{\rho_a g \omega \sigma^2} , \qquad (5.5)$$

where σ^2 - variance of the surface elevation of the mechanically generated and wind amplified wave. All variables on the right hand side of equation (5.5) are known and the resulting wave growth function can be easily calculated. It is shown together with parameterizations obtained by other authors on Fig. 5.11.

As described in the background chapter, one of the goals of this work was to investigate the nature of the γ dependence on various wind-wave conditions. According to the linear wave theory it should be a function of the wind forcing only. However, results of this study are widely scattered similar to the previously observed scatter of the function. Note that previous parameterizations were based on data collected in moderate wind conditions, mostly in the range of $1 < U_{10}/C_p < 4$ and never exceeding $U_{10}/C_p = 7.6$. Results of the present work extend the range of the wind forcing to over $U_{10}/C_p = 16$. In such extreme conditions, the non-linear nature of the process is expected to reach its full potential. Therefore, wave steepness ak, was investigated as another controlling parameter, responsible for the scatter.

Clusters of points with nearly constant U_{10}/C_p, but strongly scattered γ can be seen on Fig. 5.11. These clusters were created on purpose to provide cross-sections $\gamma(ak)\big|_{U_{10}/C_p=const}$ and thus map the entire function $\gamma(U_{10}/C_p, ak)$. Note that the following results are presented in reference to $U_{\lambda/2}$ rather than U_{10}, as wind speed measurement at half the wave length height is more relevant to the problem discussed. Table 1 can be used to convert to U_{10}.

First, the dependence of wave growth on wind forcing only is calculated. A quadratic fit $\gamma(U_{\lambda/2}/C_p) = 0.52(U_{\lambda/2}/C_p - 1)^2$ forced through the (0,0) point is shown in Fig 5.12 (solid line). The next step is to incorporate a wave shape parameter in an attempt to reduce the remaining scatter. The dependence of the wave growth function γ on wave steepness is shown with differing symbols in Fig. 5.12. While the result is mixed, it can be suggested that experiments with higher wave steepness tend to produce lower γ. In some cases, an increase in steepness is responsible for up to 50% decline in γ, however in other cases increases with steepness. According to Jeffreys "sheltering hypothesis" a decrease of γ with increasing steepness is expected. As steepness increases, at some point the airflow cannot follow the wave surface and separates. This causes the relative wave growth to decrease below the expected value. The goal of the following discussion is to provide a clear, quantitative description of this effect based on available data.

Second, the dependence of wave growth on wave steepness is calculated. To investigate the effect of wave steepness, each cluster of runs of nearly constant wind forcing is analyzed separately. All of them are shown as $\gamma(ak)\big|_{U_{\lambda/2}/C_p=const}$ with corresponding linear fit on Fig. 5.13.
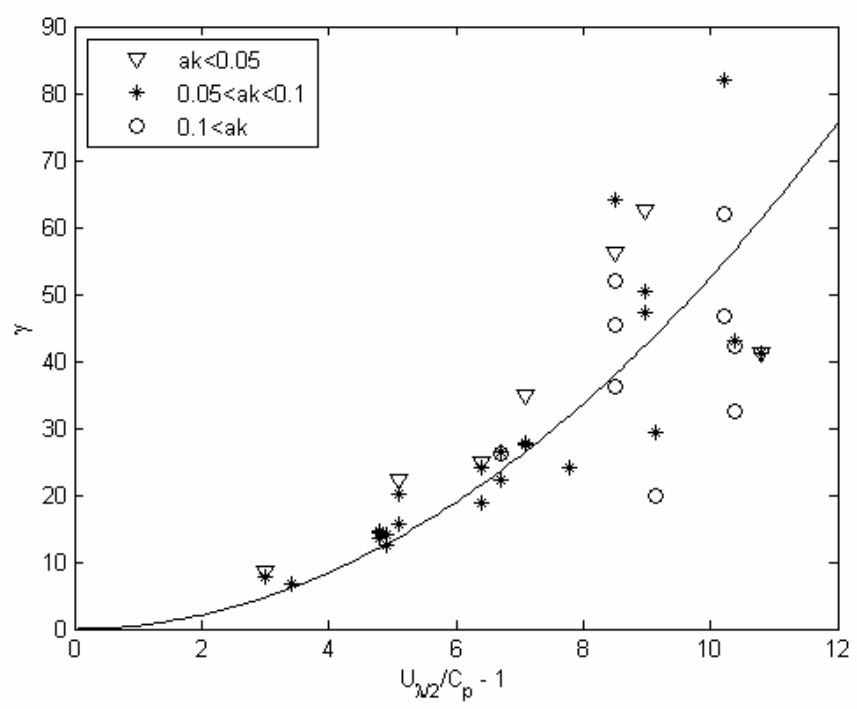
Figure 5.12. Spectral wave growth function dependence on wind forcing. Asterisks, circles and triangles represent different steepness bands of the studied wave.
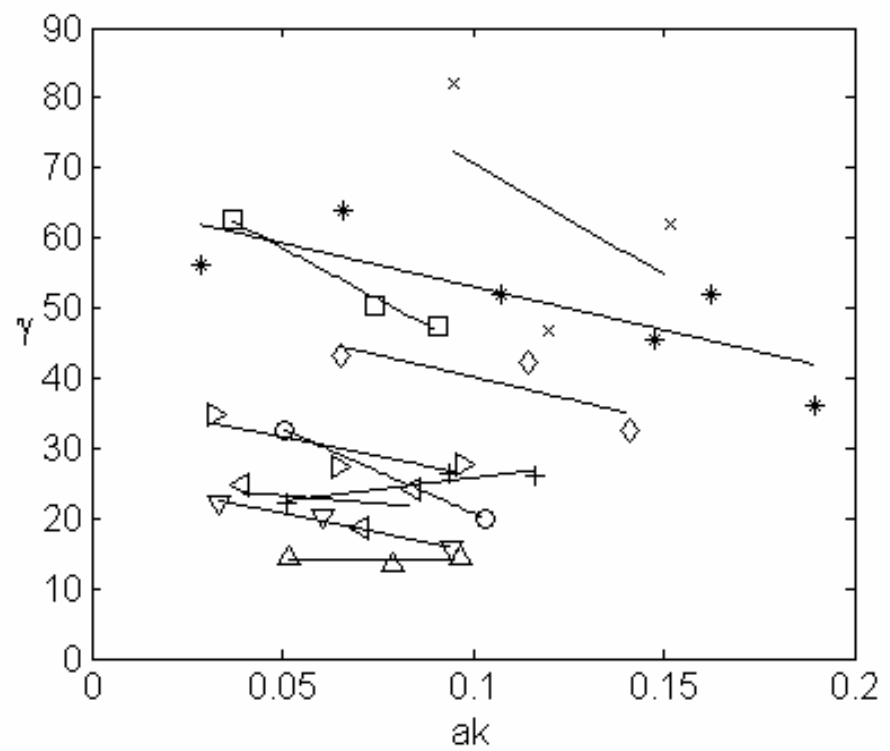
Figure 5.13. Spectral wave growth function dependence on wave steepness for various wind forcing. Symbols represent groups of runs with constant wind forcing. Solid lines represent a linear fit through each group.

It is evident that a decline of γ with steepness occurs in almost all cases. Moreover, the slope seems to be increasing as the value of γ increases. This leads to an assumption $\frac{\partial\gamma/\partial ak}{\gamma} \approx const$. Therefore, the data were generalized as having a linear decline of γ with increasing *ak*, which is supported by recent findings of Pierson and Garcia (2008). To quantify this dependence, each *γ(ak)* function in Fig.5.13 was normalized by its average <γ>, so that the linear fit through all available data gives an average *γ(ak)* linear fit (Fig.5.14). The resulting averaged dependence of the wave growth function on wave steepness is given by

$$\gamma \propto -1.9ak + 1.2, \qquad (5.6)$$

where the 95% confidence interval of the linear regression slope is -1.9±0.58. The decline rate of normalized wave growth function can be compared to sheltering coefficient by Pierson and Garcia (2008, figure 7). Most of the decline that they observed took place at *ak* < 0.05, this range of steepness is poorly covered by the present data. But if their data set is compared to the present data in 0.05 < *ak* < 0.15 range, the declines are ~20% and ~35% respectively, which is not a perfect match but is within the range of confidence intervals. This difference might be attributed to a much stronger wind forcing in the present study, as the effect of wind forcing on sheltering coefficient relation to wave steepness remains unknown.
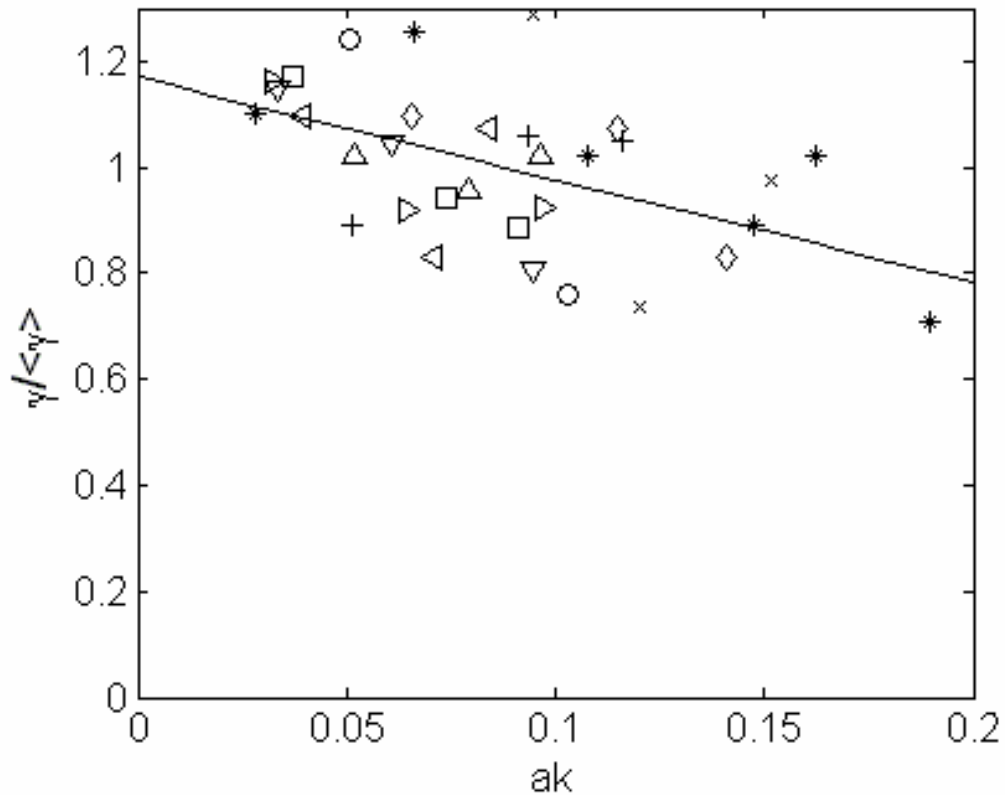
Figure 5.14. Normalized and averaged dependence of the spectral wave growth function on wave steepness. Symbols are the same as in fig. 5.13. Solid line represents averaged linear fit.

As can be easily seen in Figure 5.14, equation 5.6 is unable to fully account for all wave growth spectra variations at a given wind forcing. The variance of the data itself (i.e., γ is independent of ak) is 0.022. The given linear fit reduces the variance to 0.016, with a linear correlation coefficient of 0.52.

In an attempt to further reduce the scatter, another possible controlling parameter was investigated. Separation takes place on the lee side of the wave crest, therefore, crest sharpness might be a better parameter to quantify this effect. To check this idea, crest sharpness was calculated as ratio of wave crest height from mean water level to crest width at half the height. The rest of the derivations were similar to ak and produced

averaged and normalized wave growth function dependence on crest sharpness (Fig.5.15).

Such dependence, however, results in an even weaker correlation of 0.31, and, therefore,

crest sharpness was not chosen as a controlling parameter.
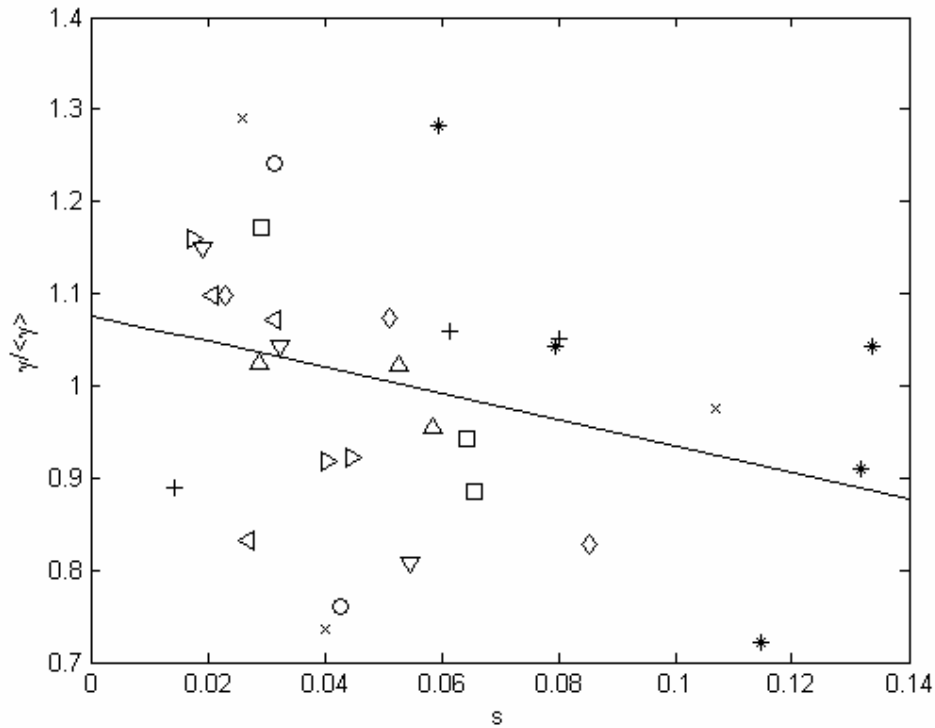
Figure 5.15. Normalized and averaged dependence of spectral wave growth function on wave crest sharpness. Symbols are the same as in fig. 5.13. Solid line represents averaged linear fit.

Finally, based on considerations above, wave growth dependences are combined

and it was concluded that the empirical function describing wave growth primarily

depends on wind forcing with sheltering coefficient correction parameterized through

wave steepness:

$$\gamma(\frac{U_{\lambda/2}}{C_p}, ak) = 0.52G \cdot (\frac{U_{\lambda/2}}{C_p} - 1)^2, \qquad (5.7)$$

where *G=(-1.9ak+1.2)*. Three cases with differing wave steepness are shown on Figure

5.16 for illustration. Limiting values of wave steepness *ak* = 0.01 and 0.2 are shown in

the figure. Ideally all data points are supposed to be within these two boundaries. Wave

steepness *ak* = 0.1 corresponds to the average wave steepness.
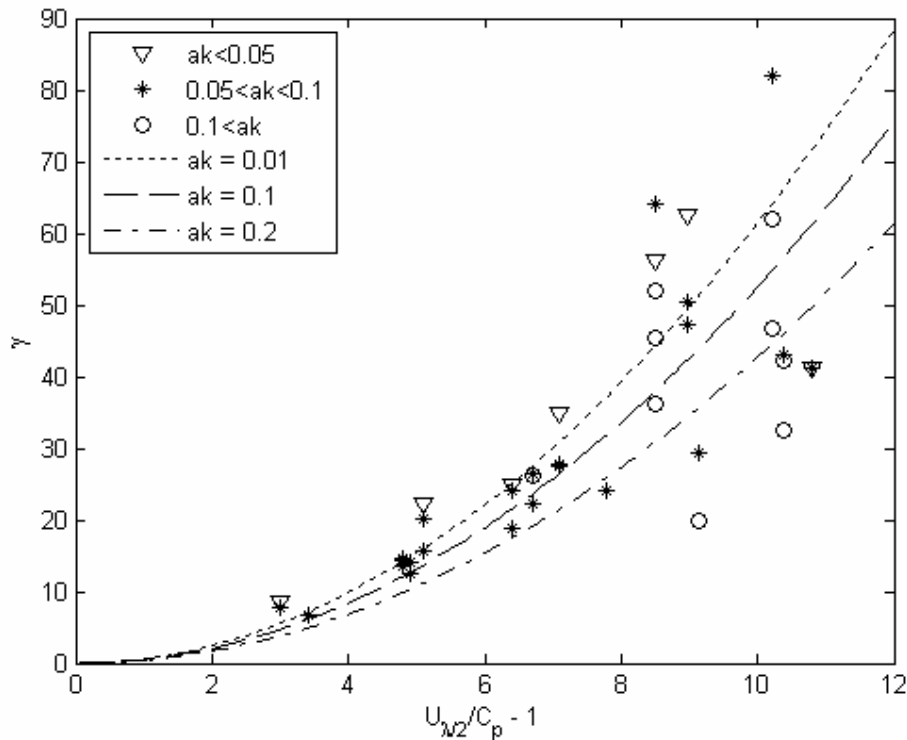
Figure 5.16. Three examples of the final spectral wave growth function parameterization (eq.5.7) compared to available data points.

  e. The effect of wave's non-linearity on the wave growth.

  The given overall spectral wave growth function parameterization (5.7) yields a

correlation coefficient of 0.78 with available data points. While it is a reasonable

correlation, further steps were made to explain the remaining scatter.

  Both wave steepness and wave crest sharpness are properties of the wave shape.

The wave shape together with the wind forcing were thoroughly investigated above,

however, scatter still remains in those data. There must be some other physical properties that are influencing the wave growth. Such influence on the growth of a particular wave frequency can be caused by other waves within the wave spectrum. For example, longer waves are known to shelter shorter waves (Kukulka et al. 2007) and, therefore, reduce the momentum flux. Another more complicated mechanism involves wave-wave energy flux within wave spectra. Below, a case of interaction between harmonics of a longer wave and wind wave peak is discussed.
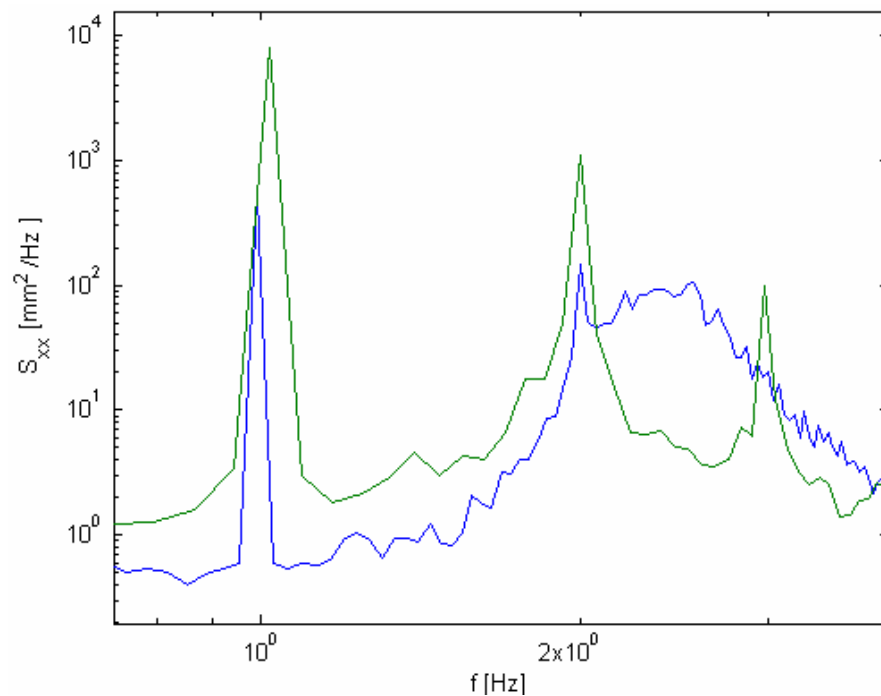
Figure 5.17. Wave spectra below the wave follower for Experiment #51 with ak=0.162 (green line) and Experiment #53 with ak=0.028. In both cases wind speed U_{10} = 19.1ms^{-1}, mechanical wave frequency 1Hz.

Examination of experiments with identical wind speed and identical mechanically generated wave frequency reveals the most apparent difference between input parameters of these experiments was the amplitude of the mechanically generated waves. In Figure 5.17, a case with the smallest (blue line) and largest (green line) mechanical wave

steepness (ak = 0.028 and 0.162) are shown. Even with low steepness, the sharp peak at 1

Hz is clearly visible, as well as its first harmonics at 2 Hz. A wider peak at 2.5 Hz

corresponds to the wind-generated waves.

If there were no interactions between wind waves and mechanical waves, the wind

peak would be expected to remain unchanged as the steepness of the mechanical wave

increases. However, at higher steepness an enhanced energy transfer from the wind wave

peak to the first harmonic is observed in the data. The value of the wave spectrum at

2.5Hz has decreased by an order of magnitude, and the width of the primary wave and its

first harmonic (2Hz) has increased, indicating wind wave energy buildup around it. The

gradual evolution of the wind-wave spectral peak can be seen in Fig.5.18.
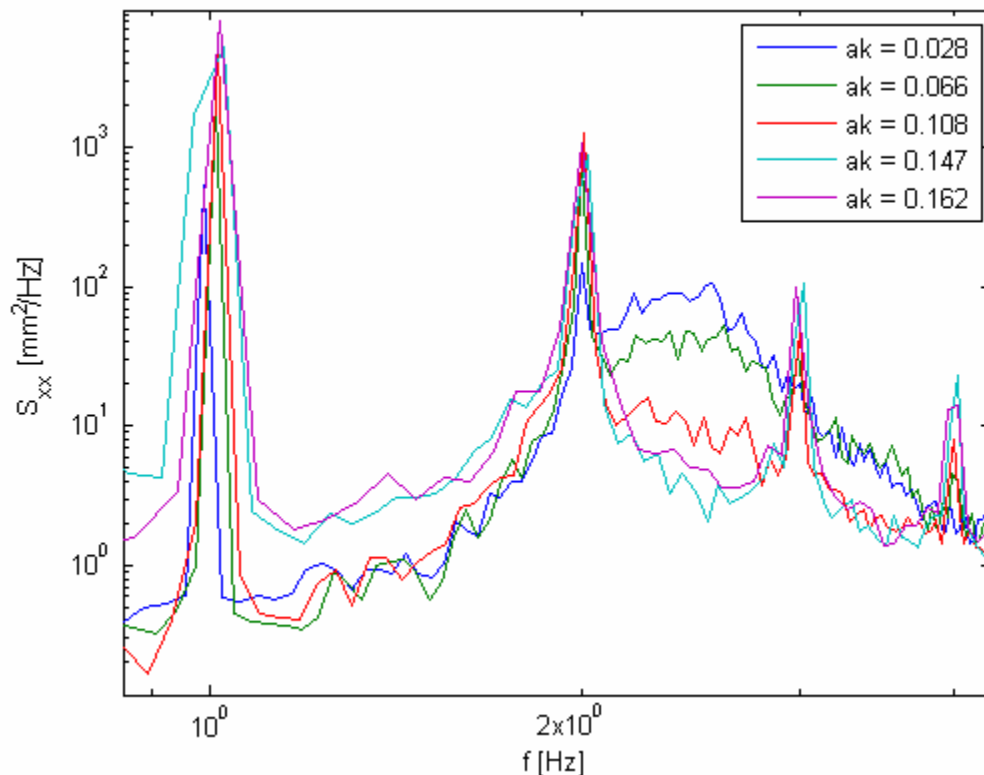
Figure 5.18. Wave spectrum below the wave follower for Experiment #3,7,13,51 and 53.
In all cases wind speed U_{10} = 19.1 ms^{-1}, mechanical wave frequency 1Hz The only
changing parameter is the steepness of the generated wave, shown in the legend.

Based on the wave spectrum alone, it is impossible to assess whether the wind peak disappears due to reduced non-dimensional wave growth function γ or due to increased wave-wave energy transfer and energy dissipation. But it is clear that the shape of the spectrum has a strong influence on the evolution of a particular wave frequency (i.e., Fig.5.19). There is also a possibility that this influence is partly imposed through the wind-wave energy input function.
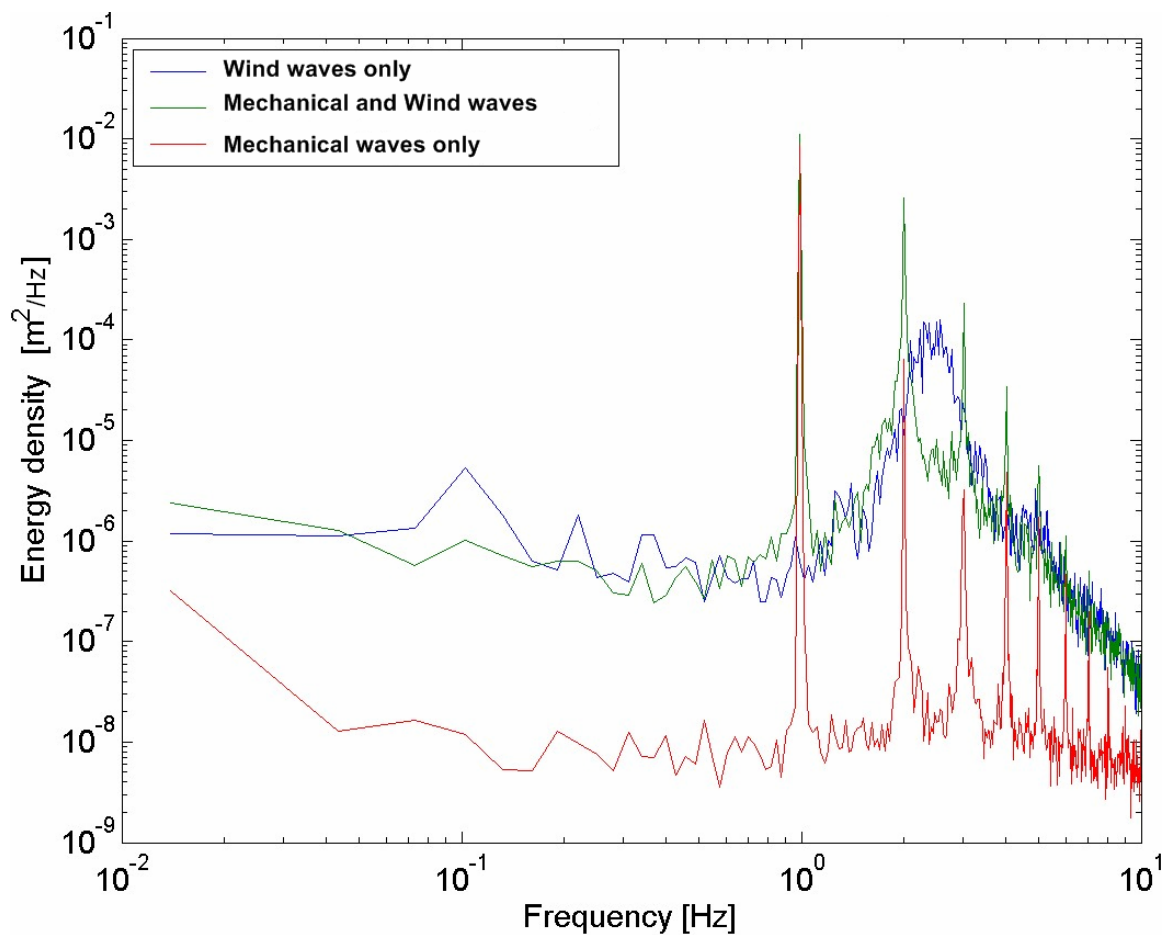
Figure.5.19. An example of three wave spectra: red and blue are only mechanical and only wind waves respectively (U_{10} = 19.1 ms^{-1}, ak = 0.1), green represents combined wave field. Note the energy transfer from wind wave peak (blue line, 2.5 Hz) towards the first harmonics of the mechanical wave, increased both in height and width (green, 2 Hz).

Two elevation gauges were installed at the beginning and the end of the tank. This allows an estimation of the value of the spectral wave growth function by definition (eq.2.9). Such a methods, of course, have limitations: first, the rate of the wave growth is averaged in the along tank direction; second, in addition to wind-wave energy input such an estimate will also incorporate energy dissipation and wave-wave transfer. In essence, the result will demonstrate the net wave evolution in the tank, rather than wind-wave input at one point.
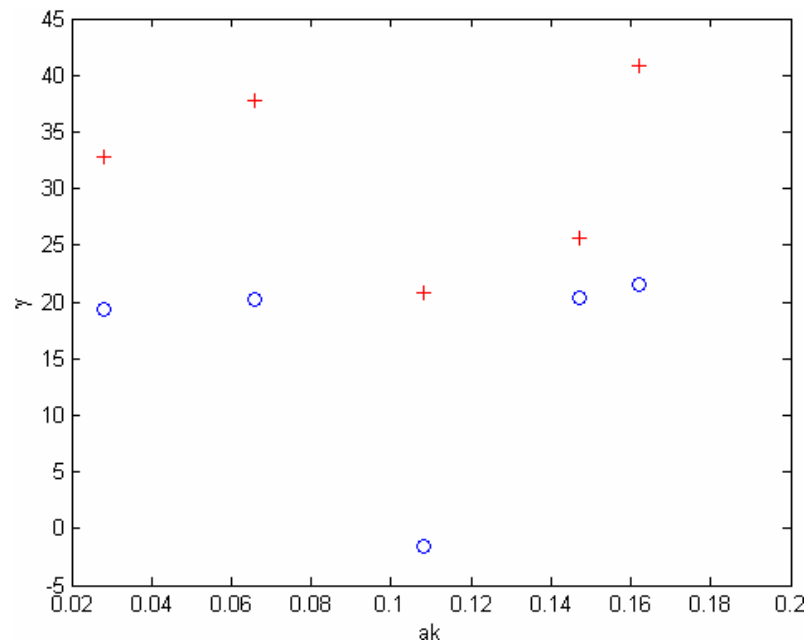
Figure 5.20. Spectral evolution estimate of wave-growth function (γ) for 5 experiments with the constant wind speed U_{10} = 19.1 ms^{-1}, constant mechanical wave with frequency f = 1Hz, but various steepnesses ak. Wind wave peak growth (2.5Hz) is shown in blue circles, growth of the first harmonics of the mechanical wave (2Hz) is shown in red pluses.

The set of experiments with constant wind and constant mechanical wave frequency, but various steepnesses (noted above), was investigated using such a spectral evolution approach. As shown in Fig.5.20, the resulting values of the wind-wave peak growth are shown in blue and the growth of the first harmonics (2Hz) is shown in red. Four out of five values for the non-dimensional wind-wave peak growth suggest its

independence on the mechanical wave steepness. However, the fifth point in the middle

has a dramatically lower value and, together with the decreased growth of the

corresponding harmonics, suggests that this phenomenon is sensitive to wave steepness

and that more data is needed to investigate this effect.

It is useful to compare the wave growth measurements obtained using different

methods. Given the wave-follower based wind-wave input measurements, the actual

wave spectra evolution is compared by measuring surface elevation at the beginning and

end of the tank. The latter wave growth estimate is expected to be lower due to intensive

wave breaking, while the direct wave-follower based method is not influenced by wave

dissipation. In Figure 5.21, the wave-follower based parameterization (blue line) is higher

than the spectral evolution estimate for the mechanical wave (red line).
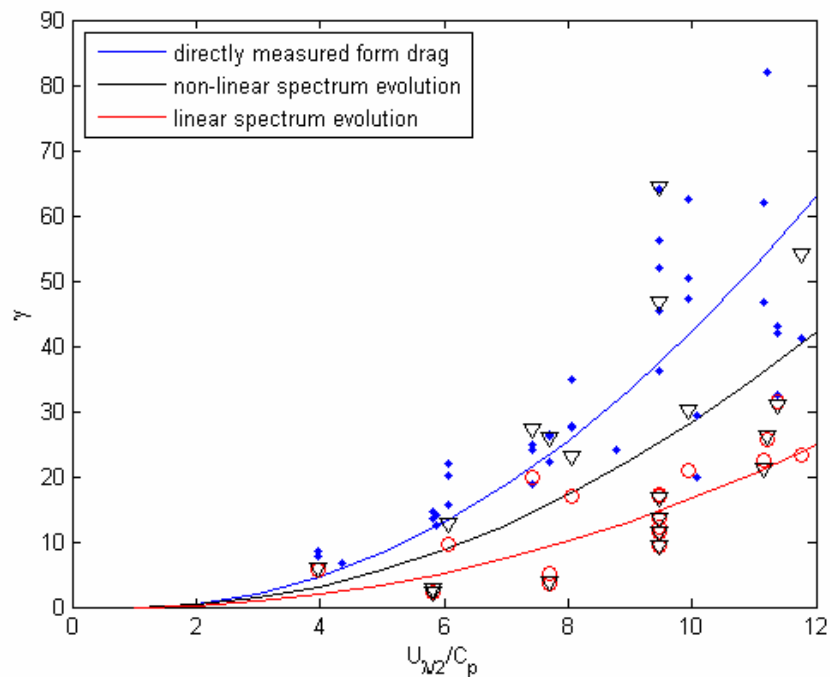
Figure 5.21. The estimates of the spectral wave growth function. Blue points and their quadratic fit are based on the wave-follower data, it is the same as in figure 5.16, red are based on spectral evolution and computed based on definition (eq.2.9), black are estimated based on a non-linear spectral evolution method (eq.5.8).

The pressure-slope correlation based method (blue line), however, is not expected to produce the same value as the definition based spectral evolution (i.e., direct wave spectra measurements applied to spectral wave growth function definition eq. 2.9). Specifically, these values can only be compared for linear waves, where the mean surface elevation, based on the phase resolved mean surface elevation technique produces a sine wave. Due to strong wind forcing, the mean shape of the studied wave is distorted and a fraction of the wave energy is contained in its harmonics. To fully account for the wave non-linearity in the spectral method of the wave growth estimate, the role of the major harmonics must be considered. The presence of harmonics propagating with the speed of the dominant wave was previously observed (e.g. Hara et al. 1997). Equation 5.8 is a modification of the original definition (eq.2.9) made specifically for the comparison with observed wind-wave momentum flux into a non-linear wave. The main frequency and its first and second harmonics were considered, as they contribute well above 99% of the energy in all cases:

$$\gamma(\omega) = \frac{\rho_w}{\rho_a} \frac{1}{\omega(E(\omega) + E(2\omega) + E(3\omega))} \frac{\partial(E(\omega) + E(2\omega) + E(3\omega))}{\partial t} \quad (5.8)$$

Another way considered for the comparison of two estimates was to separate the wave-follower based momentum flux measurements into harmonics and into the main frequency. This can be accomplished by enforcing a sine-wave shape of the main wave within the slope estimate procedure. In this case, the role of harmonics is unclear, because being attached to the main wave they can not be viewed as separate waves. Therefore, even if it is assumed that harmonics do not affect wind input into the main frequency (which is clearly an unlikely assumption), they still travel with a phase speed

faster than that of the free waves of their frequency. The wind forcing ratio U_{10}/C_p can not

be applied to them in a normal fashion.

Due to the reasons mentioned above, equation 5.8 was chosen as a better way to

compare spectral wave growth with the existing parameterization. The resulting points

and a least mean square fit to a quadratic function are shown in black color in Figure 5.21.

All three curves are given in the same quadratic form:

$$\gamma(\frac{U_{\lambda/2}}{C_p}) = A \cdot (\frac{U_{\lambda/2}}{C_p} - 1)^2, \qquad (5.9)$$

where A is equal to 0.52 (on average $G = 1$), 0.32, and 0.24 for blue, black and red

curves respectively. The resulting difference between the original blue curve and the

black curve is smaller, but is still expected and is explained mainly due to wave

dissipation and wave-wave energy transfer.

Chapter 6: Conclusions

In this work an experimental effort was undertaken to improve our understanding of near surface wind interaction with the wave field, and near-surface currents and turbulence. The most significant effort and achievement of this work is in the area of the airflow pressure fluctuations near the air-sea interface. Pressure measurements were used to obtain an empirical parameterization of wind wave growth in high winds.

The spectral wave growth function's (eq.2.9) dependence on various wind-wave parameters was investigated and its empirical form is given by:

$$\gamma(\frac{U_{\lambda/2}}{C_p}, ak) = 0.52G \cdot (\frac{U_{\lambda/2}}{C_p} - 1)^2,$$

where $G = (-1.9ak + 1.2)$.

This new parameterization extends the wind forcing range $U_{\lambda/2}/C_p$ up to 12 and reveals and describes the dependence on wave steepness ak in the range of 0.03 to 0.2. The dependence of the growth function on the wave steepness reflects the tendency for airflow separation as the curvature of the surface near the crest increases causing the streamlines to separate downstream of the crest. Separation produces changes in both the amplitude and the phase of the pressure pattern over the wave. The net effect on the pressure-slope correlation is negative at these high forcing conditions.

The remaining scatter, unaccounted for by the given parameterization was studied in detail and is partially explained by strong non-linear effects between the wave and its harmonics. The harmonics, traveling attached to the main wave, were found to exchange energy with wind waves and to grow in amplitudes. The resulting non-standard shape of

the wave significantly alters the value of the wind-wave momentum flux and dampens the growth of shorter wind waves. Such behavior is sensitive to specific wind-wave conditions, and in general, in strongly forced non-linear conditions, can not be accounted for within a linear spectral description of a wave field.

The contribution to wind stress, attributed to a single wave frequency was measured as a fraction of total wind stress. The fraction was found to be a function of the wave steepness, nearly independent of wind speed. Change of the wave steepness, however, had little effect on the value of the total wind stress, as increased steepness of a given wave symmetrically dampened the remaining wind wave field together with the wind stress caused by it.

Taken together with measurements of vertical profiles of currents and turbulent properties within the water column, the results of this work provide some of the necessary empirical parameterization in high winds, required to close the basic equations, described in chapter 2.a. This leads to the possibility of more accurate modeling and forecasting of ocean conditions within storms and hurricanes.

References

Andreas, E.L., 1998: A new sea spray generation function for wind speeds up to 32 m s^{-1}. *Journal of Physical Oceanography*, **28**, 2175–2184.

Babanin, A.V., Banner, M.L., Young I.R, Donelan M.A., 2007: Wave-follower field measurements of the wind-input spectral function. Part III: Parameterization of the wind-input enhancement due to wave breaking. *Journal of Physical Oceanography*, **37**, 2764–2775.

Babanin, A.V., Makin, V.K., 2008: Effects of wind trend and gustiness on the sea drag: Lake George study. *Journal of Geophysical Research*, **113**, C02015.

Babanin, A.V., Haus, B.K., 2009: On the existence of water turbulence induced by non-breaking surface waves. *Journal of Physical Oceanography*: In Press

Banner, M.L., Phillips, O.M., 1974: On the incipient breaking of small scales waves. *Journal of Fluid Mechanics*, **65**, 647-656.

Banner, M.L., Young, I.R., 1994: Modeling spectral dissipation in the evolution of wind waves. Part I: Assessment of existing model performance. *Journal of Physical Oceanography,* **24**, 1550-1571.

Banner, M. L., Peirson, W. L., 1998: Tangential stress beneath wind-driven air-water interfaces. *Journal of Fluid Mechanics*, **364**, 115-145.

Banner, M.L., Gemmrich, J.R., Farmer, D.M., 2002: Multiscale measurements of ocean wave breaking probability, *Journal of Physical Oceanography*, **32**, 3364-3375.

Belcher, S.E., Hunt, J.C.R., 1993: Turbulent shear flow over slowly moving waves. *Journal of Fluid Mechanics*, **251**, 109-148.

Belcher, S.E., Hunt, J.C.R., 1998: Turbulent flow over hills and waves, *Annual Review of Fluid Mechanics,* **30**, 507–38.

Bendat, J.S., Piersol, A.G., 1986: *Random Data: Analysis and Measurement Procedures*, New York: Wiley & Sons. 2nd edition.

Benjamin, T.B, 1959: Shearing flow over a wavy boundary, *Journal of Fluid Mechanics*, **6**, 161-205.

Benjamin, T.B., Feir, J.E., 1967: The disintegration of wavetrains on deep water. Part 1: Theory. *Journal of Fluid Mechanics*, **27**, 417–430.

Buckles, J., Hanratty, T.J., Adrian, R.J., 1984: Turbulent flow over large-amplitude wavy surfaces. *Journal of Fluid Mechanics*, **140**, 27-44.

Celenligil, M.C., Mellor, G.L., 1985: Numerical solution of two-dimensional turbulent separated flows using a Reynolds stress closure model. *ASME, Transactions, Journal of Fluids Engineering*, **107**, 467-476.

Chalikov, D., Sheinin, D., 1998: Direct modeling of one-dimensional nonlinear potential waves. In *Nonlinear Ocean Waves*. Ed. Perrie, W., *Advances in Fluid Mechanics* **17**, 207–258.

Charnock, H., 1955: Wind stress on a water surface. *Quarterly Journal of the Royal Meteorological Society,* **81**, 639-640.

Cheung, T.K., Street, R.L., 1988a: The turbulent layer in the water at an air—water interface. *Journal of Fluid Mechanics*, **194**, 133-151.

Cheung, T.K., Street, R.L., 1988b: Wave-following measurements in the water beneath an air-water interface. *Journal of Geophysical Research*, **93**, C11, 14089-14097.

Davis R.E., 1969: On the high Reynolds number flow over a wavy boundary. *Journal of Fluid Mechanics*, **36**, 337-346.

Deakon, E.L., Webb, E.K., 1962: Small-scale Interactions. In *The Sea*, **1**, Hill M.H., ed. Interscience, New York, 43-66.

Dickey, T.D., Mellor, G.L., 1979: The Kolmogoroff $r^{2/3}$ law. *Physics of Fluids,* **22**, 1029-1032.

Dobson, F.W., 1971: Measurements of atmospheric pressure on wind-generated sea waves. *Journal of Fluid Mechanics*, **48**, 91-127.

Dobson, F., Perrie, W., Toulany, B., 1989: On the deep-water fetch laws for wind-generated surface gravity waves. *Atmosphere-Ocean*, **27**, 210-236.

Donelan, M.A., 1990: Air-sea interactions. In *The Sea: Ocean Engineering Science,* **9**, copyright by John Wiley & Sons, Inc., 239-292.

Donelan, M.A., Anctil, F., Doering, J.C., 1992a: A simple method for calculating the velocity field beneath irregular waves. *Coastal Engineering,* **16**, 399-424.

Donelan, M.A, Skafel, M., Graber, H., Liu, P., Schwab, D., Venkatesh, S., 1992b: On the growth rate of wind-generated waves. *Atmosphere-Ocean,* **30**, 457–78

Donelan, M.A., Madsen, N.., Kahma, K.K., Tsanis, I.K., Drennan, W.M., 1999a: Apparatus for atmospheric surface layer measurements over waves. *Journal of Atmospheric and Oceanic Technology*, **16**, 9, 1172.

Donelan, M.A., 1999b: Wind-Induced Growth and Attenuation of Laboratory Waves, published in *Wind-over-Wave Couplings, Perspectives and Prospects*, editors: Sajjadi, S.G., Thomas, N.H., Hunt, J.C.R., Clarendon Press, Oxford, 183-194.

Donelan, M.A, Haus, B.K, Reul, N., Plant, W.J., Stiassnie, M., Graber, H.C., Brown, O.B., Saltzman, E.S., 2004: On the limiting aerodynamic roughness of the ocean in very strong winds. *Geophysical Research Letters*, **31**, L18306.

Donelan, M.A., Babanin, A.V., Young, I.R., Banner, M.L., McCormick, C., 2005a: Wave follower field measurements of the wind input spectral function. Part I. Measurements and calibrations. *Journal of Atmospheric and Oceanic Technology,* **22**(7), 799–813.

Donelan, M.A., Dobson, F., Graber, H., Madsen, N., McCormick, C., 2005b: Measurements of wind waves and wave-coherent air pressures on the open sea from a moving SWATH vessel. *Journal of Atmospheric and Oceanic Technology*, **22**, 896–908.

Donelan, M.A., Babanin, A.V., Young, I.R., Banner, M.L., 2006: Wave-follower field measurements of the wind-input spectral function. Part II: Parameterization of the wind input. *Journal of Physical Oceanography*, **36**, 8, 1672-1689.

Doron, P., Bertuccioli, L., Katz, J., Osborn, T.R., 2001: Turbulence characteristics and dissipation estimates in the coastal ocean bottom boundary layer from PIV data. *Journal of Physical Oceanography*, **31**, 8, 2108–2134.

Drennan, W.M., Kahma, K.K., Donelan, M.A., 1999: On momentum flux and velocity spectra over waves. *Boundary-Layer Meteorology,* **92**, 489-515.

Elliott, J.A., 1972a: Microscale pressure fluctuations near waves being generated by the wind. *Journal of Fluid Mechanics*, **54**, 427-448.

Elliott, J.A., 1972b: Instrumentation for measuring static pressure fluctuations within the atmospheric boundary layer. *Boundary-Layer Meteorology,* **2**, 476–495.

Ewing, J., Laing, A., 1987: Directional spectra of seas near full development. *Journal of Physical Oceanography*, **17**, 1696–1706.

Fincham, M., Maxworthy, T., Spedding, G.R., 1996: Energy dissipation and vortex structure in freely decaying, stratified grid turbulence. *Dynamics of Atmospheres and Oceans*, **23**, 1-4, 155-169.

Garratt, J.R., 1977: Review of drag coefficients over oceans and contitents. *Monthly Weather Review,* **105**, 915-929

Gastel, K., 1987: Nonlinear interactions of gravity-capillary waves: Lagrangian theory and effects on the spectrum. *Journal of Fluid Mechanics,* **182**, 499-523.

Hara, T., Bock, E.J., Donelan, M.A., 1997: Frequency-wavenumber spectrum of wind-generated gravity-capillary waves. *Journal of Geophysical Research*, **102,** C1, 1061–1072.

Hara, T., Belcher, S.E., 2002: Wind forcing in the equilibrium range of wind-wave spectra. *Journal of Fluid Mechanics,* **470** , 223-245.

Harris, D.B., DeCicco, D.J., 1993: Wave follower instrumentation platform redesign and test, *OCEANS '93. 'Engineering in Harmony with Ocean'. Proceedings*, **1**, I439-I443.

Hasselmann, K., 1960: Grundleichungen der Seegangsvoraussage. *Schiffstechnik,* **7**, 191-195.

Hasselmann, K., Coauthors, 1973: Measurements of wind-wave growth and swell decay during the Joint North Sea Wave Project (JONSWAP). *Deutsche Hydrographische Zeitschrift,* **A8**, 12, 95.

Hasselmann, K., Sell, W., Ross, D., Müller, P., 1976: A parametric wave prediction model. *Journal of Physical Oceanography*, **6**, 200–228.

Hasselmann, S., Haselmann, K., Bauer, E., Janssen, P.A.E.M., Komen, G. J., Bertotti, L., Lionello, P.,Guillaume, A., Cardone, V.C., Greenwood, J.A., Reistad, M., Zambresky, L., Ewing, J.A. (The WAMDI Group), 1988: The WAM Model – A third-generation ocean wave prediction model. *Journal of Physical Oceanography,* **18**, 1775–1810.

Hasselmann, D., Bösenberg, J., 1991: Field measurements of wave-induced pressure over wind-sea and swell. *Journal of Fluid Mechanics*, **230**, 391-428.

Howe, B.M., Chambers, A.J., Klotz, S.P., Cheung, T.K., Street, R.L., 1982: Comparison of profiles and fluxes of heat and momentum above and below an air-water interface. *Transaction of the ASME (J. Heat Transfer)*, **104**, 34–39.

Hristov, T.S., Miller, S.D., Friehe, C.A., 2003: Dynamical coupling of wind and ocean waves through wave-induced air-flow. *Nature*, **422**, 55-58.

Hsiao, S.V., Shemdin, O.H., 1983: Measurements of wind velocity and pressure with a wave follower during MARSEN. *Journal of Geophysical Research,* **88**, 9841-9849.

Hsu, C.-T., Wu, H.-Y., Hsu, E.-Y., Street, R.L., 1982: Momentum and energy transfer in wind generation of waves. *Journal of Physical Oceanography*, **12**, 929–951.

Jacobs, C.M.J., Oost, W.A., van Oort, C., Worrell, E.H.W., 2002: Observations of wave-turbulence interaction at sea using a wave follower. *EGS XXVII General Assembly*, Nice, 2178.

Janssen, P.A.E.M., 1991: Quasi-linear theory of wind-wave generation applied to wave forecasting. *Journal of Physical Oceanography*, **21**, 1631-1642.

Jeffreys, H., 1924: On the formation of waves by wind. *Proceedings of Royal Society*, **107A**, 189-206.

Jeffreys, H., 1925: On the formation of waves by wind. II. *Proceedings of Royal Society*, **110A**, 341-347.

Kitaigorodskii, S., Lumley, J., 1983a: Wave-turbulence interactions in the upper ocean. Part I: The energy balance of the interacting fields of surface wind waves and wind-induced three-dimensional turbulence. *Journal of Physical Oceanography*, **13**, 1977–1987.

Kitaigorodskii, S., Donelan, M.A., Lumley, J., Terray, E., 1983b: Wave-turbulence interactions in the upper ocean. Part II. Statistical characteristics of wave and turbulent components of the random velocity field in the marine surface layer. *Journal of Physical Oceanography*, **13**, 1988–1999.

Komen, G., Hasselmann, K., Hasselmann, K., 1984: On the existence of a fully developed wind-sea spectrum. *Journal of Physical Oceanography*, **14**, 1271–1285.

Kondo J., Fujinawa, Y., Naito, G., 1972: Wave-induced wind fluctuation over the sea. *Journal of Fluid Mechanics*, **51**, 751-771.

Kukulka, T., Hara, T., Belcher, S. E., 2007: A model of the air-sea momentum flux and breaking wave distribution for young, strongly forced wind-waves. *Journal of Physical Oceanography*, **36**(7), 1811-1828.

Kundu, P.,K., Cohen, I.M., 2002: Fluid mechanics. *Academic Press,* 638.

Lamb, H., 1945: Hydrodynamics. 6th, first American edition. *New York: Dover Publications.*

Large, W.G., Pond, S., 1981: Open ocean momentum flux measurements in moderate to strong winds. *Journal of Physical Oceanography,* **11**, 324-336.

Lumley, J.L., Panofsky, H.A., 1964: The structure of atmospheric turbulence. *New York: Interscience.*

Makin, V.K., Branger, H., Peirson, W.L., Giovanangeli, J.P., 2007: Stress above wind plus paddle waves: modelling of a laboratory experiment. *Journal of Physical Oceanography*, **37**, 2824–2837.

Mellor, G.L., 1966: The effects of pressure gradients on turbulent flow near a smooth wall. *Journal of Fluid Mechanics,* **24** , 255-274.

Mellor, G.L., 2008a: The depth-dependent current and wave interaction equations: a revision. *Journal of Physical Oceanography*, **38**, 2587-2596.

Mellor, G.L., Yamada, T., 1982: Development of a turbulence closure model for geophysical fluid problems. *Reviews of Geophysics and Space Physics*, **20**, 4, 851-875.

Mellor, G. L., Donelan, M. A., Oey, L.-Y., 2008b: A surface wave model for coupling with numerical ocean circulation models. *Journal of Atmospheric and Oceanic Technology*, **25**, 1785-1807.

Melville, W.K., 1982: The instability and breaking of deep-water wave. *Journal of Fluid Mechanics*, **115**, 165-185.

Melville, W.K., Rapp, R.J., 1985: Momentum flux in breaking waves, *Nature,* **317**, 514-516.

Miles, J.W., 1957: On the generation of surface waves by shear flows. *Journal of Fluid Mechanics*, **3**, 185-204.

Miles, J.W., 1959: On the generation of surface waves by shear flows, Part 2. *Journal of Fluid Mechanics,* **6**, 568-582.

Miles, J.W., 1960: On the generation of surface waves by turbulent shear flows. *Journal of Fluid Mechanics*, **7**, 469-478.

Miles, J.W., 1993: Surface-wave generation revisited. *Journal of Fluid Mechanics,* **256**, 427-441.

Moskowitz, L., 1964: Estimates of the power spectrums for fully developed seas for wind speeds of 20 to 40 knots. *Journal of Geophysical Research*, **69**(24), 5161–5179.

Nishiyama, R.T., Bedard, A.J., Jr., 1991: A "Quad-Disc" static pressure probe for measurement in adverse atmospheres: With a comparative review of static pressure probe designs. *Review of Scientific Instruments,* **62**, 2193.

Ocampo-Torres, F.J., Donelan, M.A., Merzi, N., Jia, F., 1994: Laboratory measurements of mass transfer of carbon dioxide and water vapour for smooth and rough flow conditions. *Tellus*, B, **46**, 16– 32.

Okuda, K., Kawai, S., Toba, Y., 1977: Measurement of skin friction distribution along the surface of wind waves. *Journal of Oceanography,* **30**,190-198.

Peirson, W.L., Garcia A.W., 2008: On the wind-induced growth of slow water waves of finite steepness. *Journal of Fluid Mechanics*, **608**, 243-274

Pope, S.B., 2000: Turbulent flows. *Cambridge University Press.*

Powell, M.D., Vickery, P.J., Reinhold, T.A., 2003: Reduced drag coefficient for high wind speeds in tropical cyclones. *Nature,* **422**, 279-283.

Prandtl, L., 1905: Uber Flussigkeitsbewegung bei sehr kleiner Reibung. Verhandlungen des III. Internationalen Mathematiker Kongresses. *Heidelberg,* 484–491.

Rapp, R.J., Melville, W.K., 1990: Laboratory measurements of deep-water breaking waves. *Philosophical Transactions of the Royal Society of London. Series A, Mathematical and Physical Sciences*, **331**, 1622, 735-800.

Reul, N., Branger, H., Giovanangeli, J.-P., 2008: Air flow structure over short-gravity breaking water waves. *Boundary-Layer Meteorology*, **126**, 477–505.

Shen, L., Zhang, X., Yue, D.K.P., Triantafyllou, M.S., 2003: Turbulent flow over a flexible wall undergoing a streamwise travelling wave motion. *Journal of Fluid Mechanics,* **484** , 197-221.

Shchepetkin, A.F., McWilliams, J.C., 2005: The regional oceanic modeling system (ROMS): A split-explicit, free-surface, topography-following-coordinate oceanic model. *Ocean Modelling*, **9 (4)**, 347-404.

Shemdin, O.H., Hsu, E.Y., 1967: Direct measurement of aerodynamic pressure above a simple progressive gravity wave. *Journal of Fluid Mechanics*, **30**, 403-416.

Smith, S.D., 1980: Wind stress and heat flux over the ocean in gale force winds. *Journal of Physical Oceanography,* **10**, 709-726.

Snyder, R.L., Cox, C.S., 1966: A field study of the wind generation of ocean waves. *Journal of Marine Research,* **24**, 141–178.

Snyder, R.L., 1974: A field study of wave-induced pressure fluctuations above surface gravity waves. *Journal of Marine Research,* **32**, 497-531.

Snyder, R.L., Dobson, F.W., Elliott, J.A., Long, R.B., 1981: Array measurements of atmospheric pressure fluctuations above surface gravity waves. *Journal of Fluid Mechanics*, **102**, 1.

Sullivan, P.P., McWilliams, J. C. Moeng, C.-H., 2000: Simulation of turbulent flow over idealized water waves. *Journal of Fluid Mechanics*, **404**, 47-85.

Terray, E.A., Drennan, W.M., Donelan, M.A., 1999: The vertical structure of shear and dissipation in the ocean surface layer. In: *The wind-driven air-sea interface: electromagnetic and acoustic sensing, wave dynamics and turbulent fluxes*. Ed: Banner, M.L., Pub: School of Mathematics, U. New South Wales, Sydney 2052, Australia, 239-245.

Uz, B.M., Donelan, M.A., Hara, T., Bock, E.J., 2002: Laboratory studies of wind stress over surface waves. *Boundary-Layer Meteorology*, **102**, 2, 301-331(31).

Valenzuela, G.R., Laing, M.B., 1972: Nonlinear energy transfer in gravity–capillary wave spectra, with applications. *Journal of Fluid Mechanics,* **54**, 507-520.

Wright, C.W., Walsh, E.J., Vandemark, D., Krabill, W.B., Garcia, A.W., Houston, S.H., Powell, M.D., Black, P.G., Marks, F.D., 2001: Hurricane directional wave spectrum spatial variation in the open ocean. *Journal of Physical Oceanography,* **31**, 2472-2488.

Wyngaard, J.C., Siegel, A.,Wilczak, J., 1994: On the response of a turbulent-pressure probe and the measurement of pressure transport. *Boundary-Layer Meteorology,* **69**, 379–396.

Yefimov, V.V., Khristoforov, G.N., 1971: Spectra and statistical relations between the velocity fluctuations in the upper layer of the sea and surface waves. *Izvestiya Academy of Science USSR, Atmospheric and Oceanic Physics, English Translation*, **7**, 1290– 1310.

Young, I.R., Babanin, A.V., 2006: Spectral distribution of energy dissipation of wind-generated waves due to dominant wave breaking. *Journal of Physical Oceanography,* **36**, 376-394.

Zakharov, V.E., 1968: Stability of periodic waves of finite amplitude on the surface of a deep fluid. *Journal of Applied Mechanics and Technical Physics*, **9**, 190–194.

Zhang, X., 1995: Capillary–gravity and capillary waves generated in a wind wave tank: observations and theories. *Journal of Fluid Mechanics,* **289**, 51-82.